

**Modeling Perspective on Translatability of
Deep Brain Stimulation Mechanism for
Treating Parkinsonian Motor Symptoms in
Rodent and Human**

Dissertation

zur

Erlangung des akademischen Grades

Doktor-Ingenieur (Dr.-Ing.)

der Fakultät für Informatik und Elektrotechnik

der Universität Rostock

vorgelegt von

Konstantin Butenko geb. am 25.02.1994 in Biysk, Russland
aus Rostock

Rostock, 29.11.2021

Tag der Verteidigung: 10.03.2022

Gutachter:

Prof. Dr. Ursula van Rienen, Universität Rostock

Prof. Dr. med. Rüdiger Köhling, Universitätsmedizin Rostock

Prof. Dr. Madeleine Lowery, University College Dublin

If the human brain were so simple that we could understand it, we would be so simple that we couldn't.

Emerson M. Pugh

If you find a path with no obstacles, it probably does not lead anywhere.

Frank A. Clark

Acknowledgement

First and foremost, I would like to express my sincere gratitude to Prof. Dr. van Rienen for her profound support and supervision throughout my doctoral studies and to Prof. Dr. Horn for his expert guidance in the medical aspects of my research. Furthermore, I would like to thank my colleagues Andrea Andree and Ningfei Li, who were always eager to help me. I am deeply thankful to my mother Marina Butenko, who was supportive at each step of my life journey.

Abstract

Over the past years, deep brain stimulation (DBS) has become an established treatment for Parkinson’s disease. Although standards of care were formulated, they require extensive and often unpleasant stimulation tuning, which still does not guarantee the possible highest symptom alleviation and absence of side-effects. To tackle this issue and establish new efficient stimulation protocols, researchers need to gain a better understanding of the DBS action mechanism. The research inevitably involves invasive procedures and is thus supported by animal studies, including primate models due to the similar brain anatomy as well as rodent models due to relatively low costs and simple animal management. At the same time, hypotheses on the mechanism can be pre-tested with *in silico*, primarily computational studies. Furthermore, these studies are able to assess whether differences in anatomy and DBS technology for humans and animals lead to significant distinctions of the induced neuromodulation or the pattern is reproducible.

This thesis starts with a description of computational methods implemented to simulate DBS effects on neural tissue, with a particular emphasis on accurate and efficient electric field modeling. Different aspects of modeling are then discussed in the context of clinical relevance. Additionally, challenges pertinent to rodent DBS studies are highlighted. Afterward, the presented methods are applied to investigate possible DBS mechanisms in Parkinson’s disease for human and rodent treatment. Three distinct though not contradictory paradigms on neuromodulation are analyzed: local stimulation of nuclei, pathway activation in white matter fibers, and tuning of the basal ganglia circuit. For the local effects, such aspects as the electrode selection and its implantation precision are discussed, as well as the extent of the DBS-induced neural activation in nuclei. The impact of pathway activation is examined in the context of correlation with clinical outcome, as well as theoretical disruption of the pathological activity in a human basal ganglia-thalamo-cortical network. At last, the reproducibility of the pathway activation patterns, considered beneficial in these analyses, is estimated for the rat model, taking into account uncertainties in brain tissue conductivity.

The presented results support the hypothesis that the primary mechanism of neuromodulation in DBS is axonal rather than somatic recruitment. The outcome of *in silico* optimization for pathway activation in a realistic volume conductor model indicates that stimulation of the rat subthalamic nucleus can simultaneously recruit beneficial and avoid detrimental tracts. However, the reproducibility of the theoretically optimal activation profiles is limited. The thesis also provides insight into biophysical and computational problems that should be addressed in order to optimize animal studies and avoid possible misconceptions when transferring experimental findings to clinical trials.

Zusammenfassung

In den letzten Jahrzehnten hat sich die Tiefe Hirnstimulation (THS) in der Behandlung des Morbus Parkinson bewährt. Die Einstellung der Stimulationsparameter erfolgt nach einem Standardverfahren, welches umfangreich ist und unangenehme Stimulationsoptionen enthält, welche dennoch nicht immer die bestmögliche Symptomlinderung und Vorbeugung von Nebenwirkungen garantiert. Um dieses Problem zu beseitigen, sowie um neue, effiziente Stimulationsprotokolle zu etablieren benötigen Wissenschaftler ein besseres Verständnis des THS-Wirkmechanismus. Für die Forschung sind invasive Prozeduren unvermeidlich, weshalb zu meist Tierstudien durchgeführt werden. Aufgrund der vergleichbaren Gehirnanatomie beinhalten diese häufig Primaten, außerdem werden wegen der einfachen Tierhaltung und der geringen Kosten auch Nagetiermodelle genutzt. Zusätzlich können Hypothesen mit *in silico* Studien getestet werden. Diese können einschätzen, ob Unterschiede in der Anatomie und der THS-Technologie zwischen Menschen und Tieren zu signifikanten Unterschieden in der induzierten Neuromodulation führen, oder ob die Muster reproduzierbar sind.

Diese Arbeit beginnt mit einer Beschreibung der Berechnungsmethoden die zur Simulation von THS-Effekten auf Nervengewebe implementiert sind, mit Fokus auf die akkurate und effiziente Modellierung elektrischer Felder. Anschließend werden verschiedene Aspekte des Modellierens im Kontext ihrer klinischen Relevanz diskutiert. Weiterhin werden die Herausforderungen bezüglich THS Studien in Nagetieren hervorgehoben. Im darauffolgenden Teil werden die vorgestellten Methoden zur Untersuchung möglicher THS-Mechanismen in Morbus Parkinson sowohl für die Behandlung von Menschen als auch für Nagetiere angewendet. Drei unterschiedliche, jedoch nicht widersprüchliche Paradigmen der Neuromodulation werden analysiert: lokale Stimulation der Nuclei, Nervenbahnaktivierung in der weißen Substanz und Regelung des Kreislaufs der Basalganglien. Für lokale Effekte werden Aspekte wie die Elektrodenauswahl und die Implantationspräzision, sowie das Ausmaß der THS-induzierten neuronalen Aktivität in Nuclei diskutiert. Der Einfluss von Nervenbahnaktivierungen wird in Korrelation mit klinischen Daten, sowie als theoretisch angenommene Unterbrechung der pathologischen Aktivität im menschlichen Gehirnnetzwerk von Basalganglien, Thalamus und Kortex betrachtet. Abschließend wird die Reproduzierbarkeit der Nervenbahnaktivierung, welche in dieser Analyse als vorteilhaft erachtet wird, für Rattenmodelle evaluiert, wobei Unsicherheiten in der Leitfähigkeit des Gehirngewebes berücksichtigt werden.

Die präsentierten Ergebnisse unterstützen die Hypothese, dass der direkte Mechanismus der Neuromodulation in THS am ehesten aus axonaler als aus somatischer Aktivierung besteht. Ergebnisse der *in silico* Optimierung für die Nervenbahnaktivierung in einem realistischen Volumenleitermodell weist darauf hin, dass eine Stimulation des Subthalamischen

Nucleus eine simultane Aktivierung vorteilhafter Nervenbahnen auslösen kann und nachteilige Pfade vermeidet. Darüber hinaus liefert die Arbeit Einblicke in biophysikalische und numerische Probleme, welche adressiert werden sollten, um Tierstudien zu optimieren und um mögliche Missverständnisse beim Transfer von experimentellen Ergebnissen in klinische Studien zu vermeiden.

Contents

1	Introduction	1
1.1	Parkinson’s disease pathophysiology and treatment approaches .	1
1.2	General notion of DBS mechanism in Parkinson’s disease	4
1.2.1	Non-human primate PD model	7
1.2.2	Rodent PD model	8
2	Computational Methods for Deep Brain Stimulation: From Medical Imaging to Neural Activation	11
2.1	DBS-induced electric field in brain tissue	11
2.1.1	Mathematical Formulation	12
2.1.2	Brain tissue properties	15
2.1.3	Electrode–tissue interface	23
2.2	DBS-induced neural activity	26
2.2.1	Biophysics of action potential	26
2.2.2	Computational modeling of neurons	28
2.2.3	Quantification concepts of induced activation	30
2.3	Finite Element Method	35
2.3.1	FEniCS	35
2.3.2	FEM formulation	35
2.3.3	Solvers	39
2.3.4	Electric potential derivatives	39
2.3.5	Mesh refinement	40
2.4	Simulation platform OSS-DBS	42
2.5	Uncertainty quantification in DBS	44
3	Local Modulation of Neural Activity	46
3.1	Direct DBS effect in stimulated nuclei	46
3.2	Precision of implantation and VTA	50
3.3	Field focalization for cranial implantations	52
4	Pathway Activation Induced by Stimulation of Subthalamic Nucleus	54
4.1	Basal ganglia pathways	54
4.2	Direct correlation of pathway activation with motor improvement	58

Contents

4.3	Network effects of the pathway activation	65
4.4	Pathway activation modeling for rat STN-DBS	71
4.4.1	Reconstruction of pathways using diffusion imaging	71
4.4.2	Optimization of pathway activation	77
4.4.3	Effect of uncertainty in tissue conductivity	86
4.5	Limitations of the pathway activation modeling	91
5	Conclusion	92
5.1	Outlook	95
A	Appendix	I
A.1	Mesh refinement	I
A.2	Modeling of human STN-DBS	III
	List of Acronyms	IV
	List of Symbols	VII
	List of Figures	XI
	List of Tables	XXIV
	Bibliography	XXVI

Chapter 1

Introduction

1.1 Parkinson's disease pathophysiology and treatment approaches

Parkinson's disease (PD) is a neurological disorder with a wide range of both motor and non-motor symptoms. The former include akinesia (inability to initiate a movement), bradykinesia (slowness of movement), rigidity, resting tremor, postural instability and dysarthria (failure of muscles involved in speech production). Possible non-motor symptoms include depression, psychosis, apathy, sleep disturbance, etc. PD manifests in a progressive neurodegeneration and predominantly affects the elderly population with about 1% occurrence over the age of 60 years and 5% over the age of 85 years. The prevalence of PD is only surpassed by Alzheimer's disease, and the impact of the disorder becomes increasingly apparent in the ever aging Western society.

While different pathophysiological models of PD were proposed [1], none of them can completely integrate experimental and clinical observations. In this section I will only provide a general description, while a more detailed discussion follows in Chapter 4. In the basal ganglia (Fig. 1.1), the pathology arises from the death of dopaminergic cells in the substantia nigra pars compacta (SNc). The cause of death is not yet determined, thus complicating a development of preventive therapies. The reduced dopamine supply of the striatum causes an imbalance of its activity leading to a disinhibition of the substantia nigra pars reticulata (SNr) and the internal segment of the globus pallidus (GPi) (see Fig. 1.2) via the direct pathway (cortex–striatum–GPi/SNr), while the external segment (GPe) is redundantly inhibited via the indirect pathway (cortex–striatum–GPe–GPi/SNr). In turn, the more active GPi and SNr suppress the activity in the ventral anterior thalamus, reducing its input to the motor cortical regions. At the same time, the suppressed GPe releases activity

in the subthalamic nucleus (STN), the excitatory efferents of which innervate both pallidal segments and the SNr. The reciprocity of the STN and the GPe is suspected to be a factor in the generation of abnormal synchronous oscillations that were consistently observed in the basal ganglia of PD patients and non-human primates [1, 2, 3, 4, 5]. Additionally, oscillatory activity in the STN might be induced via the hyperdirect pathway [6] that descends to the nucleus directly from the motor cortical regions. It was shown that bursting activity is the major contributor to these pathological oscillations [7], and, in particular, long-duration bursts are implicated in the onset of symptoms [8]. Furthermore, one study with a PD mouse model demonstrated that bursting of the GPi leads to a thalamic inhibition followed by a rebound that invokes PD-like motor symptoms, and a suppression of the GPi input to the thalamus results in alleviation [9]. However, this finding has not been reproduced in primates yet.

The initial treatment of severe PD cases was conducted by lesioning various thalamic and basal ganglia structures. Particular success was achieved by Lars Leksell with pallidotomy of the posteroventral portion [13]. The lesioning practice was, however, eclipsed by the discovery of levodopa, a drug that increases dopamine concentrations and leads to a significant alleviation of the motor symptoms. Nevertheless, it was observed that over the course of levodopa treatment, PD patients developed dyskinesia (involuntary movements), motor fluctuations and drug resistance. Thus, lesions again gained attention in clinics, but now supported by a better understanding of the pathophysiology, elucidated by animal studies and advanced medical imaging techniques that improved the accuracy of implantations. Apart from alleviation by pallidal

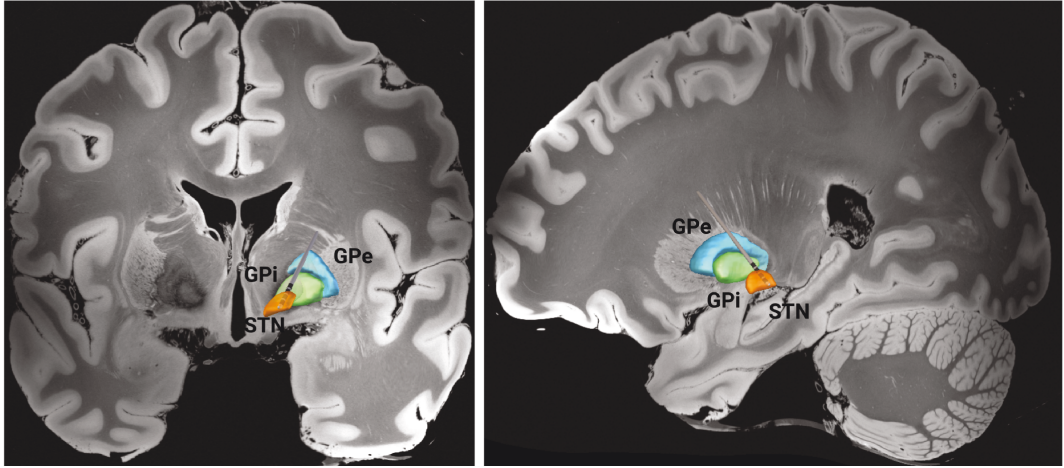


Figure 1.1: *Coronal and sagittal view of the selected structures of the basal ganglia visualized using a high resolution and subcortical atlases [10, 11] of the human brain in Lead-DBS [12] (STN – subthalamic nucleus, GPe and GPi – external and internal segments of the globus pallidus, respectively).*

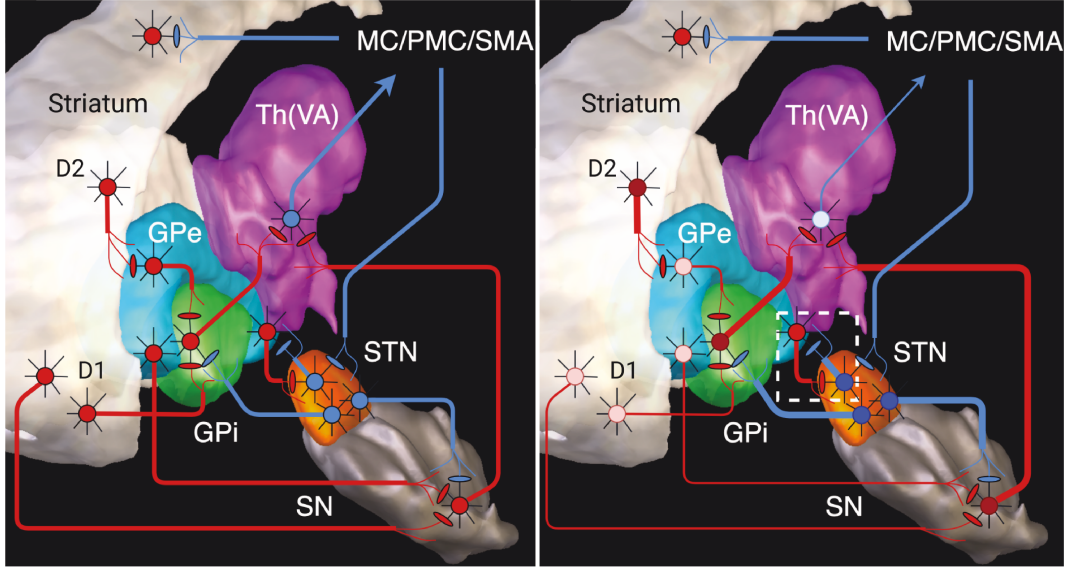


Figure 1.2: Circuit diagram of the human brain basal ganglia-thalamo-cortical activity in the healthy (left) and the parkinsonian (right) states. Red and blue colors correspond to inhibitory and excitatory projections, respectively, and the intensity reflects the activity level. Brain structures are visualized using a subcortical atlas [11] in Lead-DBS (GPe and GPi – external and internal segments of the globus pallidus, respectively, Th(VA) – ventral anterior nucleus of the thalamus, STN – subthalamic nucleus, SN – substantia nigra, MC/PMC – primary motor and premotor cortical regions, SMA – supplementary motor area, D1/D2 – dopamine receptors). The distinctive trait of the parkinsonian state is the imbalanced striatal output that leads to higher activity in the GPi, SN and STN. The reciprocal coupling of the latter with the GPe (white dash-line) is a probable source of the abnormal oscillatory activity [1].

ablations, lesioning of the STN was shown to be effective in akinesia, bradykinesia and rigidity reduction [14]. Still, the procedure remained controversial due to its irreversibility and inconsistent outcome.

The knowledge and skills acquired with lesioning were not in vain. Prior to the procedure, a surgeon would apply a small current to test the patient's response to determine the probe's position and the effect on the local brain region. The idea to employ this electric testing as a chronic therapy was proposed by Alim-Louis Benabid, and so deep brain stimulation (DBS) was invented. The stimulation is conducted via an electrode, usually with 4 or 8 contacts, which is implanted in the basal ganglia or the thalamus. The current is delivered by a battery-driven pulse generator implanted under the clavicle bone, and a titanium casing of the generator serves as the grounding electrode. In comparison with lesioning, DBS produces less side-effects, allows stimulation adjustment by means of contact and signal selection, and inflicts a significantly lower tissue damage, thus reducing irreversible effects. Numerous clinical studies on PD demonstrated that optimal DBS protocols, i.e an accu-

rate implantation and a clinically effective choice of the stimulating contacts, can alleviate most of the motor symptoms. At the same time, reports on cognitive improvement are inconsistent, with evidence of depressive or mania-like behavior and even suicidal tendencies [15, 16, 17, 18]. Furthermore, there is the problem of poor responders¹, i.e. patients whose improvement with DBS is insignificant when taking into account the surgery risks and other complications. In addition, our knowledge of the therapeutic mechanism of DBS in PD remains limited, and a deeper insight might promote the emergence of more effective and efficient DBS protocols. Apart from the aforementioned issues, the protocols are expected to reduce the manual optimization period of the stimulation, when multiple clinical visits and unpleasant current tuning are required. The efficiency of the treatment is also important for the battery life: its surgical replacement is one of the main concerns for PD patients.

The application of DBS is not only limited to PD. It has been demonstrated that the stimulation of the GPi is effective against symptoms of dystonia, while essential tremor is substantially suppressed by DBS of the ventral intermediate thalamus or the zona incerta. For obsessive-compulsive disorder, a general improvement is observed when stimulating the nucleus accumbens or the ventral capsule/ventral striatum. DBS of the centromedian-parafascicular-thalamic complex reduces motor tics of Tourette's syndrome, and in patients with Huntington's Disease pallidal stimulation was shown to suppress chorea. Lastly, preliminary studies demonstrate a certain success of DBS as an Alzheimer's Disease treatment.

1.2 General notion of DBS mechanism in Parkinson's disease

In clinics, a conventional DBS signal is a 30–90 μs rectangular pulse with a repetition rate of 90–185 Hz . To ensure a capacitive nature of the stimulating current², highly polarizable platinum/iridium electrodes are employed [19]. The current generates a relatively strong extracellular electric field that depolarizes membranes of neural tissue. If the depolarization is high, it might induce activation of voltage-gated ion channels that in turn will generate an action potential, also known as "spike". In this event, we will consider a neuron to be "activated". For more details on the action potential initiation, please refer to Chapter 2.

¹One of the criteria for DBS patient selection is a history of successful levodopa treatment (33% improvement) to exclude candidates with atypical PD that is not DBS responsive.

²Resistive current would arise from electrochemical reactions on the electrode surface, affecting its integrity and possibly leading to additional tissue damage.

Certainly, the mean endogenous activation, i.e. the activation triggered by cell-to-cell communication, is reduced when the nucleus is lesioned. This leads to a disruption of the abnormal synchronization in the basal ganglia and is thought to be the mechanism of symptom alleviation. The effectiveness of STN lesioning in the disrupting can be also explained by the high density of various neural pathways in the vicinity of the nucleus. These pathways provide a structural connectivity of different areas and are not limited to the basal ganglia. Therefore, lesioning might induce neurological changes beyond disruptions of the local circuitry. For STN-DBS, a lower activity measured in the nucleus was the initial evidence of a similar mechanism involved in the therapeutic effect. The inhibition would arise not from the mechanical damage, but due to the stimulation of GABAergic (inhibitory) afferents, projecting primarily from the GPe, and the decreased activity of the STN would lead to a reduction of the pathological bursting. However, the ability of STN-DBS to suppress the bursts was challenged [20]. It was also demonstrated that efferents of the STN to the GPi and GPe roughly follow the DBS signal, increasing activity in these nuclei [21, 22], and therefore the mechanism had to be reconsidered. Warren Grill proposed a concept of "informational lesion", where the disruption occurs not via the elimination of pathological oscillations in the STN, but by overwriting it with a regular non-physiological pattern that does not convey information content [23]. The overwriting occurs not only by filtering in the refractory period, which follows a spike and temporarily prevents further firing, but also due to synaptic depression and depletion of neurotransmitters. It was observed that STN-DBS modulates neural activity in the whole basal ganglia (see Fig. 1.3) and certain regions of the thalamus and the neocortex, driving it to a new functional state, which is distinct from the healthy condition. In the context of brain pathways, the stimulation of motor-related corticosubthalamic fibers has a significant correlation with the clinical outcome [24]. These fibers mainly innervate the dorso-lateral portion of the STN that was shown to be effective in alleviating of motor symptoms. Curiously, the corticosubthalamic afferents emerge from the corticofugal tract, which stimulation a contrario must be avoided as it induces motor contractions and dysarthria. For tremor-dominant PD, it was observed that the stimulation of the cerebellothalamic pathway correlates with the improvement [25].

An alternative target in PD treatment is the GPi. While its stimulation is not accompanied by a reduction of the levodopa intake, which is the case for STN-DBS, it shows a moderately higher effect on the cognitive symptoms. Therefore, GPi-DBS is usually recommended for patients suffering from mood disorders, such as depression and anxiety. The mood fluctuations, reported in some studies on STN-DBS, might originate from the stimulation of pathways projecting to the ventral tegmental area, implicated in the reward circuitry of the brain. In the basal ganglia, the DBS-induced modulations are similar for the STN and the GPi since afferents of the latter from the STN and the

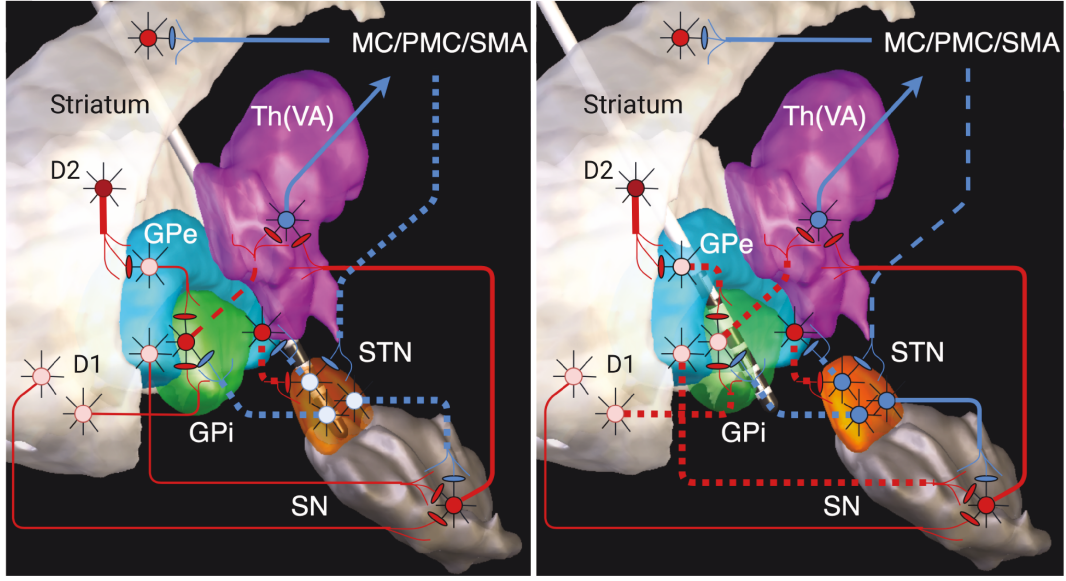


Figure 1.3: *Circuit diagram of the human brain basal ganglia-thalamo-cortical activity during DBS in the STN (left) and the GPi (right). Red and blue colors correspond to inhibitory and excitatory projections, respectively, and the intensity reflects the activity level. Dotted lines show projections that are likely to be directly stimulated by the DBS-induced electric field. The stimulation extent of the hyperdirect pathway by DBS-GPi and the pallidothalamic projection by STN-DBS (dash-lines) is limited due to the relative remoteness. Note that stimulations lead to a modulation of the basal ganglia output to the thalamus.*

GPe are recruited in both cases. On the other hand, a pallidal stimulation is expected to activate inhibitory afferents from the striatum and/or efferents to the ventral anterior thalamus, hence directly altering the basal ganglia output. Furthermore, GPi-DBS should have a lesser effect on the hyperdirect pathway. Nevertheless, a direct activation of the pallidothalamic pathways can also occur in STN-DBS, and, considering the strong similarity of the motor symptom alleviation, the mechanisms are expected to be closely related. In this thesis, the emphasis lies on DBS for motor symptom alleviation, which, in rodents, is easier to assess than cognitive improvement. For this reason, neuromodulatory effects will be described for stimulation of the STN, which is the most frequent target for the treatment.

In contrast to DBS in patients with dystonia, the treatment efficacy for PD can be observed without a delay, but the effect quickly wears off after the stimulation has ceased. Various approaches were considered to reduce the power consumption, e.g. cessation during sleep or adaptive stimulation that is active only when certain electrophysiological markers are registered. A relatively novel approach is coordinated reset stimulation, where alternating contact pairs are active (inject and eject the current) over time. This protocol is theorized to be more efficient in the desynchronization of the pathological

activity by shifting the network into a new state that is stabilized by downregulated synaptic connectivity. In pilot studies, coordinated reset stimulation was shown to provide lasting effects on the motor symptoms with reduced power consumption [26, 27].

Yet, conventional DBS was also shown to affect synaptic plasticity. In rodents, a stimulation induced short and long-term depression of STN neurons was reported [28], while in humans a long-term potentiation in the motor cortex was observed for patients treated with both DBS and levodopa. Nevertheless, the direct involvement of synaptic plasticity in the therapeutic effect is not yet established, though indirect evidence, such as the minute latency of bradykinesia relief, implies the relevance of this mechanism. Besides, DBS facilitates various neurochemical changes. For example, some studies in rats and non-human primates reported an increase in dopamine levels [29, 30], despite a low excitability of dopaminergic projections by extracellular fields. Furthermore, the electrical stimulation might also affect non-neural tissue, in particular, astrocytes that alter the release of neurotransmitters. Taking these factors into consideration, a profound neurological reorganization can be assumed. Functional magnetic resonance imaging (fMRI) shows that STN-DBS does not only decouple the nucleus from its afferents, but also increases activity in the thalamocortical and the direct pathways, while in rats a one-hour stimulation was shown to strengthen corticostriatal connectivity [31]. Furthermore, neuroprotective properties of DBS were observed in both rats and non-human primates, where stimulation led to reduced losses of nigral neurons.

Although desirable, the simultaneous modeling of all these mechanisms is still out of reach for the modern computational science³. In this thesis, we will mainly focus on the immediate effect of DBS on neural tissue, though the modulation of the network activity will be also discussed in Chapter 4.

1.2.1 Non-human primate PD model

Unquestionably, non-human primates have the closest brain anatomy and physiology to humans. Though this factor raises ethical concerns, such animal models inherently offer the best translatability to clinical applications, concerning both efficiency and safety. A major step in the development of primate PD models was the discovery of the toxin 1-methyl-4-phenyl-1,2,3,6-tetrahydropyridine (MPTP). Initially synthesized as a recreational drug, it produced PD-like symptoms in users and thus drew medical attention. Monkeys treated with MPTP "demonstrated most all of the cardinal motor signs of PD except for tremor, including bradykinesia/akinesia, rigidity, gait and

³Nevertheless, attempts are being made, for example, see the Human Brain Project <https://www.humanbrainproject.eu/en/>.

postural imbalance, freezing, and dyskinesia when given L-dopa" [13]. The experiments in non-human primates concluded that the treatment reproduces a pathological and biochemical state similar to parkinsonism [32, 33], thus allowing researchers to improve their understanding of PD with invasive electrophysiological recordings. Furthermore, the MPTP model provided an insight into the DBS mechanism. A major discovery was that STN-DBS leads to an increase in the mean firing rates of the GPe and GPi [21], which contradicts the lesioning hypothesis. Therefore, the DBS community gradually shifted its interest to the modulation of the network activity via DBS-induced pathway activation. Despite the clear advantages of non-human primate models, their employment is obstructed by relatively high costs and complex regulations of animal welfare, especially in the European Union. Moreover, non-professional criticism and public opposition, including that beyond legal boundaries [34], discourages researchers from conducting this kind of experiments and provokes the exodus to less-regulated states [35, 36].

1.2.2 Rodent PD model

Small body dimensions, low costs, high reproduction rates, ensuring low inter-individual variability, and the comparability to the human brain-to-body mass ratio make rodent models attractive for *in vivo* and *ex vivo* experiments. Mice are by far the most widely employed in animal research with a variety of transgenic models, including specifically developed for studying the PD pathology [37]. Furthermore, some mice strains were shown to be MPTP-sensitive, which is not the case for rats and hamsters [38]. However, DBS in mice is highly problematic due to the miniature dimensions, and a long-term full implantation has not been conducted yet⁴. In contrast, recent advances in hardware allowed a long-term implantation of the whole stimulating system in rats [40], thus permitting a study of DBS effects in freely moving animals. To imitate the parkinsonian pathology, a 6-hydroxydopamine (6-OHDA) injection is commonly applied. It induces a degeneration of dopaminergic neurons of the nigro-striatal tract and leads to a similar biochemical state and partial resemblance to the behavioral phenotype [41]. The reciprocal translatability of certain findings was demonstrated for 6-OHDA-treated rats and primate PD models, though there were also reports on failed translations [42].

In DBS studies employing rat PD models, the STN is the most common target. However, intentional targeting of specific STN subregions is not pursued due to relatively large stimulating electrodes and limited precision of implantations. Furthermore, dendrites and collaterals of the STN neurons extend over the

⁴In [39], a 30 days continuous stimulation with a fully implanted stimulator was reported. However, it was demonstrated *in silico* with a 1 *kOhm* resistor, which corresponds to impedances measured in human DBS, but not in rodents.

whole structure, and the anatomical differences are less expressed [43]. The major pathways of the STN involved in PD are present in the rodent brain anatomy (see Fig. 1.4), although pallidothalamic projections are not as clearly structured as the ansa lenticularis and the lenticular fasciculus in primates [44].

Stimulation is usually conducted via monopolar or bipolar electrodes placed either directly or cranially (superior) to the target to reduce neurological damage imposed by the implantation. For monopolar electrodes, different grounding methods are applied including a gold wire electrode placed under the scalp or screws in the skull (see Fig. 1.5). In comparison with bipolar electrodes, the monopolar configuration induces a more spherically shaped electric field, which allows better targeting by the stimulation. However, this setup is less stable not only due to possible corrosion and other electrochemical effects occurring on the grounding screws or possible displacement of the grounding wire, but also due to a more intricate current path, which partially leads through low conductive skull areas. The field focalization problem with bipolar electrodes will be discussed in Chapter 3 of this thesis.

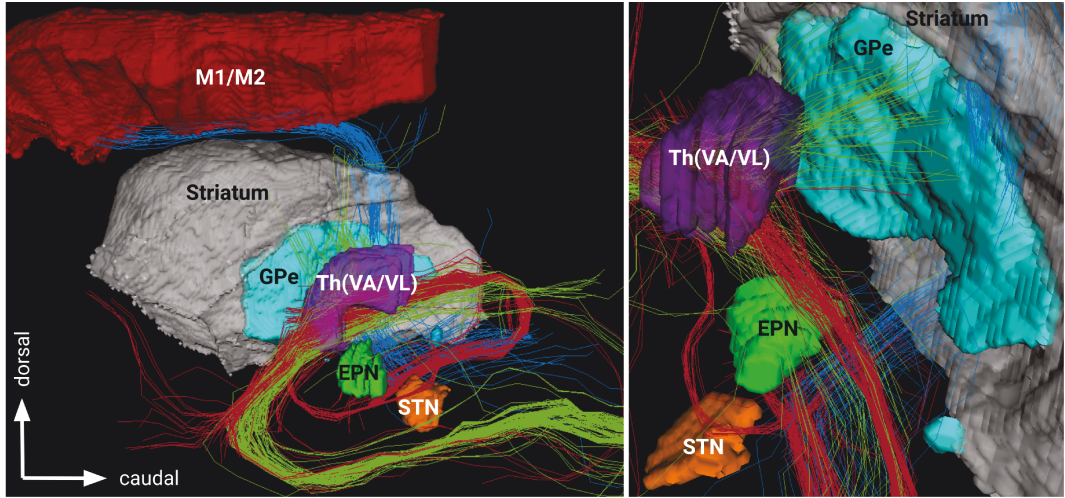


Figure 1.4: Pathways relevant for STN-DBS, reconstructed in the rat brain using a water diffusion imaging data from [45]. The brain structures are visualized using a rat brain atlas [45] (GPe – external segment of the dorsal pallidum, EPN – entopeduncular nucleus (analogue of the GPi in rodents), Th(VA/VL) – ventral anterior and ventral lateral nuclei of the thalamus, STN – subthalamic nucleus, M1/M2 here are the sensorimotor regions of the cortex). The central question of the thesis is whether DBS-induced activation patterns in the hyperdirect (blue), the cerebellothalamic (green) and the pallidothalamic pathways (red) are comparable in human and rat from the modeling perspective.

Rat experiments offer a variety of methods to assess the effect of DBS. To describe the alleviation of PD-like symptoms, multiple behavioral tests were developed, including:

- apomorphine- (or amphetamine)-induced circling in the hemiparkinsonian model, where the number of rotations contralateral to the 6-OHDA-lesioned hemisphere is controlled on a time interval;
- corridor tests to quantify lateralised neglect in the hemiparkinsonian model by placing sugar pellets equidistantly on both sides of the corridor [46];
- open-field tests that evaluate spontaneous mobility and anxiety by measuring total migration distances and the migration distance within the center area [47];
- cylinder tests to assess the reversal of forelimb use asymmetry in the hemiparkinsonian model [48].

In addition, it is possible to conduct electrophysiological measurements including extracellular and intracellular recordings, local field potentials (LFPs), electroencephalography (EEG), electrocorticography (ECoG), electromyography (EMG), magnetoencephalography (MEG) and fMRI, though with a limited resolution. *Post mortem* histological analysis allows quantification of the induced cell proliferation with immunostaining, while Nissl staining [49] is applied to evaluate the dopamine loss and precision of the electrode implantation. Alternatively, the latter can be evaluated based on computed tomography (CT) and MRI data [50, 51] acquired *in vivo*.



Figure 1.5: Schematic depiction of a DBS setup in rats. 1 – DBS electrode, 2 – cables to connect to the pulse generator, 3 – grounding gold wire (note that it is placed outside of the skull), 4 – acrylic mounting, 5 – fixating screw that can be used for grounding. The image is adapted from [47].

Chapter 2

Computational Methods for Deep Brain Stimulation: From Medical Imaging to Neural Activation

Before we further examine the DBS-induced modulation of neural activity in PD, it is necessary to introduce computational methods to evaluate the generated electric field and its impact on neural tissue. Note that these methods are not restricted to PD, or even DBS, as they follow general principles of physics and biophysics. In this chapter, we will also discuss the relevance of model complexity in theoretical and clinical studies, and highlight challenges pertinent to rodent DBS modeling. Finally, I will present an open-source simulation platform that is applicable for fundamental research involving complex computational analysis, including uncertainty quantification as well as patient-specific modeling.

2.1 DBS-induced electric field in brain tissue

Current applied through electrode contacts generates an electric field while passing over the brain tissue. In this section, we discuss the underlying physical and mathematical description of the process and address issues of the current conduction in brain, with a subsection dedicated to the electrode–tissue interface.

2.1.1 Mathematical Formulation

Four *Maxwell's equations* describe the phenomenon of electromagnetic fields in time and space. Let us consider two of them: *Ampère's* and *Faraday's laws* in the corresponding differential forms [52]

$$\nabla \times \mathbf{H}(\mathbf{r}, t) = \frac{\partial}{\partial t} \mathbf{D}(\mathbf{r}, t) + \mathbf{J}(\mathbf{r}, t), \quad (2.1)$$

$$\nabla \times \mathbf{E}(\mathbf{r}, t) = -\frac{\partial}{\partial t} \mathbf{B}(\mathbf{r}, t), \quad (2.2)$$

where $\mathbf{E}(\mathbf{r}, t)$ and $\mathbf{H}(\mathbf{r}, t)$ denote the electric and magnetic field strengths, $\mathbf{D}(\mathbf{r}, t)$ and $\mathbf{B}(\mathbf{r}, t)$ are the electric and magnetic flux densities, respectively, and $\mathbf{J}(\mathbf{r}, t)$ represents the current density. In brain tissue, the natural current sources are negligible in comparison with DBS signals, and therefore we consider only the conduction current $\mathbf{J}(\mathbf{r}, t) = \sigma(\mathbf{r})\mathbf{E}(\mathbf{r}, t)$, where $\sigma(\mathbf{r})$ is the electrical conductivity of the material, i.e. of the brain tissue. The fluxes can be expressed via fields with the following constitutive relations [53]:

$$\mathbf{D}(\mathbf{r}, t) = \varepsilon_0 \mathbf{E}(\mathbf{r}, t) + \mathbf{P}(\mathbf{r}, t), \quad (2.3)$$

$$\mathbf{B}(\mathbf{r}, t) = \mu_0 \mathbf{H}(\mathbf{r}, t) + \mu_0 \mathbf{M}(\mathbf{r}, t), \quad (2.4)$$

where ε_0 and μ_0 are the vacuum permittivity and permeability, respectively. The polarization field $\mathbf{P}(\mathbf{r}, t)$ and the magnetization field $\mathbf{M}(\mathbf{r}, t)$ depend on tissue properties: the relative permittivity $\varepsilon_r(\mathbf{r})$ and the relative permeability $\mu_r(\mathbf{r})$

$$\mathbf{P}(\mathbf{r}, t) = \varepsilon_0(\varepsilon_r(\mathbf{r}) - 1)\mathbf{E}(\mathbf{r}, t), \quad (2.5)$$

$$\mathbf{M}(\mathbf{r}, t) = (\mu_r(\mathbf{r}) - 1)\mathbf{H}(\mathbf{r}, t). \quad (2.6)$$

Thus, Eq. 2.3 can be rewritten as $\mathbf{D}(\mathbf{r}, t) = \varepsilon_0 \varepsilon_r(\mathbf{r}) \mathbf{E}(\mathbf{r}, t) = \varepsilon(\mathbf{r}) \mathbf{E}(\mathbf{r}, t)$, where $\varepsilon(\mathbf{r})$ is the permittivity of the tissue. Applying the divergence operator ($\nabla \cdot$) to Eq. 2.1, we utilize the vector calculus identity $\nabla \cdot (\nabla \times \mathbf{X}) = 0$ and write the expression in terms of the electric field assuming no time dependence of the tissue properties:

$$0 = \nabla \cdot (\varepsilon(\mathbf{r}) \frac{\partial}{\partial t} \mathbf{E}(\mathbf{r}, t) + \sigma(\mathbf{r}) \mathbf{E}(\mathbf{r}, t)), \quad (2.7)$$

Though explicit time modeling is possible, it significantly increases the computational effort. Instead, we can represent the physical quantities in terms of harmonic oscillations [54]:

$$\mathbf{E}(\mathbf{r}, t) = \Re(\underline{\mathbf{E}}(\mathbf{r}) e^{j\omega t}), \quad (2.8)$$

where j is the imaginary unit, $\omega = 2\pi f$ denotes the angular frequency and $\underline{\mathbf{E}}(\mathbf{r}) = \mathbf{E}(\mathbf{r})e^{j\phi}$ is the complex amplitude, where ϕ is the phase angle of the cosine function. Here, f does not refer to the repetition rate of the DBS signal (often around 80–200 Hz), but to a frequency of a sine wave signal, which is extracted by decomposition of the DBS signal using a Fourier transform (see Fig. 2.1 and Fig. 2.2). In the notation of harmonic oscillations and after dividing both sides by $e^{j\omega t}$, *Ampère's* and *Faraday's laws* are transformed to

$$0 = \nabla \cdot ((j\omega\varepsilon(\mathbf{r}) + \sigma(\mathbf{r}))\underline{\mathbf{E}}(\mathbf{r})), \quad (2.9)$$

$$\nabla \times \underline{\mathbf{E}}(\mathbf{r}) = -j\omega\underline{\mathbf{B}}(\mathbf{r}). \quad (2.10)$$

The electric field is generated by a current delivered by the DBS system that either sets electric potentials on the electrode contacts to a fixed value or

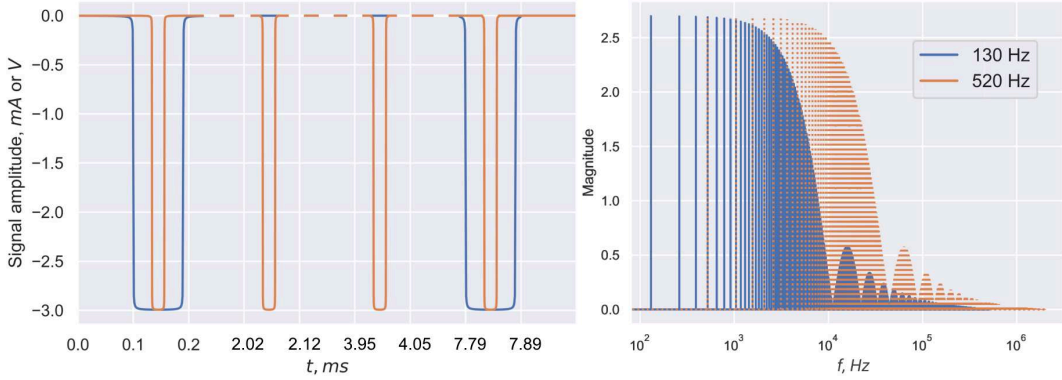


Figure 2.1: Rectangular DBS signals with different repetition rates (left, note the time lapse) and the magnitude of their power spectra (right). The contribution of individual frequency components is important in the context of dispersive dielectric properties of brain tissue.

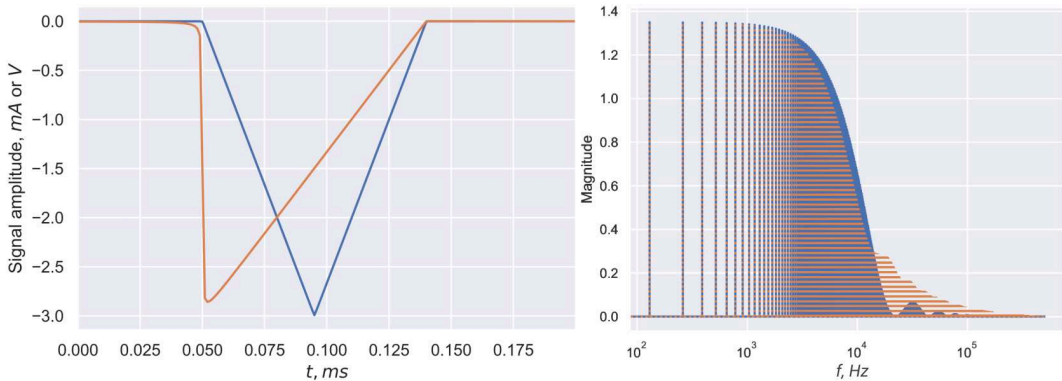


Figure 2.2: Alternative triangular DBS signals with a 130 Hz repetition rate (left) and the magnitude of their power spectra (right). Note that the signal depicted in orange is cropped due to the inappropriately large time step.

adjusts them over the pulse. So, the actual given value (or the boundary condition, in terms of numerical methods) is for the electric potential, but not the electric field. Furthermore, the DBS effect on neural excitation is defined in terms of altered extracellular electric potential when solving the Hodgkin-Huxley cable equation. Therefore, it is reasonable to reformulate the equations above for the electric potential.

Since magnetic monopoles do not exist, the magnetic flux density is defined as $\underline{\mathbf{B}}(\mathbf{r}) = \nabla \times \underline{\mathbf{A}}(\mathbf{r})$, where $\underline{\mathbf{A}}(\mathbf{r})$ is the magnetic vector potential. Using Eq. 2.10, we describe the electric field strength in terms of potentials

$$\underline{\mathbf{E}}(\mathbf{r}) = -j\omega\underline{\mathbf{A}}(\mathbf{r}) - \nabla\varphi(\mathbf{r}), \quad (2.11)$$

where $-\nabla\varphi(\mathbf{r})$ is the electrostatic component of the electric field. Note that the inclusion of this term does not contradict Eq. 2.10 due to the vector calculus identity $\nabla \times (\nabla \mathbf{X}) = 0$.

Computations in brain tissue can be further simplified due to criteria formulated by Robert Plonsey and Dennis Heppner [55]. Firstly, we can assume that the electric field changes instantly throughout the domain, i.e. propagation effects are absent if

$$\omega\sqrt{\mu\varepsilon(1 + \frac{\sigma}{j\omega\varepsilon})}R_{\max} \ll 1, \quad (2.12)$$

where μ is the magnetic permeability set to that of the free space ($1.257 \cdot 10^{-6} \text{ H/m}$) since brain tissue does not demonstrate magnetic properties. R_{\max} is the largest brain dimension $\approx 180 \text{ mm}$. Let us consider the high frequency case. For typical DBS signals, power spectrum components above 1 MHz are negligibly small (see Fig. 2.1), and at this frequency the brain conductivity σ and permittivity ε are roughly⁵ 0.2 S/m and $4.4 \cdot 10^{-9} \text{ F/m}$, respectively. This estimates the propagation factor at 0.023, but one should bear in mind that contributions of such high frequency components are not significant. For a conventional DBS signal with a 130 Hz repetition rate, the component of this frequency will contribute the most, and the corresponding propagation factor is 0.0002 with σ and ε estimated as 0.13 S/m and $8.854 \cdot 10^{-7} \text{ F/m}$.

Furthermore, Plonsey and Heppner showed that if the criterion to omit propagation holds true, the inductive effect of the magnetic field can also be neglected, as its criterion is just the squared value of the former. This allows to

⁵Details on the estimation of the dielectric tissue properties in the DBS power spectrum will be presented in the following section.

drop time derivatives of the magnetic field and finally obtain *Laplace's equation* for the electro-quasistatic approximation of *Maxwell's equations*

$$-\nabla \cdot (\sigma(\mathbf{r}) + j\omega\varepsilon(\mathbf{r}))\nabla\varphi(\mathbf{r}) = 0. \quad (2.13)$$

2.1.2 Brain tissue properties

It was previously mentioned that in DBS modeling the endogenous currents in the extracellular space of the brain are usually neglected, and the only electrically active elements are the electrode and the stimulator casing, often used for grounding. The DBS current can be supplied in two modes: voltage-controlled and current-controlled, where the voltage driven by the stimulator is adjusted over time to achieve the desired currents through the electrode contacts. In the past, voltage-controlled stimulation was the standard mode, partially due to safety issues. However, with the development of reliable stimulating systems, the current-controlled mode gained the attention of the clinical community. Its advantage is a compensation for the voltage drop over the electrode–tissue interface, which will be discussed at the end of this section.

In case of PD treatment, both modes commonly employ a rectangular pulse of 30–120 μs with a repetition rate of 80–200 Hz , and the amplitude is usually determined empirically during clinical evaluations. The pulse is followed by a long and low amplitude train signal (see Fig. 2.3) that balances the injected current⁶. Alternatively, a symmetric biphasic pulse can be used. In recent years, novel shapes of varying complexity were proposed, e.g. triangular and Gaussian pulses [56, 57], but these were not established across multiple clinical facilities.

Fig. 2.4 shows the power spectrum of a 130 Hz 60 μs rectangular pulse and the dielectric properties of brain tissue across the spectrum according to [58]. It can be noted that the tissue demonstrates a prominent electrical dispersion, i.e. $\sigma=\sigma(\mathbf{r},\omega)$ and $\varepsilon=\varepsilon(\mathbf{r},\omega)$, and that the capacitive term of Eq. 2.13 contributes considerably for the parameters given in [58]. The dispersive effect necessitates the application of the Fourier Finite Element method (FFEM) [62] that involves

1. computing the electric potential distribution in the frequency domain with the corresponding values of the dielectric properties;
2. scaling the solutions with the Fourier Transform of the DBS pulse;
3. applying the Inverse Fourier Transform to obtain a solution in the time domain.

⁶In this thesis, we disregard the charge balancing train assuming its negligible effect on the neural tissue.

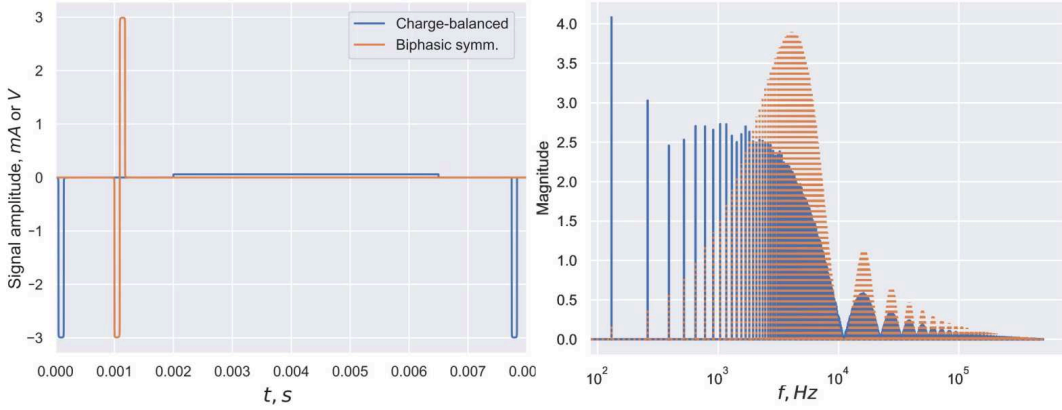


Figure 2.3: Two types of charge balancing for a 130 Hz DBS signal (left) and the magnitude of their power spectra (right). Note the shift to higher frequencies for the biphasic symmetric pulse. The left plot also illustrates the ratio of the pulse width to the signal period.

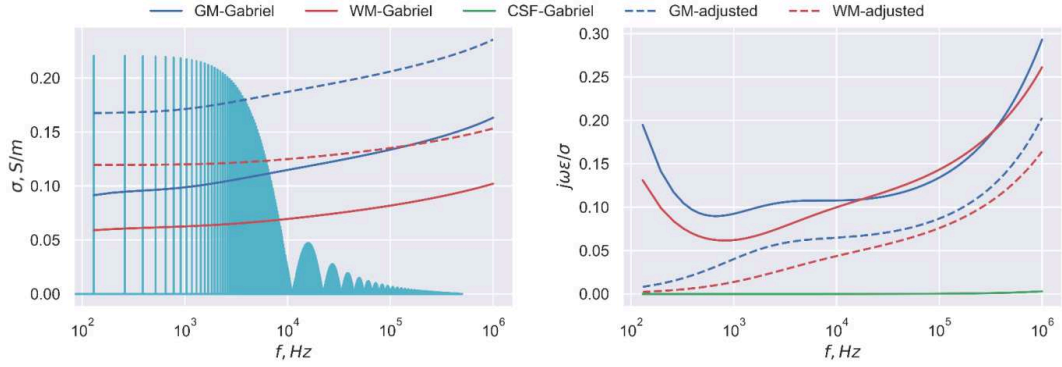


Figure 2.4: Dielectric properties of the main brain tissue types in the frequency domain. The dispersive values were taken from Gabriel et al [58], but adjusted by omitting the α -dispersion as proposed in [59] and additionally upscaled to match the grey and white matter electrical conductivities at 50 kHz, computed as the mean of the values reported in [58] and [60]. **Left:** electrical conductivity of the tissue (CSF conductivity is not dispersive and ≈ 2 S/m) and the magnitude of the power spectrum for the 130 Hz DBS signal (shown in teal on the background). **Right:** relative contribution of the capacitive term in the Laplace's equation depending on the brain tissue. Note that the omission of the α -dispersion significantly reduces the capacitive contribution at low frequencies.

To avoid multiple field computations in the frequency domain, different techniques were proposed [61, 63], and in this thesis we employ an octave band approximation (see Fig. 2.5) that drastically reduces the number of computations and does not require extensive preliminary estimations, while accurately describing the dispersive behavior of brain tissue.

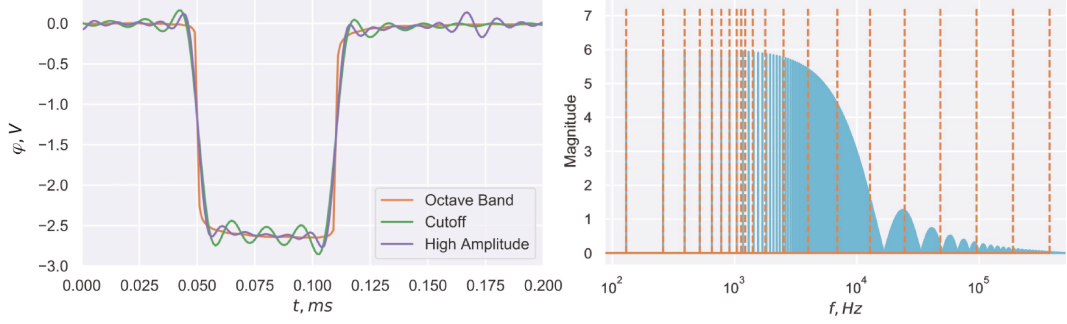


Figure 2.5: Tissue-voltage response for different DBS power spectrum approximation methods [61] when solving the electroquasistatic formulation of Maxwell’s equations. Here, the cutoff method picks the first 500 frequencies in the spectrum, while the high amplitude method picks 500 frequencies with the largest contribution. The octave bands deployed over the power spectrum starting from 1040 Hz are shown on the right (orange dash). The idea is to compute the field distribution only for one frequency in the band and extrapolate on the rest. Evidently, the octave band method is more efficient and accurate approximation. Note the voltage growth over the pulse due to the capacitive charging.

The significance of the capacitive contribution remains debatable. Although its omission affects the computed electric field and, subsequently, the neural activity, the magnitude of the error is highly dependent on the DBS setup and the choice of the quantification metric for the DBS effect. For example, the error is practically negligible in studies where the extent of the stimulated tissue is estimated by the thresholding of the electric potential derivatives. Furthermore, it was suggested that α -dispersion (below 1 kHz) had been overestimated in [58] due to the electrical double layer effects [59], and the proposed correction significantly reduces the tissue capacitance (dash lines in Fig. 2.4). In addition, the solution of Eq. 2.13 in complex numbers poses an additional computational challenge. Therefore, numerous studies approximate the electric potential distribution with the quasistatic formulation of *Laplace’s equation*:

$$-\nabla \cdot (\sigma(\mathbf{r}, \omega) \nabla \varphi(\mathbf{r})) = 0. \quad (2.14)$$

The difference in the voltage-tissue response and the equivalent circuits for both formulations as well as for the static case (no electrical dispersion) are presented in Fig. 2.6.

The brain conductivity varies considerably depending on tissue type. For simplicity, it is customary to categorize the tissue into grey matter (which comprises brain nuclei and includes somas, axons, dendrites, and glial cells),

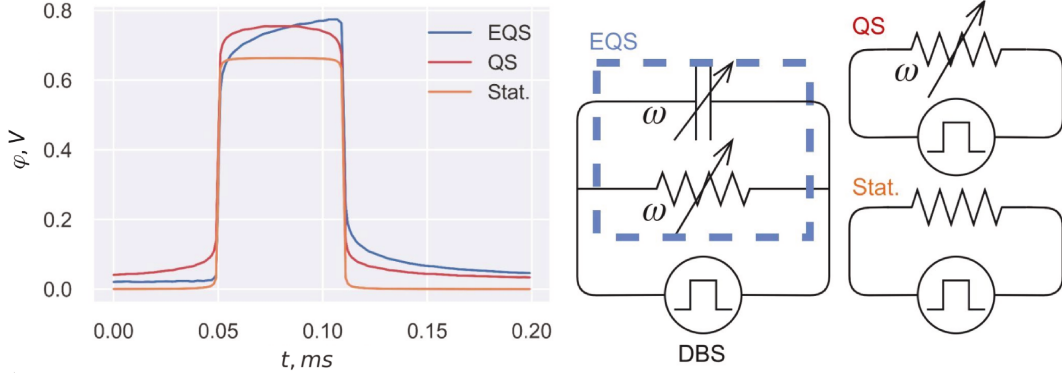


Figure 2.6: Three formulations for modeling the DBS-induced field in brain tissue. **Left:** tissue-voltage response during the constant current stimulation solved for the dielectric properties of grey matter [58]. The electro-quasistatic formulation clearly demonstrates a capacitive charging effect, while the stationary model, where dispersion is neglected, shows a lower tissue resistance (the conductivity is assessed at the median frequency of the power spectrum of 130 Hz 60 μ s rectangular signal). Insignificant rippling occurs due to the truncation of the spectrum. **Right:** equivalent circuits of the formulations. The image is taken from the author’s book chapter [64] with a permission of the publisher.

white matter (bundles of myelinated axons) and cerebrospinal fluid⁷ (CSF), see Fig. 2.7. The latter has a very prominent effect on the electric field distributions (see Fig. 2.8), since its conductivity is one order of magnitude higher than that of the grey and white matter, the conductivities of which are comparable, though the former is consistently reported to be 1.5–2 times higher [58, 65]. However, a precise estimation of white matter conductivity is ambiguous due to its highly anisotropic nature (Fig. 2.7, right): measurements along fiber bundles yield up to nine times larger values than the transverse measurements [66].

Furthermore, it can be generally stated that no precise values for brain tissue are available at the moment. One meta study [65] clearly shows significant variations that cannot be solely attributed to the individual differences of organisms. While numerous techniques for conductivity extraction were proposed, their applicability is strictly limited. Among the studies reviewed in [65], the approach proposed by Koessler et al [60] is of a special interest in the context of this thesis. Apart from *in vivo* impedance measurements, which can be conducted via an implanted DBS electrode, the method performs fitting using a segmentation of brain tissue, which is an inherent part of DBS modeling. The difficulty of the method lies in attaining a proper placement of recording contacts that should reside in a homogeneous medium, e.g. grey matter. Moreover, the applicability of the method is limited when investigating

⁷Though anatomically incorrect, it is common to classify blood content as CSF in the context of dielectric properties to simplify segmentation routines.

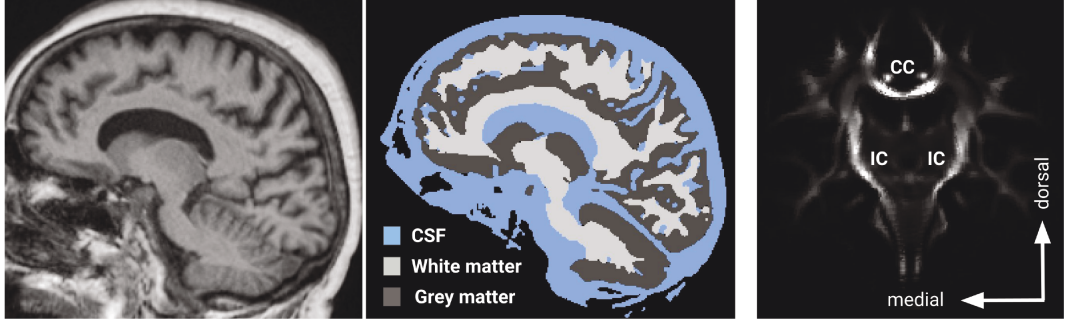


Figure 2.7: Example of medical imaging data required for a detailed volume conductor model. **Left:** T1-weighted (longitudinal relaxation time) MRI sequence allows to clearly visualize myelinated tissue (white matter) as high intensity regions, while CSF appears dark. **Center:** a segmentation of the brain tissue with distinctly different electrical conductivities. **Right:** the distribution of the anisotropic tissue, visualized using the IIT human brain atlas [67]. The intensity corresponds to the magnitude of the voxel-wise normalized water diffusion tensor data. Here, the anisotropy is especially prominent in the corpus callosum (CC) and the internal capsule (IC), which passes in the vicinity of the STN.

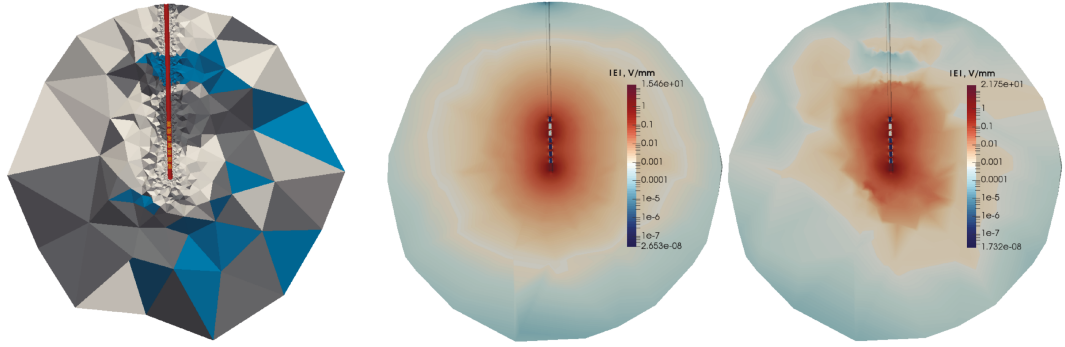


Figure 2.8: Effect of complexity of a volume conductor model. Note that for DBS modeling, a brain geometry can be usually approximated with an elliptic or spherical domain. **Left:** a segmentation of brain tissue mapped onto an FEM mesh. Grey and white matter are depicted in the corresponding colors, CSF in blue, encapsulation layer (scar tissue formation) in red and the highly conductive electrode contacts in orange (the rest of the electrode is assumed to be insulated and removed from the volume conductor model). A precise mapping in the whole domain is often not required, especially for bipolar stimulations, where the current path is confined to the vicinity of the electrode contacts. **Center and right:** the distribution of the electric field magnitude (log scale) in homogeneous isotropic and heterogeneous anisotropic volume conductor models, respectively.

anisotropic tissue. It is important to note that conductivity values at 50 kHz reported in [60] and [58] are inconsistent: 0.360 S/m vs 0.128 S/m for grey matter and 0.190 S/m vs 0.078 S/m for white matter, respectively. Fig. 2.4 presents a possible approximation derived from [58] with the omission of the

α -dispersion and a scaled conductivity to match the mean of the original [58] and [60] data at 50 kHz .

Although numerous studies neglected anisotropy when modeling DBS, its effect on the conductivity and consequently the electric field distribution has been demonstrated to be substantial [64, 68, 69]. It is especially prominent when modeling activation in white matter fibers, which are the main source of anisotropy in brain tissue. In volume conductor models, the anisotropic effect is implemented by expressing conductivity in terms of voxel-wise defined tensors Σ , and the simplest approach is to assume that the conductivity along fiber tracts is nine times greater than in the transverse direction, while treating the rest of the tissue as isotropic. However, this binary dependence of the conductivity on fiber directionality not only introduces large interpolation errors, especially at fiber crossings, but also requires a rigorous fiber tracking analysis. Alternatively, conductivity tensors can be assessed based on diffusion-weighted MRI imaging (DWI) (Fig. 2.7, right), where a pulsed-gradient spin echo is applied to estimate the mobility of water molecules in the tissue. Tuch et al [70] have shown that "... in a structured medium such as tissue the two processes are related through mutual respect for the boundary conditions imposed by the tissue geometry." The tensor is defined as

$$\Sigma = \mathbf{V}_D \Lambda_{\text{scaled}} \mathbf{V}_D^T, \quad (2.15)$$

where \mathbf{V}_D is a matrix composed of eigenvectors of diffusion tensors \mathbf{D} , and Λ_{scaled} is a diagonal matrix that contains scaled eigenvalues λ of \mathbf{D} . These diffusion tensors are extracted from DWI based on the assumption that a Gaussian process underlies the diffusion [71], and this modality was named diffusion tensor imaging (DTI) [72]. To estimate Λ_{scaled} , or the ratios of its components if the isotropic conductivity σ_{iso} is given, different methods had been proposed that were collected in a comparative study [73]. In [74], it was suggested to use a direct transformation based on the mean diffusivity:

$$\Sigma = \frac{3\sigma_{\text{iso}}}{\text{trace}(\mathbf{D})} \mathbf{D}. \quad (2.16)$$

Another method, described in [75], utilizes a volume conservation concept. If the isotropic conductivity is described as a sphere, its anisotropic form is represented by an ellipsoid, and their volumes must be equal, i.e.

$$\sigma_k = \frac{\sigma_{\text{iso}} \lambda_k}{\sqrt[3]{\lambda_1 \lambda_2 \lambda_3}}, \quad (2.17)$$

where σ_k is the k -th eigenvalue of the conductivity tensor. For both of these methods, it is necessary to determine σ_{iso} , and therefore it is desirable to have a comparable resolution for the segmented MRI and the DWI/DTI data.

Fig. 2.9 shows an elliptical representation of scaled tensors for a unit isotropic conductivity.

Other methods were developed to infer conductivity directly from the diffusive tissue properties. Tuch et al [70] proposed an expression to link microstructural diffusivity and conductivity:

$$\sigma_k = \frac{\sigma_e}{d_e} \left(\frac{d_k^2 d_i}{3d_e^2} + d_k \left(\frac{d_i}{3d_e} + 1 \right) - \frac{2d_i}{3} \right), \quad (2.18)$$

where σ_e and d_e are the microscopic extracellular conductivity and diffusivity coefficient, respectively, and d_i is the coefficient of the microscopic intracellular diffusivity; values for all three are provided in [70]. Lastly, [73] suggested an analytical expression that describes the anisotropic conductivity using ratios of diffusion tensor eigenvalues while preserving the impedance in the infinite conductive medium.

A comparison of the listed methods and their limitations is beyond the scope of this thesis. I should note that an optimal method (which is yet to be developed) should describe the effect of water diffusion on the tissue impedance, carefully extracted from the total measured impedance, and should at the same time account for the electrical dispersion of brain tissue in the DBS power spectrum. In this thesis, the volume conservation approach proposed in [75] is employed, if not stated otherwise.

In clinical application: To my knowledge, there are no clinical groups that routinely measure brain dielectric properties of DBS patients. Hence, the values for white matter, grey matter and CSF are usually taken from the literature. Nevertheless, the difference in the brain anatomy must be accounted for, and this is why medical imaging is employed. It has become customary

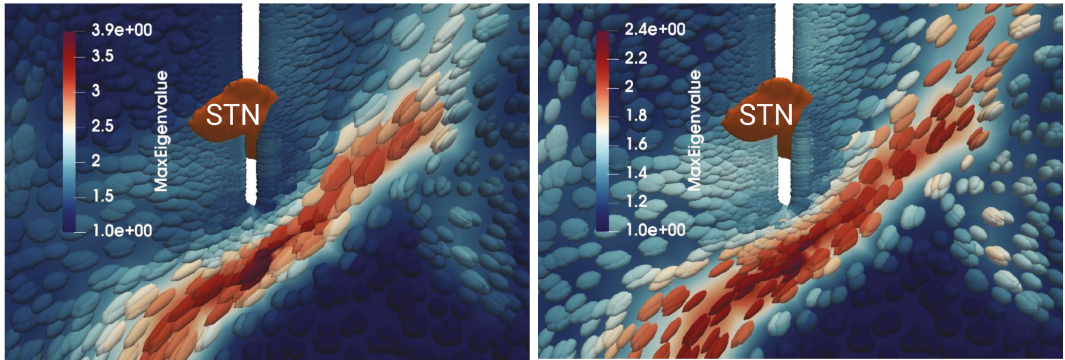


Figure 2.9: An example of elliptic representation of conductivity tensors in the vicinity of the STN obtained using [75] and [74] scaling methods, respectively. Note that the former yields a higher anisotropy (see the colorbars). The image is taken from the author's book chapter [64] with a permission of the publisher.

to acquire patient-specific MRI and CT data for surgery planning and electrode localization, while DWI data acquisition is relatively rare but might be conducted in studies on brain circuits or tumor formation. However, the resolution of these data is usually far below that applicable for accurate volume conductor modeling. Therefore, it is enhanced with digitalized atlases of the human brain, such as [76, 77]. A high resolution atlas is non-linearly transformed into the patient-space, and its segmentation is used to describe the distribution of the brain tissue *ergo* the dielectric properties. In theoretical studies aimed to formulate hypotheses on DBS mechanisms it might be justified to normalize patient data to the atlas space, but, in this case, a non-linear transformation, i.e. distortion, of the electrode geometry is required, which might be impractical for automated simulation pipelines.

If patient-specific DWI/DTI data are not available, a diffusion data atlas, e.g. [67], can be employed instead. Apart from conductivity tensors' derivation, DTI is used for the reconstruction of white matter fibers when the activation of specific pathways is investigated. For instance, the activation of the internal capsule during DBS is associated with side-effects such as motor contractions and dysarthria, and it is relatively simple to reconstruct the structure using patient-specific DTI data. Thinner and intertwined fiber bundles can be resolved using high angular resolution diffusion imaging (HARDI). In Chapter 4, I will present an example of how fiber trajectories can be extracted based on diffusion imaging.

In rodent research: The capabilities of the currently available MRI technology are limited with regard to the *in vivo* acquisition of images of a sufficient resolution. Apart from artifacts caused by respiratory activity there are legal limitations concerning the duration of animal exposure to the MRI-generated magnetic field. The issues are circumvented by an *ex vivo* acquisition, but there is a change in brain properties due to ventricle shrinking and overall loss of water content. Furthermore, to achieve an acceptable resolution ($< 100 \mu m$), costly radiofrequency coils are required, discouraging some research groups from acquiring data on their own. On the other hand, the differences in the brain anatomy of animals of the same strain, age and weight can be disregarded to a certain extent (for a further discussion please refer to [78]). As a result, a volume conductor model is usually designed based on rodent brain atlases, e.g. [45, 78, 79, 80], some of which have already been employed to plan the electrode trajectory. The latter can be validated using CT images [51] following the same routine as for the electrode reconstruction in human DBS [12]. It should be noted that a precise implantation to the rodent STN/EPN is challenging, as even minor misplacements might lead to a significant stimulation of non-targeted nuclei [61]. The miniature brain dimensions additionally complicate the tissue specific conductivity measurements described in [60], although results for incorrectly placed electrodes can be discarded by *ex vivo* tissue analysis.

2.1.3 Electrode–tissue interface

Apart from the brain tissue, volume conductor models for DBS often incorporate the electrode–tissue interface that might account for a significant voltage drop. The interface arises from two distinct processes: a biological process, which forms an encapsulation layer around the implanted electrode, and an electro-chemical process on the electrode–electrolyte film. Encapsulation is a foreign body response, which is more prominent for stiff implants. Two phases of encapsulation can be distinguished [81]. Up to 4 weeks after the implantation, the layer is in the acute phase, associated with edema, bleeding, microglial activity and degeneration of neurons (Fig. 2.10). Clinical DBS is not applied during this phase. The chronic phase is characterized by glial scarring and a decrease in neural density, while the observed thickness of the chronic encapsulation layer varies considerably [82, 83]. Moreover, the data reported for the dielectric properties of encapsulation are also heterogeneous, with a strong dependence on the electrode position, choice of measuring contacts, and postimplantation time [84]. The general trend is an increase of the impedance during the scarring process and stabilization after 3–6 months [81]. Furthermore, both clinical and animal studies report that the impedance is reversibly decreased on the active contacts during DBS [84, 85, 86].

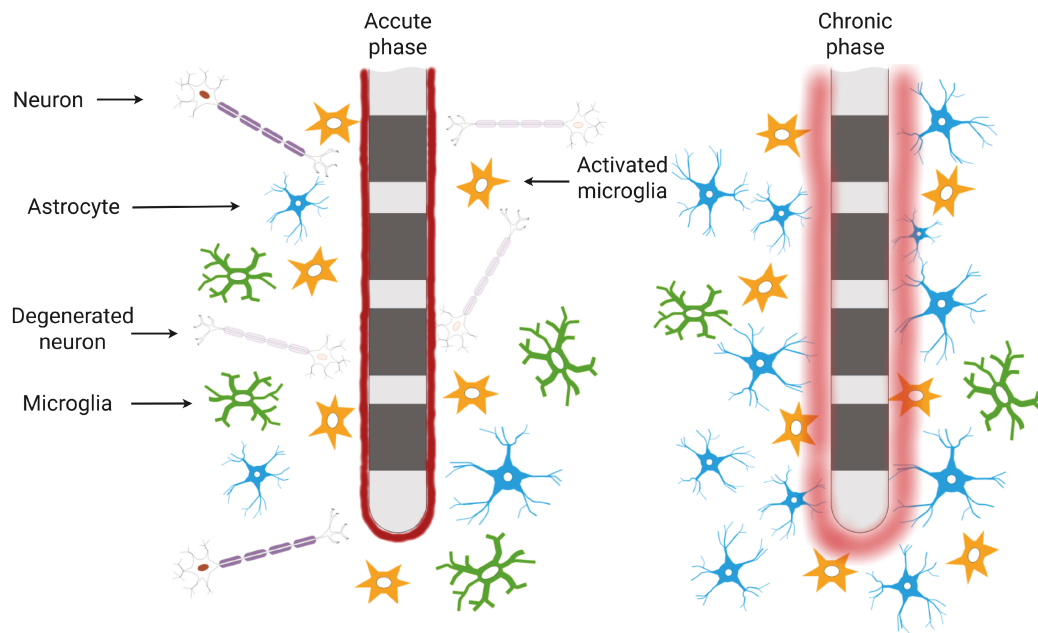


Figure 2.10: *Phases of encapsulation layer around an implanted electrode (not a realistic scale). **Left:** the acute phase is characterized by a microglial activation and degeneration of neurons. The electrode surface is covered by blood and cerebrospinal fluid. **Right:** in the chronic phase, the electrode is encapsulated by glial scarring formed by reactive astrocytes, while the neuron density is decreased.*

An electrode–electrolyte film occurs on the surface of electrode contacts due to the electron-ion interaction (Fig. 2.11, top right). The effects on the film can be described by non-faradaic reactions, where currents are induced by charging and discharging of the electrical double layer, and faradaic reactions, where a direct current flow occurs due to a reduction and oxidation [87]. Surely, faradaic reactions must be minimized to avoid metal deposition to the brain tissue and electrode damage. For this reason, highly polarizable platinum/iridium electrodes are employed instead of stainless steel designs. For grounding electrodes, where the active surface is significantly larger, the effects on the film are minor.

For a monopolar stimulation, a commonly used equivalent circuit for the electrode–tissue interface is presented in Fig. 2.11. Bipolar or multipolar cases have a more complex circuit representation of the encapsulation layer, but its dimensions allow explicit modeling with FEM. The non-faradaic and pseudocapacitive reactions are described by a constant phase element (CPE) [88] with the impedance defined as $Z_{\text{CPE}} = K(j\omega)^{-\beta}$, where K is the scaling factor

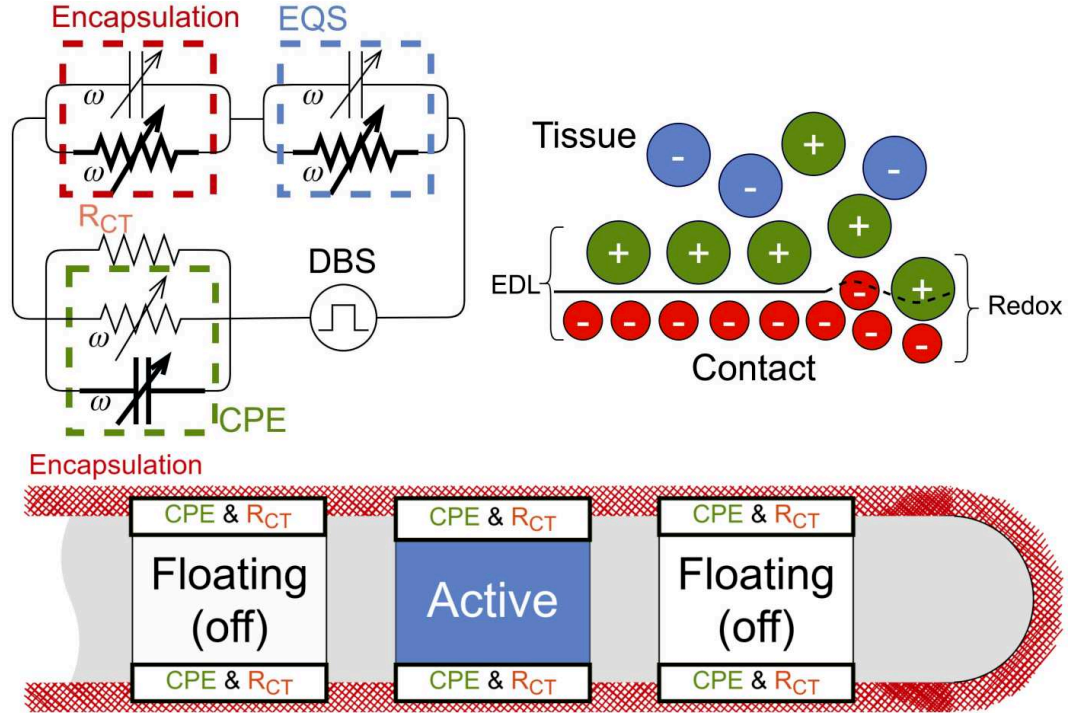


Figure 2.11: *Electrode–tissue interface. Top left:* the equivalent circuit of the interface for monopolar stimulation with highlighted dominating elements. **Top right:** a depiction of the electrical double layer and the charge transfer on the metal–electrolyte interface due to an electron-ion interaction. **Bottom:** the interface components on a DBS electrode. Note that the interface also occurs on inactive contacts that are sometimes used for measurements. The image is adapted from the author’s book chapter [64] with a permission of the publisher.

of the CPE, and β describes the capacitive contribution (for $\beta = 1.0$, CPE acts as a pure capacitor). These parameters depend on the electrode material, geometry and surface roughness. Moreover, the parameters become frequency dependent at high voltages due to specific adsorption effects [89], and in [90] a significant decrease of K and β was shown after two weeks of DBS in a non-human primate. A charge transfer R_{CT} , which describes faradaic reactions, is derived using the Butler-Volmer equation [88] and defined by multiple parameters such as temperature, overpotential, transfer coefficients, etc. Faradaic reactions are the main contributor to non-linearity on the interface [91], and their quantification is a complex problem. Still, for moderate currents delivered via platinum/iridium electrodes, Faradaic reactions are minor. Therefore, in DBS modeling it is common to represent the electrode-electrolyte film only with Z_{CPE} .

The contribution of the encapsulation layer and the electrode-electrolyte film to the total impedance is significant [81, 90, 92, 93] and, more importantly, fluctuates during a long-term DBS [94]. This poses a problem for voltage-controlled stimulation, since a fluctuating voltage drop on the electrode-tissue interface affects the electric field in the neural tissue. As mentioned previously, current-controlled mode is more resilient against these fluctuations, hence it has become more accepted in clinical and computational research. Nevertheless, it is important to track the voltage and current driven by the stimulator, not only with regard to the battery run-time, but also to ensure the safety of patients. The charge density of $30 \frac{\mu C}{cm^2}$ per phase is usually referred to as the upper limit of a safe stimulation [95], which nearly corresponds to 10 V for a 90 μs rectangular pulse injected via a conventional DBS electrode. Naturally, this limit should be decreased for novel current-steering electrodes with smaller contact surfaces *ergo* higher impedances.

In clinical application: Time-varying effects of the electrode-tissue interface on the treatment efficacy motivated a transition to the current-controlled mode, which computational model does not require simulating the electrode-electrolyte film. And even though CPE incorporation is rather simple, its parameters for specific electrode models and voltages are not comprehensively described. The encapsulation layer usually requires explicit modeling: not only it reshapes the electric field distribution during a multipolar stimulation, but it also defines an area of neurodegeneration. Based on a review study [81] it can be concluded that further research on the encapsulation is required. In clinics, total impedance measured for standardized stimulation protocols is monitored in order to detect a possible malfunctioning of the hardware.

In rodent research: Significantly higher impedances of rodent electrodes severely restrict the applied voltage if the $30 \frac{\mu C}{cm^2}$ limit is to be complied with. Moreover, the applicability of this limit is questionable considering the size difference of the human and rodent electrodes. In a study using platinum/iridium

leads, 100 μA 60 μs pulses did not lead to any observable damage in a rat brain [96]. Nevertheless, safe amplitudes for a particular electrode model should be defined with an *in vitro* assessment of the electrode-electrolyte film, followed by a preliminary animal trial and a subsequent histological analysis, the findings of which will also broaden our knowledge about the encapsulation layer. It should be noted that rodent DBS is usually conducted in the monopolar current-controlled mode, which is why the impedance of the encapsulation layer has a minor effect [61].

2.2 DBS-induced neural activity

It is important to point out that this section does not elaborate on the neural mechanism of DBS in neurodegenerative disorders; this problem will be addressed in the next chapters. Instead, we discuss how a DBS-induced electric field affects neural structures in general and present concepts that were proposed to quantify the effect.

2.2.1 Biophysics of action potential

The first thorough mathematical description of action potential initiation and propagation was proposed in the seminal work by Alan Hodgkin and Andrew Huxley [97]. When conducting experiments on squid giant axons⁸, they discovered three current sources that determine the change of the membrane potential V_m :

$$I_m = C_m \frac{\partial V_m}{\partial t} + \underbrace{g_K(V_m - E_K)}_{I_K} + \underbrace{g_{Na}(V_m - E_{Na})}_{I_{Na}} + \underbrace{g_L(V_m - E_L)}_{I_L}, \quad (2.19)$$

where I_m is the total membrane current, C_m is the membrane capacitance, g_K and g_{Na} are the time and voltage dependent potassium and sodium conductances, with all four quantities defined per unit length. The passive leak through the membrane (mostly mediated by Cl^- ions) is described by the conductance g_L . E_K , E_{Na} and E_L are the shifted Nernst equilibrium potentials. If I_m is large enough, e.g. due to a current injection, it will depolarize the neuron membrane enough to activate Na^+ channels, which, in turn, will further boost the membrane depolarization (see Fig. 2.12). Shortly after, the Na^+ channels start to inactivate, while efflux of K^+ ions and processes at leak channels will drive the decrease of V_m , and, eventually, the membrane will be repolarized. The whole phenomenon was named action potential (AP), and it can be

⁸These axons, used by squids for water jet propulsion, are literally gigantic: up to 1.5 mm in diameter. For comparison, the largest mammalian axons are only 20 μm .

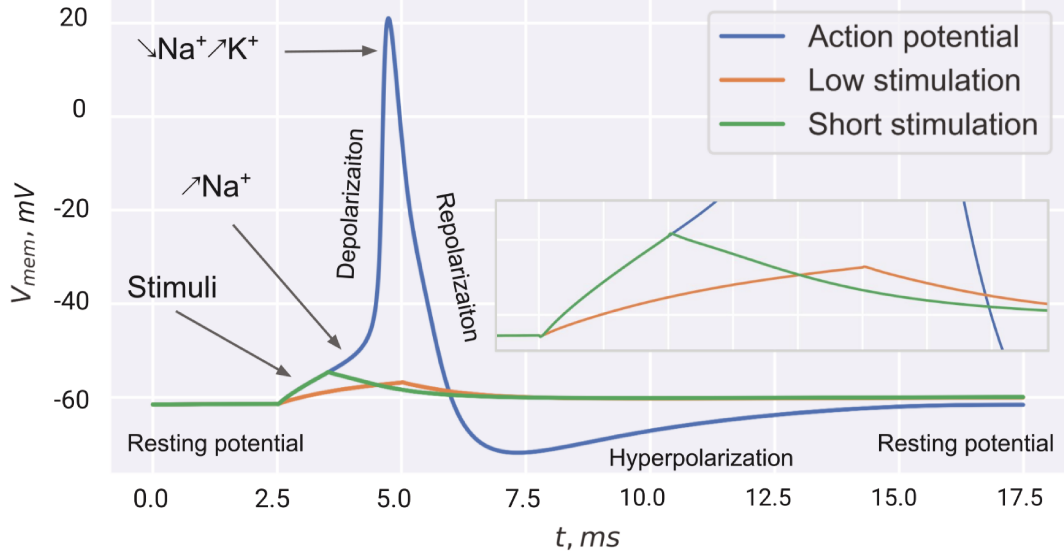


Figure 2.12: Action potential initiation in response to a current injection. The resting potential (here ≈ -60 mV) is a relatively constant membrane potential that originates from differences in membrane permeabilities of ions.

considered as a binary event⁹, i.e. it follows the ‘all-or-none’ principle. APs are the main means of communication between neurons: propagating down the axon, they cause a release of neurotransmitters into the synaptic clefts at the axon terminals, and the receptors of post-synaptic cells might respond to the influx of neurotransmitters with a further activation of ion channels. A faster alternative to this chemical mechanism is the electric synapse where the current of the pre-synaptic cell is transmitted directly via a gap junction.

The propagation of an action potential along the axon is described by the Hodgkin-Huxley cable equation:

$$C_m \frac{\partial V_m}{\partial t} = \frac{1}{r_a} \frac{\partial^2 V_i}{\partial x^2} - I_K - I_{Na} - I_L, \quad (2.20)$$

where V_i refers to the intracellular potential and r_a is the axial resistance. Note that under electrostimulation, APs might also propagate antidromically (towards the cell body) and even invade upstream collaterals [98].

The squid giant axons, investigated by Hodgkin and Huxley, are not myelinated, and the derived model can be further extended to describe the electrodynamics of dendrites and cell bodies (somas). Vertebrates also have axons covered in myelin – a lipid layer that serves as insulation¹⁰ (see Fig. 2.13). These axons are exposed to the extracellular field at nodes of Ranvier, which

⁹In this thesis, we consider a neuron activated by DBS if it elicits an AP in response to the induced extracellular field.

¹⁰Myelin is actually the main content of white matter in the central nervous system.

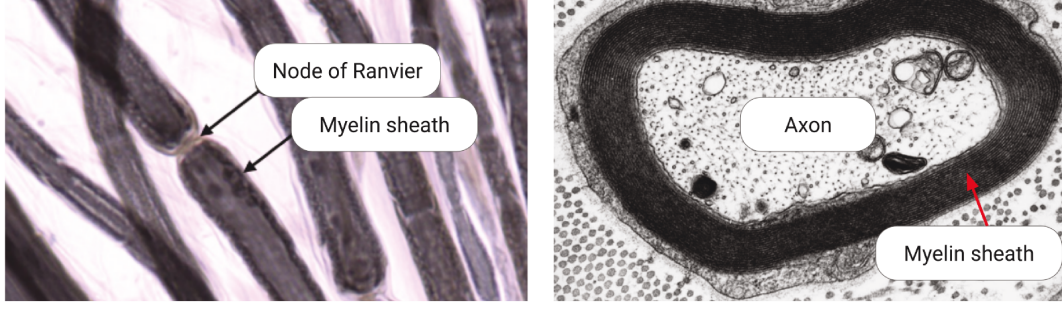


Figure 2.13: *Electron microscopy of myelinated axons. Left: nodes of Ranvier are located at the gaps of myelination. Right: a cross-section of a myelinated axon. The images are taken from [102].*

contain Na^+ and K^+ channels. In myelinated axons, APs propagate via saltatory conduction: the depolarization "jumps" from node to node resulting in a significant speed gain (120 m/s vs 1 m/s), while demyelination leads to numerous diseases, the most known of which is multiple sclerosis. The effect of an induced extracellular electric field on myelinated axons is the central subject of STN-DBS modeling: in Rhesus monkeys it was shown that this type of axons covers 40% of the STN surface [99]. Moreover, they demonstrate a significantly higher excitability [100, 101], which makes them a primary DBS input for neural modulation.

2.2.2 Computational modeling of neurons

A mathematical description for myelinated axons was formulated by Bernhard Frankenhaeuser and Andrew Huxley based on experiments with toads [103]. Using nodal conductances assessed in that work, Donald McNeal developed the first computational model to study the effect of extracellular stimulation [104] (see Fig. 2.14). In the model, a perfect insulation was assumed for the myelinated segments due to the computational limitations of the hardware of that time. With this assumption, and substituting the second spatial derivative with the second order centered finite difference as well as the term for intracellular potential at node n with the corresponding membrane, extracellular and resting potentials ($V_{i,n} = V_{m,n} + V_{e,n} - V_r$), Eq. 2.20 can be rewritten as

$$\frac{\partial V_m}{\partial t} = \frac{1}{C_m} (G_a (V_{m,n-1} - 2V_{m,n} + V_{m,n+1} + V_{e,n-1} - 2V_{e,n} + V_{e,n+1}) - I_K - I_{Na} - I_L), \quad (2.21)$$

where G_a is the axial internodal conductance. Based on this equation, Frank Rattay later proposed an activating function depending on $\frac{\partial^2 V_e}{\partial x^2}$ [105] for nerve fibers.

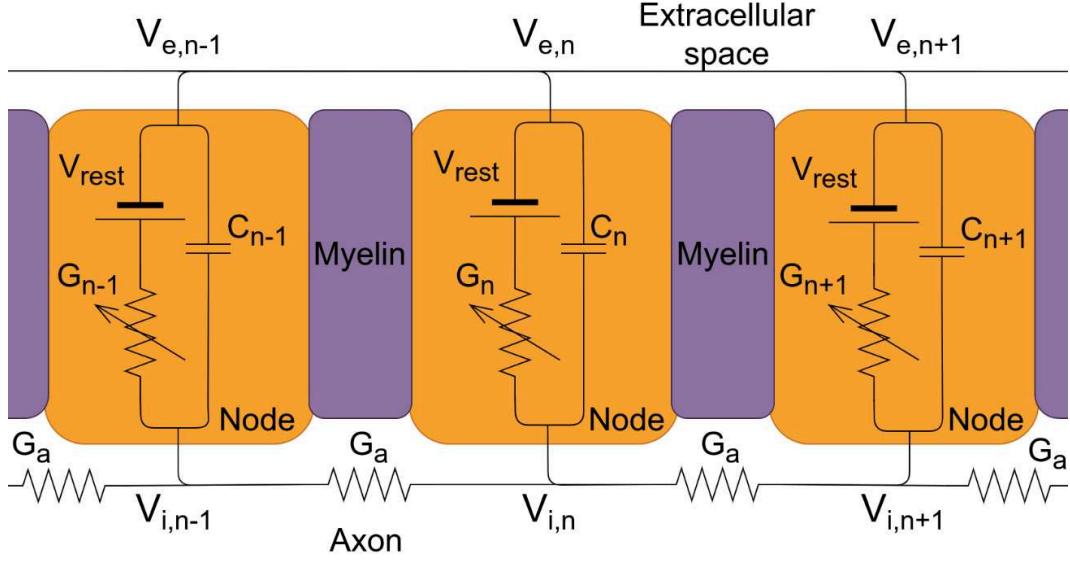


Figure 2.14: *McNeal's circuit representation of a myelinated axon [104] composed of three components: the ideally insulating myelin sheath (violet), the nodes of Ranvier (orange) and the axon itself. The conductances and capacitances are marked with the corresponding subscripts, where the nodal conductance $G_n = (I_K + I_{Na} + I_L)/V_m$. V_{rest} and V_e denote the resting and the extracellular potentials. Note that in McNeal's model, the nodal parameters correspond to the membrane parameters in Eq. 2.21.*

For simple geometries, the presented equations can be solved analytically. However, the math becomes very cumbersome for realistic neural geometries, and time derivatives should be treated with special methods, e.g. Green's functions. Alternatively, for complex geometries and fine analyses of AP propagation, an FEM model of a neuron can be employed [106, 107]. It is also possible to integrate such a neuron model into the volume conductor model, thus explicitly incorporating the contribution of neural activity to the extracellular field, which might be important for studies focused on ephaptic coupling and source reconstruction. Yet, this tailoring requires the employment of multiscale techniques, and even for modern machines such FEM computations are relatively expensive when simulating large populations of neurons. A significant reduction of computational costs can be achieved by composing a neuron with simply shaped compartments for which discrete neural properties are defined. In this case, a simulation is conducted using finite difference methods that efficiently incorporate time domain modeling, e.g. with Crank–Nicolson based integrators [108] and the tridiagonal matrix algorithm, in contrast to an expensive matrix inversion required at each time step in FEM. Among several finite difference simulators developed for neural modeling, NEURON [109] stands out for its popularity in the neuroscientific community. It was achieved due to the "natural syntax" of the software that encapsulates the technical implementation, allowing users to work on complex neural mechanisms with-

out a deep understanding of the underlying computational and programming basis. The software supports various algorithms that promote the efficiency of the simulations, such as adaptive integration and parallel computing, while conducting new studies is facilitated by a large database of verified projects.

Based on McNeal’s concept, different electrostimulation models of myelinated axons had been developed, and some of them were qualitatively compared in a comprehensive survey study [110]. Among them, the model most commonly used in the computational DBS community is McIntyre’s double cable model of mammalian nerve fibers [111] (Fig. 2.15). To avoid a further immersion in neurophysiology, I will spare the details and describe only the prominent features of it. The model was developed after advances in computer technology that allowed the simulation of explicitly myelinated segments including internodal, paranodal and juxta-paranodal compartments with specific geometrical and electrical parameters. The exact morphology was defined for discrete fiber diameters starting from $5.7 \mu m$, and was later extrapolated to thinner fibers. Such a detailed modeling of myelinated axons was suggested to accurately reproduce a passive depolarization after action potentials. The model was developed based on experimental evidence from human, cat and rat neurophysiological studies and later adopted to predict the activation in fiber tracts composed of large diameter axons, e.g. the internal capsule [112]. Among the models analyzed in the survey, McIntyre’s model demonstrated a prominently higher excitability by electrostimulation.

It could have been noted that the scope of this section gradually shifted from neurons to axons. In the context of fibers of passage, e.g. the internal capsule, only axonal compartments of neurons experience significant $\frac{\partial^2 V_e}{\partial x^2}$ to elicit APs. When considering local cells, it can be generally assumed that axons are more excitable than somas¹¹ [101] due to a higher density of Na^+ channels [114]. Furthermore, in some cases DBS activates predominantly GABAergic afferents due to their higher excitability [115], thus boosting the inhibition of the cell bodies [116]. In [117], it was shown that DBS can decouple the somatic and axonal activity, thus prioritizing simulation of the DBS effect on axons when modeling the disruption of the pathological PD pattern in the basal ganglia-thalamo-cortical network.

2.2.3 Quantification concepts of induced activation

A commonly employed concept for quantification of DBS-induced neural activation is the volume of tissue activated (VTA) [64, 118]. The idea is to arrange axons in a grid centered at the active electrode contacts, to solve the

¹¹In Chapter 3, we will investigate electrostimulation effects of DBS on soma with dendrite trees using a rat STN projection neuron model from [113].

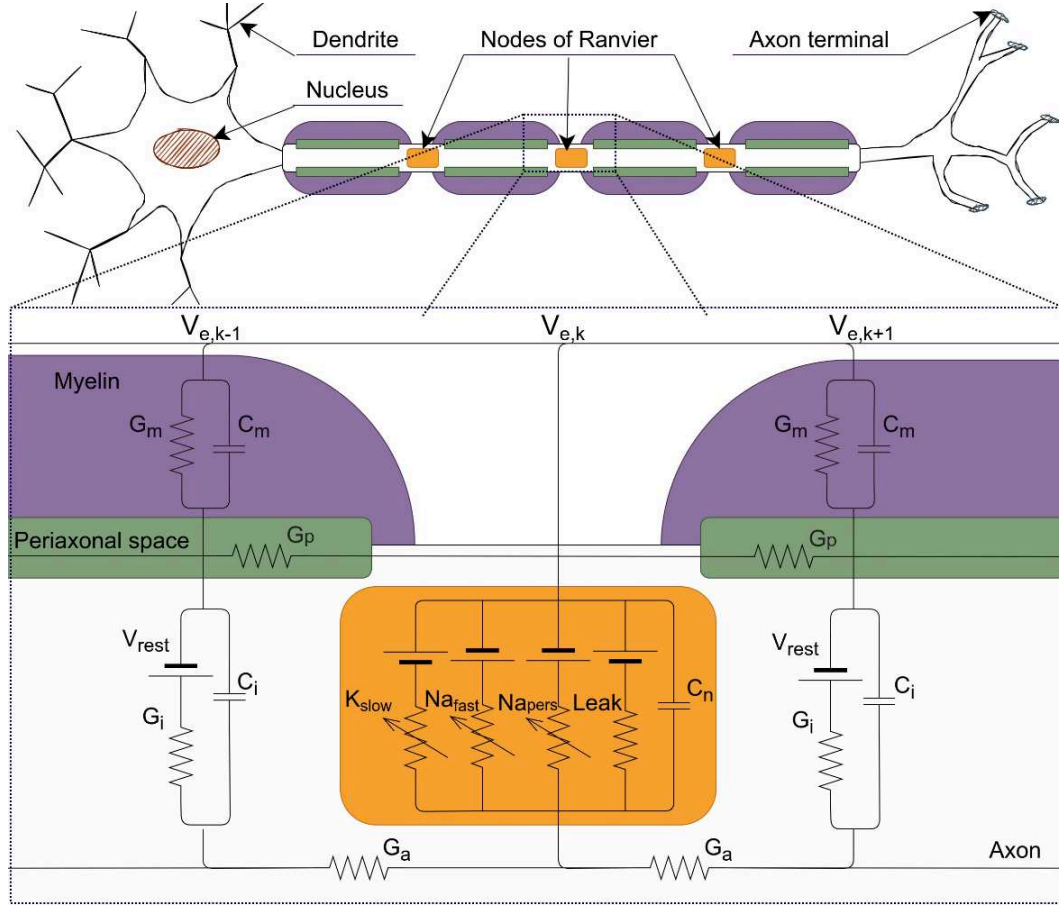


Figure 2.15: Artistic sketch (top) and circuit representation (bottom) of a mammalian myelinated axon composed of five components: the myelin sheath (violet), the periaxonal space (green), the internodal axolemmas, the nodes of Ranvier (orange) and the axon itself. The conductances and capacitances are marked with the corresponding subscripts. V_{rest} and V_e denote the resting and the extracellular potentials. The voltage-gated ion channels at the nodes of Ranvier include slow potassium K_{slow} , fast and persistent sodium channels Na_{fast} and Na_{pers} in parallel to a non-specific leakage. The image is taken from the author's book chapter [64] with a permission of the publisher.

cable equation for a given distribution of the extracellular potential in time and space and to extract an activation contour. The contour is then rotated and a volume is obtained. In homogeneous and isotropic volume conductor models, a VTA has a cylindrical symmetry along the electrode axis (see Fig. 2.16, top row). For heterogeneous and anisotropic cases, the contours might differ drastically depending on the direction of the axons, thus it is reasonable to compute multiple VTAs. To reduce the computational effort, different approximations were proposed that do not require to solve the cable equation. Most of them are based on the activating function $\frac{\partial^2 V_e}{\partial x^2}$, e.g. in [119] activation thresholds were defined for $|\nabla \cdot \mathbf{E}|$ based on the pulse width and its amplitude,

and in [120] the activation extent was estimated using the Hessian matrix for the electric potential. In [119], it was also observed that the electric field magnitude $|\mathbf{E}|_2$ could predict the activation for monopolar stimulation protocols. Though disputable, this metric became widely employed due to its relative simplicity. For more details on VTA and its approximation, please refer to my book chapter [64].

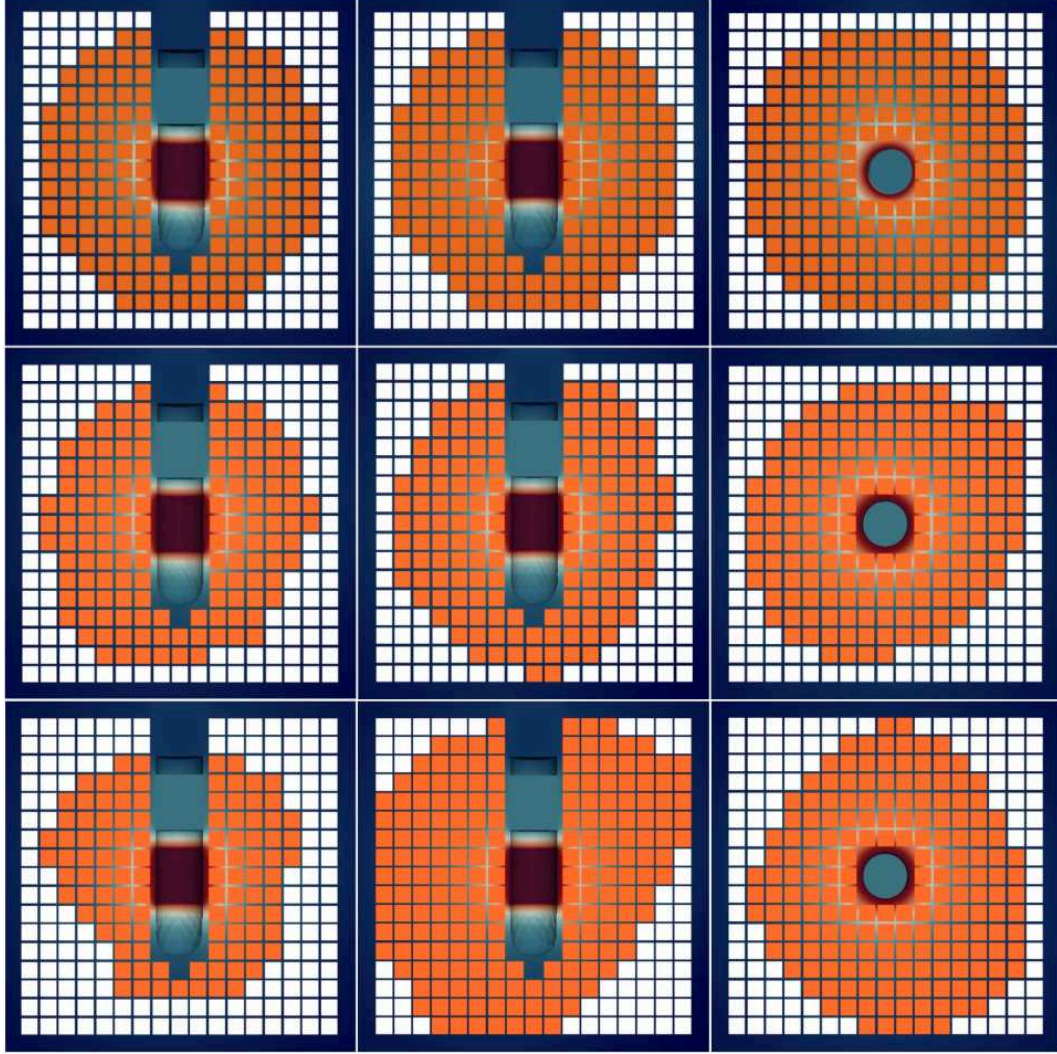


Figure 2.16: Activation extent of a monopolar stimulation computed with different volume conductor models. From left to right: activation contours for coronal, sagittal and axial planes, respectively. Volume conductor models from top to bottom: homogeneous isotropic, heterogeneous, heterogeneous and anisotropic (diffusion tensors were normalized using the volume conservation method). Note that the homogeneous isotropic model returns a cylindrically symmetric activation contour. The image is adapted from the author’s book chapter [64] with a permission of the publisher.

The drawback of these approximation methods is that they do not account for the extracellular current contribution on distant nodes of Ranvier. As a consequence, modified driving force (MDF) methods were considered [121, 122]. These methods estimate the activation at node k as $\sum_{i=0}^n \eta_{|k-i|} \Delta^2 V_{e,i}$, where n is the total number of nodes of Ranvier, $\Delta^2 V_{e,i}$ is the second order centered finite difference of the extracellular electric potential at node i and $\eta_{|k-i|}$ is the weight inversely proportional to the distance from the k -th node ($\eta_{i=k} = 1.0$). While activation thresholds were computed with some differences, both methods define weights dependent on the fiber diameter and the pulse width using McIntyre's axon model to simulate intracellular current injections and the observed decay of $|V_{m,i}|$ relative to $|V_{m,k}|$. However, in [122] it is stated that MDF methods require adjustments of the activation thresholds depending on the axon trajectory and the electric field configuration, hence significantly obstructing their application.

A faster VTA estimation in comparison with cable equations is not the only reason behind the development of MDF methods. Since their activation assessment is not localized but based on $\Delta^2 V_{e,i}$ at multiple nodes, the methods can be directly extended to compute the activation of realistically placed axons. It is obvious that arrangement of axons in a grid for VTA is a solely computational concept that does not reflect the real neuroanatomy. While it is suitable to quantify activation of relatively straight fiber bundles, e.g. the corticofugal pathway in the vicinity of the STN, a VTA prediction is dubious when multiple fiber tracts of complex trajectory are considered (see Fig. 2.17).

Developments in the brain imaging technology, in particular DWI and fiber tractography, enabled the extraction of these trajectories. To estimate the effect of DBS on realistically allocated axons, the pathway¹² activation modeling (PAM) was proposed [124]. This concept requires to compute the field distribution in a detailed volume conductor model that incorporates anisotropy, which is the most prominent along white matter fibers. Compartments of axon models are seeded on these fiber trajectories, and hence the cable equation is solved for a realistic distribution of V_e . It is important to distinguish PAM and activation volume tractography, where fibers are considered activated when intersecting with VTAs [12, 125].

In clinical application: With the DBS software development, e.g. Lead-DBS, GUIDETM XT, SureTuneTM, the estimation of VTA became a well-established protocol to assist surgery planning and programming of stimulators. Numerous medical articles were published that utilized VTA to define "sweetspots" for specific PD and dystonia symptoms [126, 127, 128, 129, 130].

¹²In this context, a pathway represents a group of fibers that establish the same structural and functional connectivity. For example, fibers of the hyperdirect pathway descend from the motor cortical regions directly to the STN and provide an excitatory input.

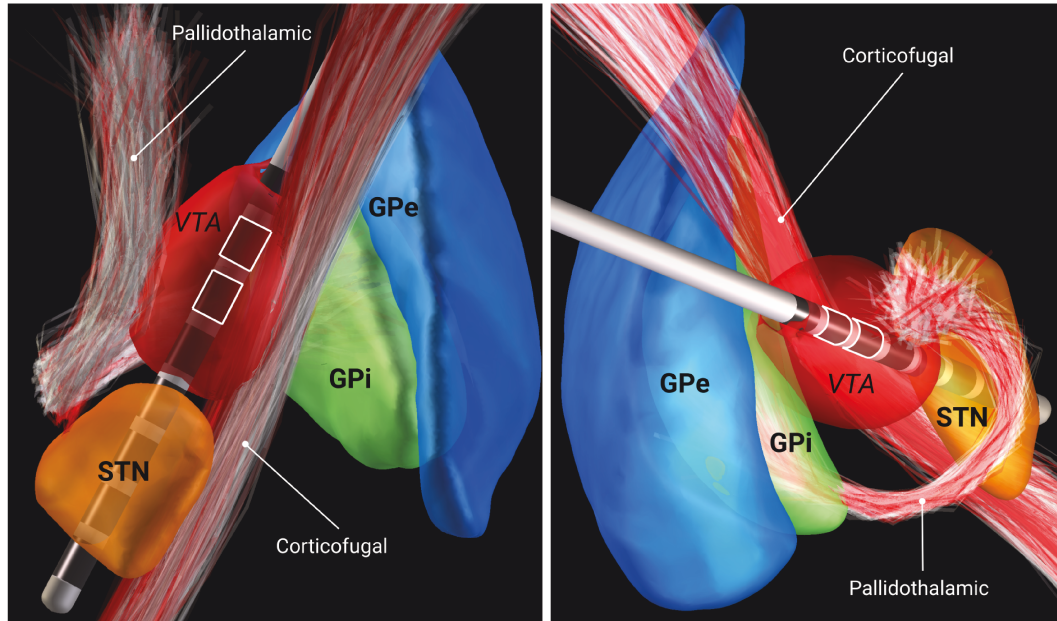


Figure 2.17: Modeling the effect of bipolar DBS on the extent of neural recruitment in the pallidothalamic and corticofugal fibers with $|\mathbf{E}|_2$ -based approximation of volume of tissue activated (VTA) and pathway activation modeling. The active electrode contacts are highlighted. Marked in red are the fibers predicted to be activated by the pathway activation modeling. Note that for the corticofugal pathway, the VTA approximation overlaps mostly with the red fibers, which is not the case for the pallidothalamic tract that swirls around the electrode. Fiber trajectories are taken from [123].

While pre-operative and post-operative studies can employ relatively expensive volume conductor models and cable models to accurately quantify neural activation, intraoperative analyses rely on VTA approximation methods, including artificial neural networks [131]. PAM only recently started to gain the attention of the clinical community and still faces rational skepticism. Apart from the scarcity of patient-specific fiber data, predictions based on PAM are limited by the accuracy of fiber tractography and pathway classification, while a higher computational effort, in comparison with VTA modeling, requires appropriate hardware resources. It is yet a task for computational scientists to demonstrate the relevancy of PAM for clinical application, and I will attempt to do so in Chapter 4.

In rodent research: For the STN, the density of neurons in primates and rodents is comparable, while somas of projecting neurons are 2-3 times smaller [132]. Rodent corticofugal fibers, directly affected by DBS in the basal ganglia, are thinner [133] and thus less excitable (more losses through the myelin sheath). The same is expected for other involved pathways, and which is why higher current densities might be required to achieve the same relative

activation extent, though one should beware of the high impedance limitations described in the previous section. No fundamental methodological difference exists between primates and rodents for VTA and PAM computations, but the latter is less applicable as rodent DWI and fiber tractography data are limited.

2.3 Finite Element Method

2.3.1 FEniCS

In this section, we will often refer to FEniCS¹³ [134], the most established open-source tool for the solution of partial differential equations. It is a C++ based software that offers a Python interface, thus combining high efficiency and accessibility. While reading this section, you will notice that FEniCS functionality does not fully cover all FEM capabilities. Yet, it is sufficient to calculate a DBS-induced electric field in an adequate and accurate manner. Besides, the software developers offer a profound support and further enhancements of FEniCS to meet the requirements of the ever growing community.

2.3.2 FEM formulation

Although the electromagnetic field theory is well-formulated for analytical methods, its application is problematic for irregular geometries and inhomogeneous material properties. Among the different numerical techniques developed in the last century the Finite Element Method (FEM) received a wide recognition for solving realistic problems defined on complex domains. Here, I outline an application of the method for the considered field modeling problem based on a relevant textbook [135]. The idea is to discretize these complex domains with finite elements (in 3-D: usually tetrahedrons or hexahedrons, but also their curved analogs) and to solve the mathematical formulation on their entities (vertices, edges, etc.). The general form of an FEM problem can be expressed as:

$$\mathbf{L}[f(\mathbf{r})] = s(\mathbf{r}), \quad (2.22)$$

where \mathbf{L} is an arbitrary differential operator (the Laplace operator $\nabla \cdot \nabla$ in our problem), s is the source (which is absent in *Laplace's equation*) and $f(\mathbf{r})$

¹³FEniCS stands for Finite Element Computation Software, originally compiled at the University of Chicago, whose mascot is a phoenix.

is the sought-for function, $\varphi(\mathbf{r})$ in our problem. The function is expanded in n number of basis functions $\psi(\mathbf{r})$:

$$f \approx \sum_{i=1}^n f_i \psi_i(\mathbf{r}), \quad (2.23)$$

where f_i is an unknown coefficient that has to be determined. The basis function $\psi_i(\mathbf{r})$ is a polynomial associated with a mesh entity i in such a manner that it is non-zero only on mesh elements containing this entity. Its form depends on the sought-for function, and FEM offers suitable options for most of the mathematical models. For example, a nodal polynomial approximation is appropriate for scalar field calculations. In case of vector field computations, nodal functions will generate nonphysical solutions, also called spurious modes [135], and therefore other finite element functions, e.g. (curl) or Raviart-Thomas, should be considered instead.

Since numerical analysis provides an approximated solution, the residual r should be introduced as

$$r = \mathbf{L}[\sum_{i=1}^n f_i \psi_i(\mathbf{r})] - s. \quad (2.24)$$

Naturally, the residual should be minimized, which is achieved by a so-called weak formulation:

$$\int_{\Omega} w_j(\mathbf{r}) r \, d\Omega = \int_{\Omega} w_j \left(\mathbf{L}[\sum_{i=1}^n f_i \psi_i(\mathbf{r})] - s \right) d\Omega = 0, \quad (2.25)$$

where Ω is the computational domain (in our case brain or its approximation) and w_j is a weighting function. There are different methods to choose its type, and for the particular problem we will follow the Galerkin method, where the weighting function matches the basis function on all entities ($w_j(\mathbf{r}) = \psi_j(\mathbf{r})$) except those with a given solution, where weighting of the residual is not required and thus $w = 0$. Since the sought-for function is the scalar field of the electric potential, we employ the nodal based Lagrange polynomials (Fig. 2.18) defined on tetrahedral FEM elements to approximate cylindrical and spherical surfaces of DBS electrodes. Alternatively, an efficient geometry approximation can be achieved with curved elements, but the support of such entities is limited. By applying necessary initial and boundary conditions, the unknown coefficients f_i are determined and the numerical solution for the whole domain is computed.

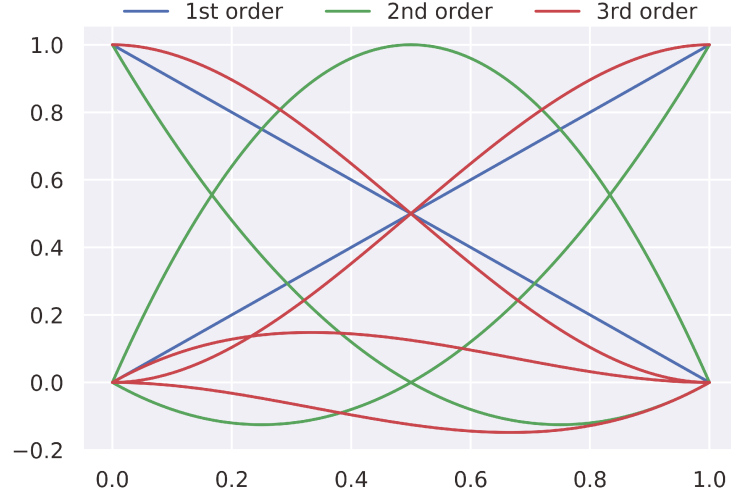


Figure 2.18: *Lagrange basis functions of different order.*

For the electro-quasistatic formulation of *Laplace's equation*, the weak formulation is

$$-\sum_{i=1}^n \underline{f}_i \int_{\Omega} \underline{\kappa} (\nabla \cdot (\nabla \underline{\psi}_i(\mathbf{r})) \underline{\psi}_j(\mathbf{r})) \, d\Omega = 0, \quad (2.26)$$

where $\underline{\kappa} = \sigma(\mathbf{r}, \omega) + j\omega\varepsilon(\mathbf{r}, \omega)$ is the complex conductivity (or the tensor of complex conductivity). We assume that the tissue properties are constant within one element¹⁴, and thus $\underline{\kappa}$ can be taken out of the divergence operator. The same holds true for the term $\sum_{i=1}^n \underline{f}_i$, and, since the \underline{f}_i is a constant defined on the corresponding basis function, it can be taken out of the integral. Integrating Eq. 2.26 by parts we obtain:

$$-\sum_{i=1}^n \underline{f}_i \left(\int_{\Gamma} \nabla \underline{\psi}_i(\mathbf{r}) \underline{\psi}_j(\mathbf{r}) \cdot \mathbf{n} \, d\Gamma - \int_{\Omega} \underline{\kappa} (\nabla \underline{\psi}_i(\mathbf{r}) \cdot \nabla \underline{\psi}_j(\mathbf{r})) \, d\Omega \right) = 0, \quad (2.27)$$

The first term is defined at the boundary of the computational domain and includes the electrode contacts (active and floating), the electrode insulation and the brain surface (or its approximation). The solution at the active contacts is imposed by the Dirichlet boundary condition, and since it is known,

¹⁴This assumption imposes additional restrictions on the element size, since high resolution MRI data will be significantly distorted when mapping on a coarse mesh.

the weighting function nullifies the term. Floating potentials can be simulated in different ways [136], but the following conditions should be fulfilled:

$$\int_{\Gamma_F} \underline{\kappa} \nabla \underline{\varphi}(\mathbf{r}) \cdot \mathbf{n} \, d\Gamma_F = 0, \quad (2.28)$$

$$\underline{\varphi}(\mathbf{r}) = \text{constant on } \Gamma_F, \quad (2.29)$$

i.e. all current that enters will also leave the conductor. We follow the virtual permittivity method [136], which simulates floating conductors as volumes of high conductivity and permittivity. The method does not require any additional term in the weak formulation or direct manipulation of the FEM system, but it introduces inhomogeneity to the system matrix, which might lead to ill-conditioning. We determined empirically that the method is applicable for DBS modeling, but it restricts the choice of FEM solvers; this aspect will be discussed later in the section.

The insulation of the electrode simply means that the current does not flow through the surface, i.e. $\underline{\kappa} \nabla \underline{\varphi}_i \cdot \mathbf{n} = 0$ on Γ_{Ins} , which is the homogeneous Neumann boundary condition. The boundary of the brain surface can be considered insulated, e.g. simulating a low conductive skull tissue. Of course, it is a rough approximation, but if the current flows only through the electrode contacts, and if the computational domain is large enough, the field distortions in the region of interest (where neuron models are allocated) will be negligible. Alternatively, the homogeneous Dirichlet boundary condition ($\underline{\varphi}_i = 0$ on Γ_{Gr}) can be imposed to simulate grounding by the stimulator casing.

The rest of Eq. 2.27 can be rewritten in the matrix form:

$$\mathbf{S}\mathbf{f} = \mathbf{0}, \quad (2.30)$$

where \mathbf{S} is the stiffness matrix, which contains the integrals given in the equation. Where the Dirichlet boundary condition for the electric potential is given, \mathbf{f}_{bc} can be easily calculated, and the rest entries are determined by solving the system of linear equations, in the matrix form:

$$\mathbf{f}_j = -\mathbf{S}_j^{-1} \mathbf{S}_{\text{bc}} \mathbf{f}_{\text{bc}}, \quad (2.31)$$

where \mathbf{S}_j is a symmetric matrix with a high degree of sparsity ($> 99.9\%$ of entries are zero when solving a typical DBS field problem). These properties simplify the calculation of the matrix inverse, which can be computationally expensive due to its dimensions.

2.3.3 Solvers

Different numerical approaches can be utilized to solve Eq. 2.31. Here we highlight only those that were empirically efficient for our particular DBS problem and also available in the employed FEM software (FEniCS). Unless the matrix dimensions are not extremely large, the MULTifrontal Massively Parallel sparse direct Solver (MUMPS) [137] can be applied on powerful machines. Its advantage is robustness when dealing with ill-conditioned systems, e.g. when multiple floating conductors are present, i.e, \mathbf{S} is highly inhomogeneous. The main disadvantage is poor scalability: apart from a drastic increase in computational time, the memory requirements usually exceed the capacity of desktop computers.

If none or a single floating conductor is present, the iterative biconjugate gradient stabilized method (BiCGSTAB) [138] with an algebraic multigrid preconditioner is used. This solver is an extension of the conjugate gradient method for systems with complex numbers, and it provides a significantly higher performance than MUMPS for large FEM systems (see Fig. 2.19). For the quasistatic formulation (Eq. 2.14), with or without floating conductors, the generalized minimal residual solver (GMRES) [139] is employed, which had a more robust convergence for the considered problem than the classic conjugate gradient method. For more information on FEM solvers, please refer to [54]. It should be noted that in our FEM implementation the system for the electroquasistatic formulation (Eq. 2.13) contained twice as many degrees of freedom as the quasistatic model given the same basis function order and the number of elements. These additional degrees of freedom were necessary to account for the imaginary part that was modeled using a second function space. This simple but computationally expensive method was utilized due to the lack of complex numbers support in FEniCS.

2.3.4 Electric potential derivatives

After the coefficients f_j and, following Eq. 2.23, the electric potential $\varphi(\mathbf{r})$ are computed, we can evaluate the electric field $\underline{\mathbf{E}}(\mathbf{r})$ and the current density $\underline{\mathbf{J}}(\mathbf{r})$. As mentioned previously, the former is sometimes used to obtain a rough approximation of the neural activation induced by DBS [12, 119]. The latter can be integrated over the active electrode contacts to estimate the corresponding impedances or currents delivered by a DBS stimulator. The current estimation is naturally essential when this parameter is controlled, which is achieved by regulating the voltage, i.e. the boundary conditions, over the DBS pulse. In modeling, we can utilize the linearity of Eq. 2.13 and simply scale the solution to match the current. For example, if one source with current J_C and the grounding are simulated, we first solve the system for a unit voltage,

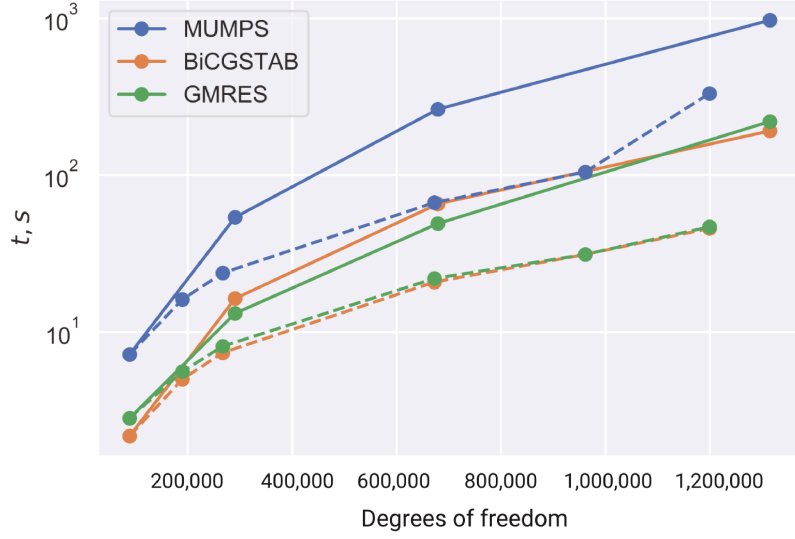


Figure 2.19: Solvers' performance for the quasistatic formulation of Maxwell's equations (Eq. 2.14) depending on the degrees of freedom and refinement type. Solid lines show the results for the p -refinement, dashed for the h -refinement.

compute the corresponding current J_S through the source (or the ground) and scale the electric potential $\varphi(\mathbf{r})$ by J_C/J_S . Note that in FFEM, the scaling is conducted not in the time domain, but at frequencies obtained by a *Fourier transform* of the DBS pulse. For multicontact stimulations, the scaling involves the superposition of fields computed individually for each source-ground pair, while the rest are set to floating conductors; the procedure is described in [140].

To obtain spatial distributions for $\underline{\mathbf{E}}(\mathbf{r})$ and $\underline{\mathbf{J}}(\mathbf{r})$, we have to express them in terms of the electric potential and project to the vector function space, in our case defined with discontinuous Lagrange basis functions, set one order lower than the basis functions for the electric potential: this is a natural space for derivatives of nodal based Lagrange functions [141]. For large systems, projections for the whole domain might be as costly as the solution of Eq. 2.31. They may nevertheless be necessary in order to control the quality of the FEM mesh.

2.3.5 Mesh refinement

Since the true solution is not known, we have to refine the mesh and assess the deviation of the electric potential, which is the quantity of interest when modeling neural response. If the deviation between the original and the refined mesh is large, we have to refine the mesh further until the solution converges with a certain tolerance (the details are provided in Appendix A.1). In the context of neural activation, the convergence is crucial on the compartments of

neurons¹⁵. How should we refine the mesh to achieve the fastest convergence? A simple idea is to refine the whole domain, but this will lead to excessive discretization and thus a significant slowdown. For this reason, the uniformly refined mesh can be used for the validation of the convergence, but never for the actual computations in the frequency spectrum. A flexible h -refinement that keeps the balance between accuracy and efficiency should be based on the local evaluation of the solution or its derivatives. The electric potential $\varphi(\mathbf{r})$ itself is not necessarily a good indicator: in regions distant from the Dirichlet boundary condition and neuron compartments, the deviation may be high, but their refinement is usually unnecessary. On the other hand, Eq. 2.13 contains the gradient term, and empirically I observed that the convergence of the electric field $|\underline{\mathbf{E}}_{\text{el,mid}}|_2$ at the midpoint of FEM elements and the convergence of the element-wise integrated current density J_{el} are efficient criteria for mesh refinement. Both $|\underline{\mathbf{E}}_{\text{el,mid}}|_2$ and J_{el} should lie above certain thresholds to avoid refinement of "non-important" elements. Please refer to Appendix A.1 and [140] for more details.

Alternatively, a p -refinement approach could be employed, i.e. increasing the order of the basis functions. However, in our problem the h -refinement is more pertinent considering the relatively high resolution of MRI/DTI data: the deviation might occur due to a coarse mapping of the dielectric properties onto the mesh.¹⁶ Furthermore, p -refinement in FEniCS is problematic: the application of higher order functions cannot be limited to a particular domain. Nevertheless, we have to take into account that the 2nd order Lagrange polynomials will yield piece-wise linear derivatives, which is why the 3rd order elements are employed for computations that involve the electric field $\underline{\mathbf{E}}(\mathbf{r})$ or the current density $\underline{\mathbf{J}}(\mathbf{r})$. In DBS problems, a finer discretization is usually required at the active electrode contacts, especially on the edges between the Dirichlet and the homogeneous Neumann (insulation) boundary conditions, where high magnitude electric fields occur. Apart from this, the h -refinement of contacts is required to accurately approximate their cylindrical or spherical shapes with tetrahedral elements. Although the FEM theory for curved elements was developed, its availability in open-source software is limited, and its advantage is not absolute due to the required higher order functions.

It should be noted that multiple mesh refinement algorithms of different complexity have been proposed for FEM [142]. In this subsection, I briefly described an algorithm that was implemented in [140] for particular DBS problems, though I do not claim it to be the most efficient and admit that further enhancements are possible.

¹⁵The deviation of 1% between refinement steps is usually acceptable: the event of action potential initiation is binary and thus not extremely sensitive.

¹⁶Such deviations usually arise from a coarse mapping of highly conductive CSF. Therefore, in [140] we implemented an algorithm that evaluates the effect of extremely accurate CSF mapping on the electric potential at neuron compartments.

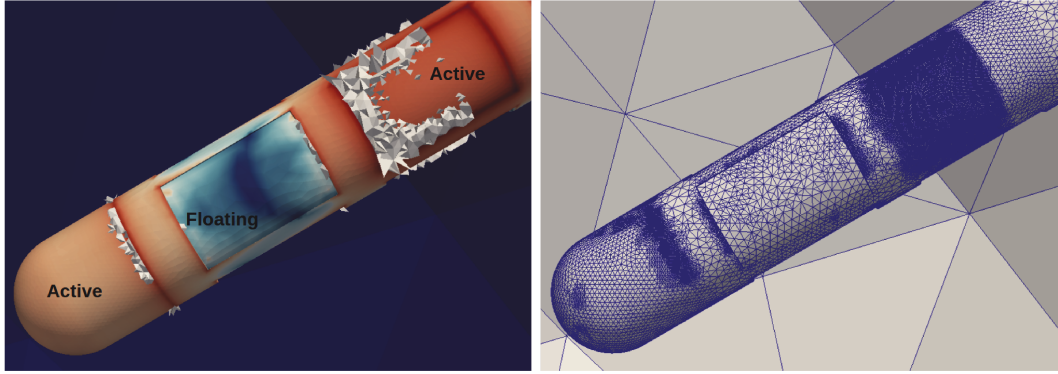


Figure 2.20: An example of mesh refinement based on the electric field convergence. **Left:** the distribution of the electric field magnitude (log scale) on the electrode surface and FEM elements marked for a subsequent refinement. Note the high magnitude at the edges of the active contacts and the low magnitude (blue area) at the floating contact. **Right:** wire view of the meshed surface after all refinement steps are completed. Note the fine discretization at the edges of the contacts and a part of the upper active contact.

2.4 Simulation platform OSS-DBS

The aspects of DBS modeling described in this chapter were incorporated in the automated open-source simulation platform OSS-DBS [140], the functionality of which hinges on a collection of different open-source tools with the workflow governed by Python scripts and the input configured via a graphical user interface (see Fig. 2.21). A simulation starts from CAD modeling and an initial meshing of the computational domain according to

- the provided medical imaging data (atlas-based or patient-specific);
- the selected electrode parameters (electrode model, placement, encapsulation thickness);
- the targeted neural tissue (uniform axon arrays for VTA, fiber tractography for pathway activation or custom allocation of neurons).

The domain is then converted to the volume conductor model with the previously described methods using pre-segmented MRI and DTI data. If necessary, users can specify the properties of the electrode–tissue interface, i.e. the parameters of CPE and the dielectric properties of the encapsulation layer. The volume conductor model is further refined based on the convergence of the electric field and the current, with a stopping criterion defined by the convergence of the electric potential on neuron compartments. These compartments either belong to the abstract straight axons for VTA evaluation or to the realistic models of neurons arranged in space by the user. Additionally, OSS-DBS provides an automated allocation of axons on fiber tracts in the vicinity of the

target to conduct pathway activation modeling. Once the volume conductor model is sufficiently refined to comply with the accuracy requirements, the FFEM problem is solved. The number of computations in the frequency domain is reduced by the octave band approximation (see Fig. 2.5), and to speed up the process further, a parallel processing is implemented. The same applies to a subsequent inverse Fourier transform and the estimation of the neural response to the altered distribution of the extracellular potential. Alternatively, a VTA approximation can be computed using either the electric field or its divergence thresholding as described in [119].

All these steps are conducted in an automated manner to facilitate iterative studies such as treatment optimization, uncertainty quantification or evaluation in patient cohorts. This is the reason why some aspects such as segmentation or tensor scaling that might require manual assessment are not included in OSS-DBS. The platform is distributed with a Docker image [143] that encapsulates the required software environment into a so-called container that allows a quick deployment and support of different operating systems.

To meet the demands of the clinical community, a collaboration with the Lead-DBS project [12] was established. The combined tool offers an advanced processing of patient-specific medical imaging (segmentation, normalization, electrode localization, visualization) and an intuitive front-end together with the comprehensive field and neural modeling provided by OSS-DBS. Apart from clinical research [144], OSS-DBS is employed in fundamental computational studies that also include rodent DBS [51, 61, 145]. The functionality of the platform can be easily extended beyond classic DBS problems, e.g. for transcranial direct current stimulation or coordinated reset DBS.

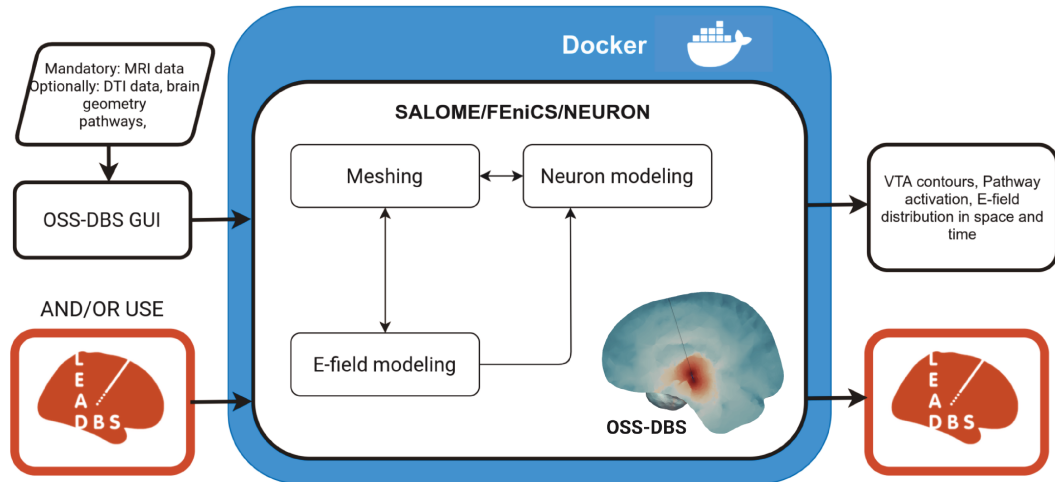


Figure 2.21: *Workflow of OSS-DBS. Input data are provided either directly or after Lead-DBS processing that facilitates patient-specific studies. OSS-DBS computations are encapsulated in a Docker container that can be deployed on all major operating systems.*

2.5 Uncertainty quantification in DBS

As in most biological systems, brain modeling is subjected to various uncertainties, both epistemic (due to avoidable measurement inaccuracies, simplifications, etc.) and aleatoric (due to limited knowledge of complex processes and random effects). In the context of DBS, those are variations in the dielectric properties of brain tissue, as well as uncertainties in neural dynamics, electrode placement, modeling assumptions, etc. To estimate the influence of these factors on the stimulation outcome, methods of uncertainty quantification can be applied. One of them is the polynomial chaos technique [146] that drastically reduces number of solutions of a computationally costly problem, in comparison with Monte Carlo based methods, by approximating it with a surrogate model described with a polynomial expansion.¹⁷ In our problem, it can be used to estimate the DBS-induced neural activation \mathcal{A} :

$$\tilde{\mathcal{A}}(\mathbf{Q}) = \sum_{i=0}^{N_p-1} c_i \xi_i(\mathbf{Q}), \quad (2.32)$$

where $\mathbf{Q} = [Q_1, Q_2, \dots, Q_n]$ are n uncertain parameters, $N_p = \frac{(p+n)!}{p!n!}$ is the number of expansion factors and p is the polynomial order for ξ_i . In [147], it was demonstrated that the expansion coefficients c_i can be efficiently calculated by solving the model for \mathbf{Q} determined by the point collocation method with Hammersley sampling [148]. The total number of required computations is then defined as

$$N_{\text{comp}} = 2(N_p + 1). \quad (2.33)$$

The authors showed that computing the expansion coefficients c_i using the least-squares method on this overdetermined system leads to a significant improvement of convergence. It must be noted that applicability of the polynomial chaos is limited by the number of uncertain parameters considered at once and it becomes inadequate for problems with $n > 20$ in comparison with Monte Carlo based methods [149]. Furthermore, it assumes a smooth dependency of the model output on the uncertain parameters. Nevertheless, for the problems that will be considered in this thesis, both conditions are fulfilled, if not stated otherwise.

The obtained polynomial expansion not only approximates computationally costly problems, but also statistical metrics such as mean and variance:

$$\mathbb{E}[\mathcal{A}] \approx c_0; \quad \mathbb{V}[\mathcal{A}] \approx \sum_{i=1}^{N_p-1} \mathbb{E}[\xi_i^2(\mathbf{Q})] c_i^2, \quad (2.34)$$

¹⁷This description is actually resemblant to the FEM system expressed in terms of basis functions, but those should not be confused. Apart from the different statement of problem, the methods have their own distinct mathematical foundations.

as well as Sobol' indices that reflect the influence of individual uncertain parameters and their interaction on the model output. To obtain percentiles, e.g. P_5 and P_{95} , a Monte Carlo based method can be applied to the surrogate model, which returns nearly instantaneous solutions. A comprehensive description of the polynomial chaos application in DBS modeling is presented in [150].

In this thesis, the generalized version of the technique [151] is employed, which utilizes different types of polynomials $\xi(\mathbf{Q})$ in the expansion, depending on the underlying distributions of uncertain parameters. All analyses are conducted using the open-source Python toolbox UncertainPy [149], which is largely based on the ChaosPy project [152] that offers non-intrusive methods for uncertainty quantification. UncertainPy allows users to conduct such studies sparing details of mathematical implementation, but at the same time granting a freedom in parameter specification for more involved analyses. Furthermore, the tool could be directly integrated with the Python-based OSS-DBS to solve the computational model on the collocation points (see the workflow in Fig. 2.22).

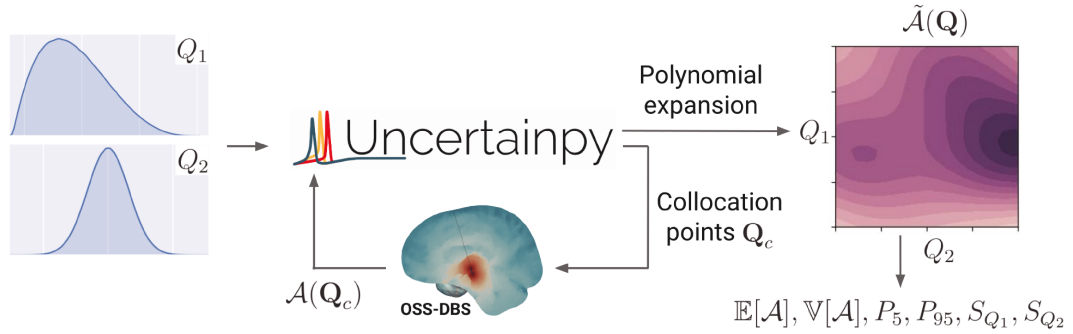


Figure 2.22: Workflow for uncertainty quantification using the generalized polynomial chaos implemented in UncertainPy. For uncertain parameters \mathbf{Q} , the user provides estimated probability density functions for which UncertainPy selects an appropriate polynomial expansion to approximate the neural activation $\tilde{A}(\mathbf{Q})$. Coefficients of the polynomials are computed by solving the original computational model in OSS-DBS for parameters \mathbf{Q}_c defined by the collocation method with Hammersley sampling. Statistical metrics and Sobol' indices S_{Q_1}, S_{Q_2} are either estimated directly from the polynomial expansion or by solving the computationally inexpensive surrogate model using a Monte Carlo sampling.

Chapter 3

Local Modulation of Neural Activity

It was previously mentioned that DBS decouples activity in somas and axons [117], and that the DBS-induced activation of the latter is usually a focus of modeling. However, somatic activity will impact efferents that are not directly activated by DBS. In [153], it was observed that the inhibition further increases the fidelity of axonal response to the DBS signal as its interaction with endogenously generated APs is eliminated. In this chapter, we will numerically investigate the effect of an extracellular field on STN projection neurons and compare it with the extent of VTA. Furthermore, we will discuss the challenges of targeted stimulation in rodent DBS, in particular the precision of the electrode placement and the field focalization problem.

3.1 Direct DBS effect in stimulated nuclei

Without diving into the oscillatory pathology of PD (which will be discussed in more detail in Chapter 4), it can be generally stated that PD is associated with an elevated bursting activity of the STN and GPi in the beta band (13–30 Hz) [7, 154]. STN-DBS was shown to decrease neural activity in the targeted nucleus [22], which can be attributed to the stimulation of GABAergic afferents [155]. However, the cell itself may be inhibited/excited due to alterations of the extracellular field on the cell membrane and dendrites. It was also demonstrated that DBS can decouple activity in the soma and axon [117], and that the inhibition of somatic activity can facilitate the axonal response to DBS [153]. The question is whether this decoupling occurs predominantly due to the activation of GABAergic afferents to the STN cells or whether the effect can be induced directly by a polarization of the membrane. To test the relevance of the latter mechanism in the context of rodent DBS, a model of

the rat STN projection neuron described in [113] was employed. The model can reproduce various electrophysiological states observed in *in vitro* and *in vivo* experiments, including the active behavior of the membrane. The cell dendrites are asymmetric and located in one plane with the maximum lateral extent of $0.372 \mu\text{m}$ (Fig. 3.1, top left). In the volume conductor, the models are distributed in the STN (the geometry of which was extracted from the rat brain atlas [45]) and aligned with the Cartesian planes, with additional flipped models to account for the asymmetry. To couple the cells with a DBS-induced electric field, an extracellular mechanism with default NEURON parameters was added.

The DBS effect on the isolated cells is to be compared with the extent of VTA computed for the same stimulation protocols. The VTA axons are based on the aforementioned McIntyre's model with a fiber diameter of $2 \mu\text{m}$ and a length of 1 mm (15 nodes of Ranvier) with the VTA grid extending over the

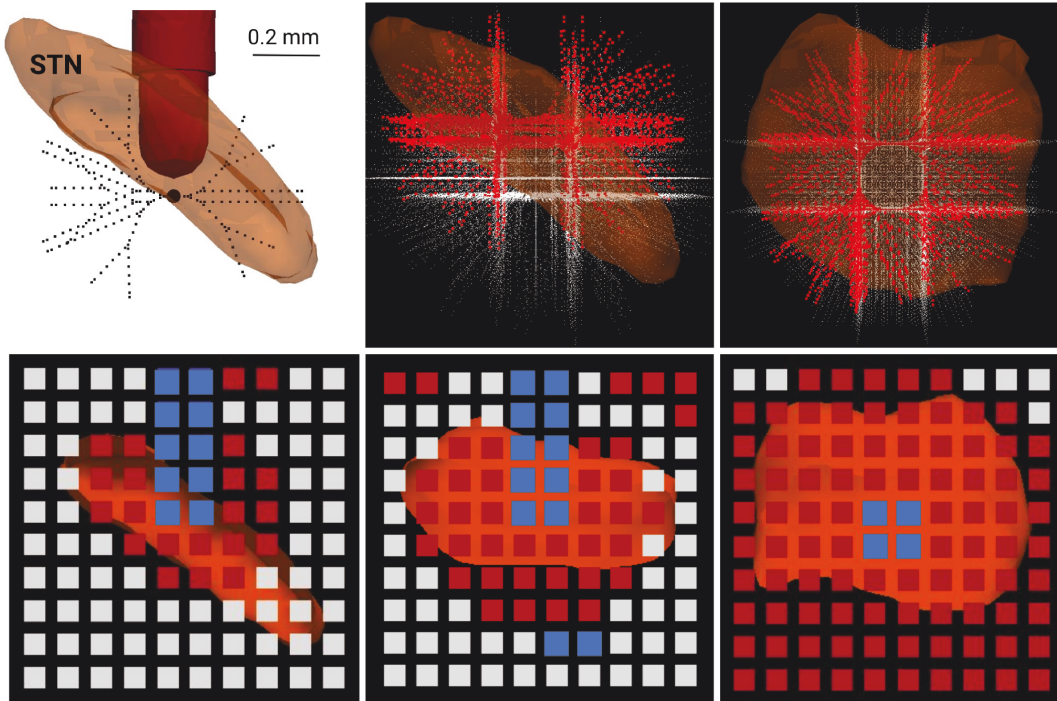


Figure 3.1: Direct local activation induced by rat STN-DBS. **Top left:** the geometry of the STN projection neuron [113] in comparison to the STN (in orange) and the stimulating tip of the bipolar electrode SNEX-100 with a $50 \mu\text{m}$ encapsulation layer (in red). **Top center and right:** only cells marked in red respond with an action potential to five DBS pulses (see Fig. 3.3). **Bottom:** VTA contours in coronal, sagittal and axial planes, respectively. Blue voxels correspond to the axons considered damaged by the implanted electrode. Note the wide extent of activation for axons oriented parallel to the electrode.

STN (Fig. 3.1, bottom row). To capture the influence of axonal directionality, the VTA is computed for each Cartesian axis.

The volume conductor model of the rat brain is constructed based on MRI and HARDI data from [45]. The MRI data are segmented into grey matter, white matter and cerebrospinal fluid (see Fig. 3.2, A); the conductivities and permittivities of the corresponding tissue at different frequencies are estimated using [58] with the omission of the α -dispersion as proposed in [59], and the conductivities are further upscaled as described in Chapter 2. The omission of the α -dispersion justifies the choice of the quasistatic formulation of *Maxwell's equations* (Eq. 2.14) for computing the electric field induced by DBS. Conductivity tensors are assessed from the HARDI data using the Python package Dipy¹⁸ [71] and the volume conservation method [75] described in Chapter 2. The stimulation is conducted via the bipolar rodent DBS electrode SNEX-100 (MicroProbe Inc. MD, USA), with the encapsulation simulated as a 50 μm layer with a conductivity of grey matter decreased by 20% (chronic phase). To ensure the accuracy of the computations, the previously described mesh refinement algorithm is enabled.

To test the excitability of the cell models, the extracellular field is computed for a current-controlled stimulation following a common protocol (rectangular cathodic pulse of 100 μA and 60 μs) and a long-pulse alternative with the

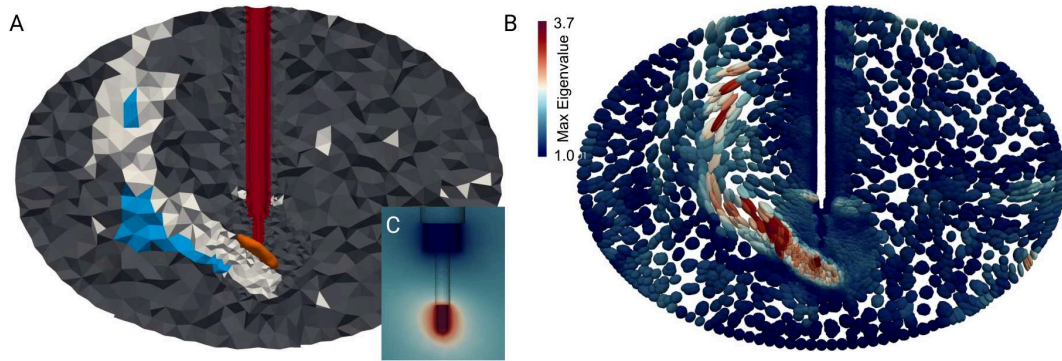


Figure 3.2: Volume conductor model for rat STN-DBS. **A:** the distribution of grey and white matter, depicted with the corresponding colors, as well as CSF (blue) and the encapsulation layer (red). The STN is shown in orange. The electrode is assumed to be highly conductive and removed from the model, preserving the appropriate boundary conditions. The large computational domain is shown here for visualization purposes, but can be significantly truncated for the bipolar stimulation. **B:** the elliptic representation of conductivity tensors obtained based on water diffusion data [45] and scaled using the volume conservation method [75]. **C:** the electric potential distribution in the vicinity of the electrode contacts. Due to the linearity of Eq. 2.14, the solution can be scaled to compute activation for different amplitudes.

¹⁸The HARDI data and Dipy will be used later to extract pathways affected by STN-DBS

same total charge per phase ($25 \mu A$ and $240 \mu s$). The membrane potential of the cells is monitored during a passive phase (see Fig. 3.3), and five consequent DBS signals ($130 Hz$) are applied to test the fidelity of the response, i.e. the AP initiation. The simulation reveals that the models fail to follow each or even every second DBS pulse, and a single AP was elicited only on the cells closest to the electrode (Fig. 3.1, top center and right; 5.66% of all seeded cells for the conventional pulse and 4.63% for the long pulse with a low amplitude). At the same time, VTA contours show the activation over the whole STN along each Cartesian axis.

The inhibition of the STN cells is simulated for the same pulses but with a reversed polarity¹⁹. Again, five DBS signals are simulated, this time to suppress a spike of endogenous activity (see Fig. 3.3). Evidently, the spike is delayed by DBS, but still occurs even within the stimulation interval. Thus, we conclude that the inhibition and activation of STN cells is predominantly induced not directly by the extracellular field, but via the activation of STN afferents. For this reason in the following studies the DBS input to neural circuits will be investigated in the context of axonal activation and its approximations.

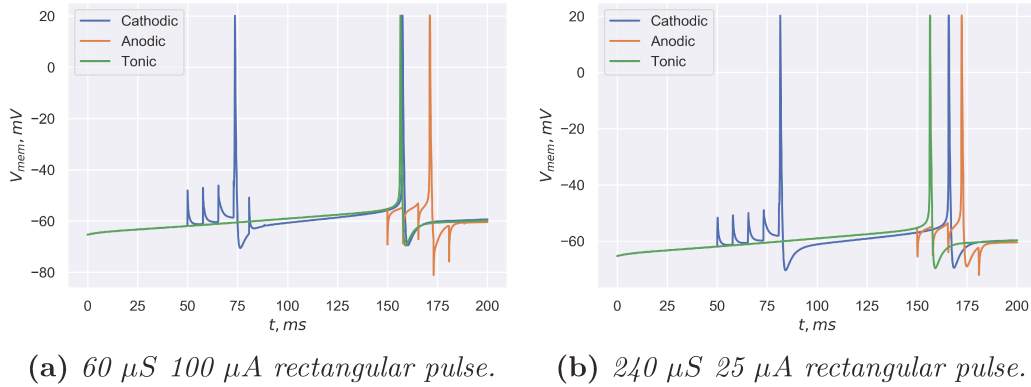


Figure 3.3: Response of an isolated STN projection neuron (without an axon, see Fig. 3.1, top left) to the DBS-induced extracellular field modulation. Note that the anodic stimulation (locally hyperpolarizes the neural membrane) postpones but does not suppress the endogenous firing, while the cathodic stimulation (locally depolarizing) provokes an action potential initiation, but with a low fidelity.

¹⁹Note that anodic stimulation can also excite neurons due to *Kirchhoff's first circuit law*.

3.2 Precision of implantation and VTA

In the previous section, it was shown that VTA extends over the stimulated target for $100 \mu A$ $60 \mu s$ rectangular pulse. This raises concerns whether adjacent structures of the basal ganglia that are involved in the pathology, but not targeted by the stimulation may be affected by DBS. The problem is especially relevant in rodent DBS where the miniature dimensions of brain structures hamper the precise electrode placement. In [61], our model predicted that misplacements within the STN significantly affect VTAs in the entopeduncular (EPN) and especially the substantia nigra pars reticulata (SNr), while the effect of the conductivity and thickness of the encapsulation layer is minor. At the same time, the relatively large dimensions of rodent stimulating electrodes and the consequent neural damage discourage from implantations into the STN. Instead, the electrode can be placed cranially to the target (see Fig. 3.4).

Here, I conduct an uncertainty quantification analysis to estimate the effect of cranial implantation on the VTA extent while accounting for a possible electrode misplacement along the posteroanterior axis, as well as for reported differences in the encapsulation layer properties (see Fig. 3.5 for the assumed probability density functions). The volume conductor model described in the

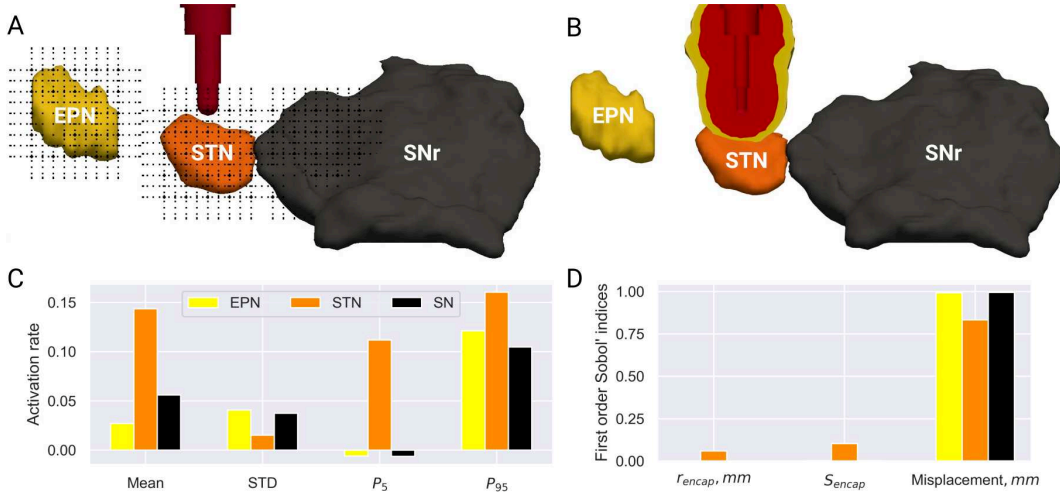


Figure 3.4: Activation in the STN and adjacent EPN and SNr for a cranial implantation (0.4 mm above the STN). **A:** VTA grids over the brain structures. **B:** $|E|_2$ -based VTA approximation ($> 0.323 \text{ V/m}$ in red, $> 0.2 \text{ V/m}$ in yellow). Evidently, most of the activated tissue is outside of the target. **C:** statistical metrics for the VTA arrays (STD – standard deviation, P_5 and P_{95} are the 5th and the 95th percentile, respectively). **D:** the first order Sobol' indices for the VTA arrays. The precision of the electrode implantation is found to be the dominant factor, especially for the non-targeted nuclei.

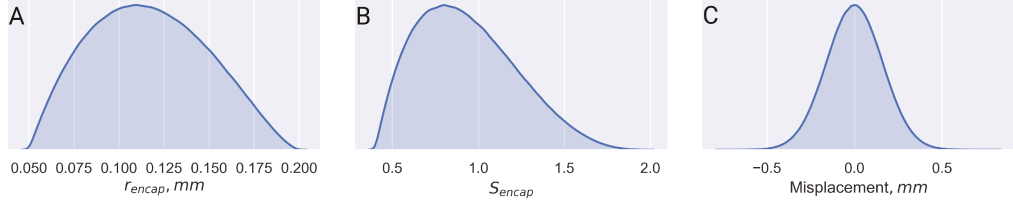


Figure 3.5: Assumed probability density functions for the thickness of the encapsulation layer (A), its conductivity scaling (B), and the deviation from the implantation site along the posteroanterior axis of the rat brain (C).

previous section is employed, which incorporates tissue anisotropy in contrast to [61]. Furthermore, the axon arrays for VTA are configured manually so that the encapsulation thickness does not alter the number of axons, and activation rates (activated/seeded) in the VTAs are reported. As was expected, the cranial implantation significantly reduces the overall and the targeted activation, and the reduction is especially prominent for bipolar electrodes, where the electric field is "pulled" upwards [145] (see Fig. 3.4). This issue will be addressed in the next section. A limited activation still occurs in the adjacent nuclei (Fig. 3.6) with the implantation precision being the paramount factor, as indicated by the first order Sobol' indices, while the STN-VTA is marginally perturbed by the encapsulation layer properties. The marginal effect is explained by the current-controlled stimulation that compensates for the voltage drop over the encapsulation, which still, however, alters the shape of electric fields and thus impacts the activation. A VTA approximation based on $|\mathbf{E}|_2$ yields a comparable estimation of the DBS effect (Fig. 3.4, top right).

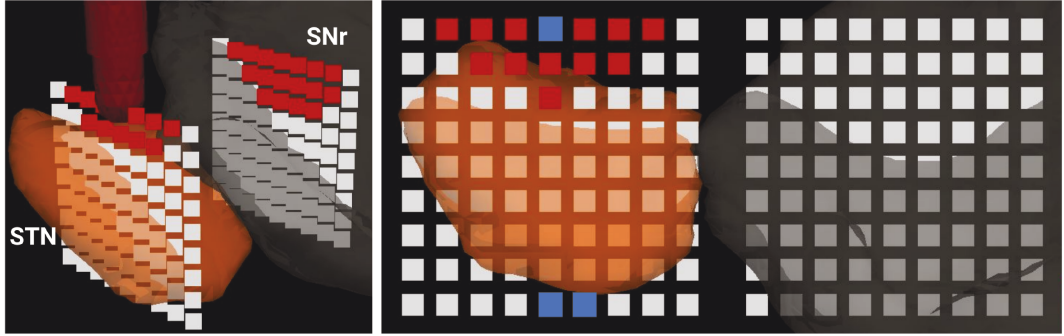


Figure 3.6: VTA contours in coronal (left) and sagittal (right) planes computed for the precise cranial implantation (red – activated axon, blue – excluded due to the intersection with the electrode or CSF). Activation in the SNr occurs due to the membrane polarization on the axons oriented towards the STN.

3.3 Field focalization for cranial implantations

The problem of extensive stimulation above the STN, occurring for cranial implantations, was addressed in [145], where new electrode designs were proposed (see Fig. 3.7, A) and compared to conventional rodent DBS leads. Apart from the tip modification, the main feature of the customized design is a grounding surface on the electrode's shaft located far enough (3 mm) from the core contact to diminish the "pulling" of the electric field. The length of the surface (2 mm in axial direction) was chosen such that the electric field strength was below the 0.323 V/mm threshold²⁰ at the distances larger than $50 \mu\text{m}$, i.e. any activation near the grounding would be confined to the encapsulation layer. In [145], VTAs were approximated with electric field metrics, and in this section I will briefly analyze the differences of VTA contours based on axonal activation. Three electrodes are considered: previously simulated SNEX-100, a custom electrode with the core contact located on the blunt tip and a custom electrode with a spherical rounding. The third custom design, where the core contact is located on a concave surface, showed a marginally higher performance, which is outweighed by its manufacturing complexity.

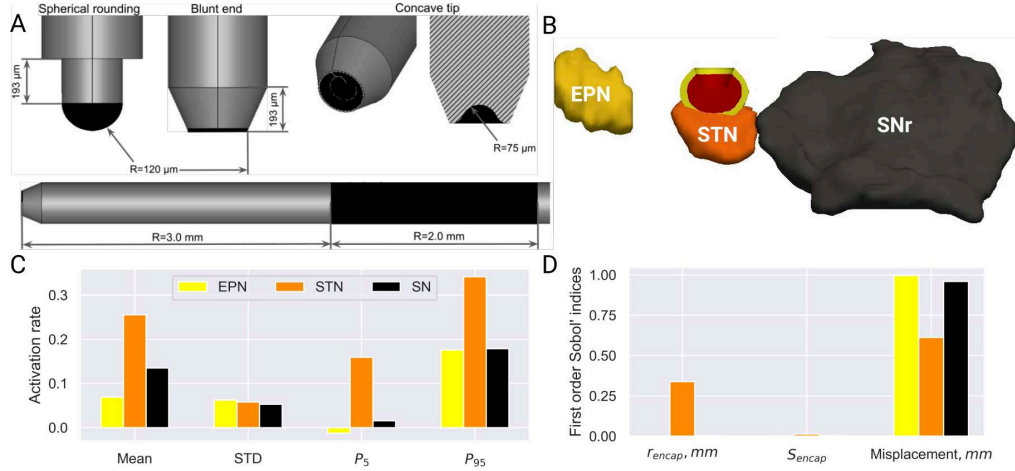


Figure 3.7: Activation in the STN and adjacent EPN and SNr for a cranial implantation of a custom electrode with the blunt tip design. **A:** schematics of the custom electrodes (adapted from [145]). **B:** $|E|_2$ -based VTA approximation ($> 0.323 \text{ V/m}$ in red, $> 0.2 \text{ V/m}$ in yellow). **C:** statistical metrics for the VTA arrays (STD – standard deviation, P_5 and P_{95} are the 5th and the 95th percentile, respectively). Note the higher overall activation than for the SNEX-100 electrode. **D:** the first order Sobol' indices for the VTA arrays. Again, the precision of the electrode implantation is found to be the dominant factor, but in this case the radius of the encapsulation has a prominent effect on the VTA in the STN.

²⁰In [119], this threshold was defined as the median value for activation of axons with $2.5 \mu\text{m}$ fiber diameter.

The computed VTA contours clearly show a better focalization for the customized electrodes (see Fig. 3.8), especially for the blunt core contact where the activation is predicted predominantly in the STN, while the application of the spherical rounding design may lead to additional stimulation in the zona incerta. Coincidentally, the zona incerta is also a DBS target for PD treatment, especially efficient in the suppression of tremor [156]. However, its structural connectivity is distinctly different from the STN, and although simultaneous stimulation of these two nuclei might be beneficial for alleviation of motor symptoms, it might complicate interpretation of results in fundamental research of the DBS mechanism. As expected, the more compact configuration of the bipolar SNEX-100 electrode leads to higher fields at the grounding (outer) contact and thus a possible direct stimulation of the thalamus, which, again, must be avoided to ensure the integrity of the stimulation hypothesis. However, Fig. 3.8 also clearly shows that the custom electrodes cause more brain tissue damage due to the larger tip diameters. These were necessitated by the charge density per phase considerations [95, 157], which impose safety limits on the current amplitude of DBS pulses.

Furthermore, an uncertainty quantification analysis, analogous to the one described in the previous section, is conducted for the blunt tip design (see Fig. 3.7, C and D). While the relative pattern of activation is similar to that of SNEX-100, a generally higher activation is predicted not only for the STN, but also for the adjacent EPN and SNr, which are also located ventrally to the electrode. The misplacement of the electrode remains the main factor of the uncertainty in the VTAs, but the encapsulation thickness was also demonstrated to have a significant influence on the STN-VTA.

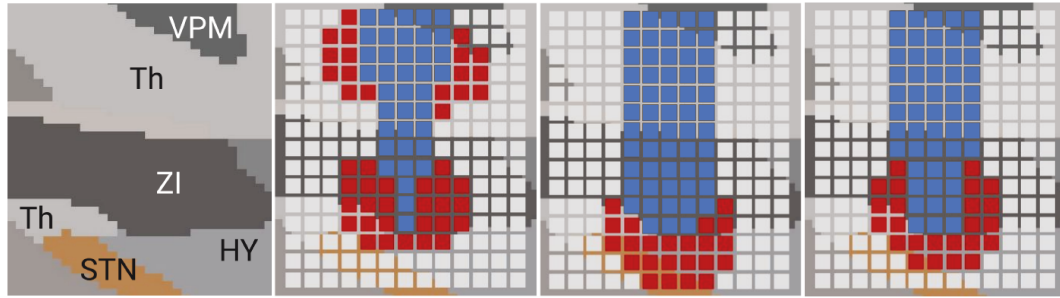


Figure 3.8: *Field focalization for the cranial implantation (coronal view). Left: brain structures above the STN, which are likely to be affected by the implantation (ZI – zona incerta, Th – thalamus, HY – hypothalamus, VPM – ventral posteromedial nucleus). The rest: VTA contours for SNEX-100 and the custom electrodes (blunt tip and spherical rounding), respectively. Note the difference in the extent of tissue affected by the implantation (marked in blue).*

Chapter 4

Pathway Activation Induced by Stimulation of Subthalamic Nucleus

In this chapter, we discuss which pathways are directly affected by deep brain stimulation of the subthalamic nucleus, and how they are involved in alleviation of parkinsonian symptoms. First, I briefly describe the suggested short-term mechanism of DBS in the context of pathway activation. Next, I highlight results obtained in our studies on pathway activation in human STN-DBS. In particular, theoretical optimal pathway activation profiles are presented that were derived based on a retrospective analysis of motor symptom improvement in patients and a network analysis of the DBS-induced modulations via pathway activation. These results are then attempted to be reproduced in a rat STN-DBS model.

4.1 Basal ganglia pathways

The basal ganglia complex is involved in different brain activities such as control of voluntary movements and emotions, as well as cognition and learning. Its input is mainly defined by the neocortex, while the major output is composed of inhibitory projections to the ventral anterior thalamic motor nuclei and the brainstem [158]. Due to a variety of performed activities, the network is often subdivided into associative, limbic and motor systems defined by the corresponding cortical regions. This thesis is focused on motor aspects of Parkinson's disease, and therefore the connectivity of the basal ganglia will be further discussed in this context.

Fig. 4.1 depicts three main pathways descending from the motor related cortical areas to the basal ganglia. These are

- the hyperdirect pathway that provides excitatory input directly to the STN, inducing a short latency inhibition of the ventral anterior (VA) thalamus via the GPi/SNr;
- the direct pathway that inhibits the GPi/SNr via inhibitory afferents from the striatum, leading to an intermediate release of the VA-thalamus;
- the indirect pathway that again reduces VA-thalamic activity by releasing the GPi/SNr due to inhibition of the GPe via striatal afferents.

The basal ganglia nuclei are also under dopaminergic control of the substantia nigra pars compacta, and a neurological damage in this structure, observed in PD, leads to manifestation of motor symptoms. In particular, patients have problems with movement initiation that can be related to the lack of internal motivation controlled by dopamine levels. Conversely, treatment with the dopamine precursor levodopa might lead to hyperkinetic movements, e.g. dyskinesias. Imbalance of the dopaminergic control leads to a hyperactivity in the indirect and the hyperdirect pathways, boosting the activity of the STN, and, in turn, of the basal ganglia output nuclei. For instance, a high neural bursting is observed in the GPi, resulting in an increased inhibition of the VA-thalamic motor neurons. In response to the prolonged inhibition, these neurons exhibit bursting rebounding behavior²¹ that was shown to correlate with muscle responses [9] and aggravation of akinesia. Furthermore, an increased synchronization and a β -band (13–30 Hz) oscillatory activity in the STN and the pallidum was reported, with alleviation of motor symptoms correlating with a suppression of this activity [159, 160, 161].

Based on these and other data, different pathophysiological models of PD were proposed. Principally, they can be divided into firing rate and firing pattern models. The former focuses on changes in the mean activity of the basal ganglia nuclei and a subsequent overinhibition of the VA-thalamic motor neurons. The firing pattern model states that motor symptoms occur due to a jamming of the information flow by increased β -band activity²². Recently, another model was proposed that emphasizes the temporal and spatial separation of the functional and structural connectivity in the basal ganglia pathways [1] (see Fig. 4.1). The model suggests that the network creates a time window for a thalamic release by a local inhibition of GPi neurons via the direct pathway, preceded and succeeded by phases of the overall high activity in the GPi due to the hyperdirect and the indirect pathways. In the PD state, this time window of release is compromised by the reduced inhibition of the GPi due to the

²¹The behavior is manifested in a fast firing after cessation of inhibition, also see Fig. 4.11.

²²However, the causality was challenged in a study that reported a lack of correlated activity preceding manifestation of motor symptoms [162].

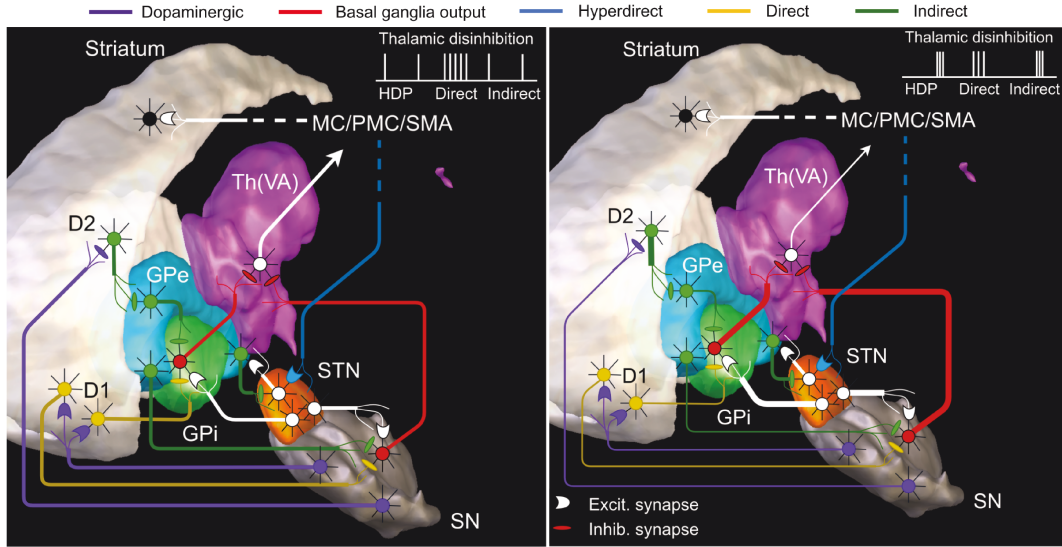


Figure 4.1: Circuit diagram of the basal ganglia pathways in the normal (left) and the parkinsonian (right) states. Line weights reflect the activity levels of the pathways. The parkinsonian state is characterized by a loss of dopaminergic cells in the substantia nigra (SN) that produces an imbalance in the striatum. In turn, it leads to a bursting activity in the basal ganglia output, which can induce rebounding in the ventral anterior nuclei of the thalamus (VA). STN – subthalamic nucleus, GPi and GPe – internal and external regions of the globus pallidus, respectively, MC and PMC are the motor and premotor cortical regions, SMA – supplementary motor area, D1/D2 – dopamine receptors. Note that in the human brain, the pallidosubthalamic pathway consists of two tracts: ansa lenticularis and lenticular fasciculus.

imbalance of the dopaminergic control of the pathways. Nevertheless, these models do not fully explain paradoxes of surgical efficacy in both hypo- and hyperkinetic disorders²³ and do not completely address data reported in neurophysiological recordings (though one cannot discard the factor of experimental flaws).

It is also important to mention pathways that do not belong to the basal ganglia, but can be stimulated by STN-DBS and lead to prominent motor effects (see Fig. 4.2). It is well known that spread of current to the corticofugal pathway, which passes through the internal capsule, might induce motor contractions and dysarthria [163, 164]. Furthermore, one study provided evidence of its involvement in increased akinesia and bradykinesia [165]. In contrast, stimulation of the cerebellothalamic pathway, which passes in the vicinity of the STN, has been shown to alleviate tremors [25, 166, 167]. Other possibly recruited pathways are the medial lemniscus and projections of the pedunculopontine nucleus to the STN and the pallidum.

²³For example, contrary to the expectations, lesioning of GPi does not produce dyskinesias in healthy animals.

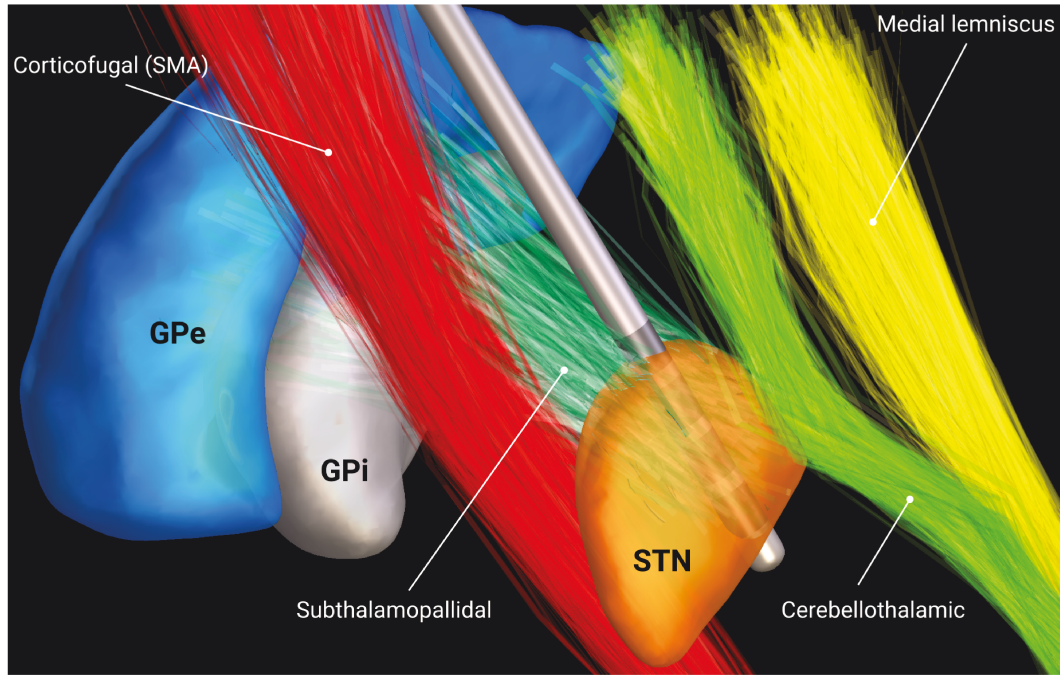


Figure 4.2: *Some passing and local projections potentially affected by STN-DBS. The pathways are taken from [123] and visualized in Lead-DBS. The chosen electrode placement (inside the motor aspect of the STN) is efficient for motor symptom alleviation in Parkinson's disease. Note that the electrode passes through the subthalamopallidal pathways, potentially leading to a significant neurological damage or neuron migration.*

With the network PD pathology described and bearing in mind the high excitability of axonal fibers, it is of interest to investigate possible mechanisms of DBS in the context of pathway activation. In this thesis, the basal ganglia pathway atlas by Petersen et al [123] was employed when modeling STN-DBS in a human brain. This atlas was developed in a collaboration with expert anatomists using holographic visualization of histological and structural MRI data. The atlas contains far less false positive trajectories in comparison with a water diffusion based fiber tractography, where they are often generated due to a low signal-to-noise ratio. On the other hand, the atlas is not accounting for patient-specific and disease related changes in the structural connectivity. For the rat DBS modeling, the pathways had to be classified from fiber tracts that were reconstructed based on the diffusion data; the procedure is described in detail later in this chapter.

4.2 Direct correlation of pathway activation with motor improvement

This section closely follows our study presented in [144]. There, we investigated correlations of DBS-induced pathway activation rates with alleviation of motor symptoms that was defined by the motor section of the Unified Parkinson’s Disease Rating Scale (UPDRS-III). The rates were computed for retrospectively recruited cohorts of bilateral STN-DBS patients from two independent clinical centers. The training and the test cohorts contained 30 datapoints (15 patients, two DBS protocols) and 19 datapoints (19 patients, one DBS protocol), respectively. Pathway activation modeling was conducted in the patient-specific space defined by preoperative MRI T1-weighted imaging in order to avoid non-linear distortion of the electrode geometries that is inevitable when computing in an abstract atlas space. To facilitate modeling in the patient-specific space, the OSS-DBS platform was integrated into Lead-DBS [12], which provides various routines for medical image processing. Electrode localizations based on co-registered postoperative CT scans were conducted and analyzed to exclude patients with a distinctly different lead placement, e.g. penetrating the pallidum. Segmentations of the patient-specific brain tissue distribution were obtained using probabilistic mapping [168] applied to the T1-weighted MRI data and a multispectral MNI (Montreal Neurological Institute) template. Apart from the heterogeneous conductivity, the volume conductor models incorporated tissue anisotropy using a human brain diffusion atlas [67], normalized following the volume conservation method [75]. Since the diffusion atlas and the basal ganglia pathway atlas are defined in MNI space, they had to be co-registered to the T1 modality. Visual assessment showed that the fractional anisotropy and the trajectories of the transformed pathways followed the distribution of white matter in the T1-weighted imaging, while the axon allocation algorithm revealed that intersections of the transformed trajectories with CSF voxels were extremely rare, additionally verifying the accuracy of the co-registration.

Electric field and action potential modeling were conducted analogously to VTA computations described in the previous chapter. However, in this case axons were realistically allocated on white matter fibers instead of artificial uniform grids. The allocation algorithm determined the closest position on the trajectories to active contacts on the DBS electrode. This position was either used as a starting seeding point for pathway projecting to/from the STN or as a middle seeding point for passing fibers. As before, McIntyre’s axon model was used, and the fiber diameter was set to $5.7\ \mu m$, except for the short sub-thalamopallidal and reciprocal projections, where it was set to $3.0\ \mu m$. Since the volume conductor models were constructed based on the patient-specific data, the FEM mesh quality had to be estimated in each simulation. However,

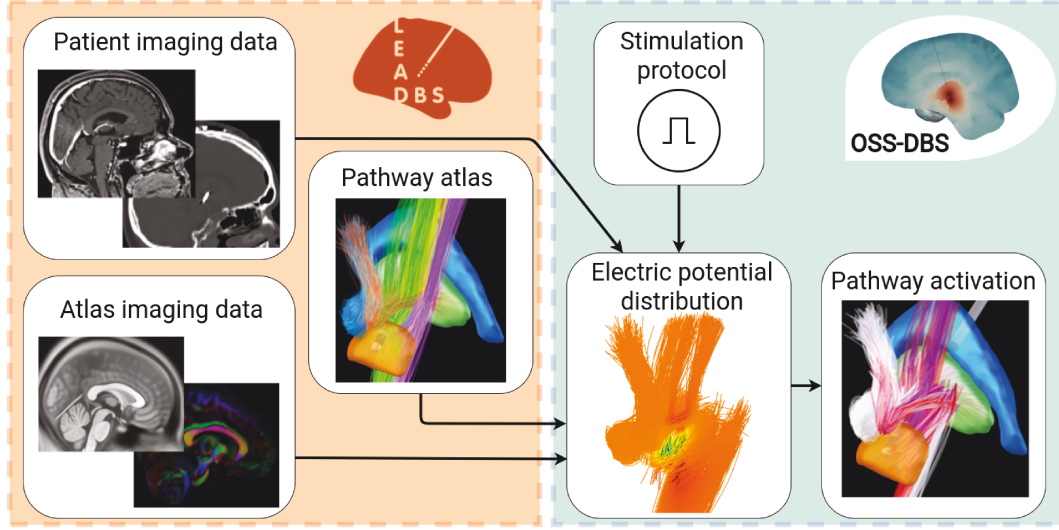


Figure 4.3: Dataflow for pathway activation modeling in the patient-specific space. Based on patient imaging and brain atlases, Lead-DBS (orange box) reconstructs the electrode position and provides a description of tissue and water diffusion distributions in the brain. These data are used by OSS-DBS (green box) to create an accurate patient-specific volume conductor model. The model is then employed to compute the electric potential distribution in space and time along axon models allocated on the trajectories described by a pathway atlas. Finally, for the given distribution, the cable equation is solved to probe the axonal activation, i.e. the occurrence of an action potential in response to DBS. The image is taken from [144].

application of the aforementioned mesh refinement algorithm implemented in OSS-DBS (see 2.3.5) is computationally expensive for 98 stimulation protocols (DBS in each hemisphere was modeled separately). Therefore, a simpler routine was implemented that controlled the total (grounded) current convergence by refining mesh cells with large current densities, predominantly at the Dirichlet boundary condition. For five randomly chosen stimulation protocols, activation rates computed using this refinement method were compared to those obtained on a mesh refined by the original algorithm. For all cases, the deviation of activation rates was below 5%, which is acceptable taking into consideration errors accumulated from the image processing, pathway atlas transformation, uncertainties in the dielectric tissue properties, etc. For more detail on modeling, please refer to Appendix A.2 and [144].

The computed activation rates for the training cohort (see Fig. 4.4) were then analyzed using different approaches. First, a correlation of UPDRS-III improvement with activation in individual pathways was investigated. The only statistically significant positive correlation was observed for the activation in a branch of the hyperdirect pathway descending from the face-neck region of the primary motor cortex. This finding, however, was not corroborated in the test cohort. For other pathways, activation rates were not correlated with motor

symptom alleviation neither when differentiating between the branches (e.g. ansa lenticularis and lenticular fasciculus) nor when aggregating the pathways (e.g. pallidothalamic projection).

Based on these results, it can be theorized that DBS outcome for PD motor symptoms is not determined by activation in individual pathways. Instead, a stimulation pattern defined on multiple pathways should be considered. This is in agreement with the previously described beneficial and detrimental stimulation effects of adjacent tracts, e.g. the hyperdirect and the corticofugal pathway [163, 169, 170]. Initially, it was attempted to cluster the datapoints according to their activation rate profiles defined on the pathways ($\mathcal{A} = [\mathcal{A}_1, \mathcal{A}_2, \dots, \mathcal{A}_k]$), but the result did not correlate with motor improvement. Therefore, another strategy was pursued that utilized improvement vectors derived from two DBS protocols evaluated in the training cohort for each patient. The principle is illustrated in Fig. 4.5. Based on the difference of their UPDRS-III scores as well as activation rates, a theoretical 100% improvement (target) profile was constructed:

$$\mathcal{A}_{\text{target}} = \mathcal{A}_+ + \frac{(\mathcal{A}_+ - \mathcal{A}_-)\text{UPDRS}_+}{\text{UPDRS}_- - \text{UPDRS}_+}, \quad (4.1)$$

where subscripts "+" and "-" refer to the more and less effective stimulation protocols, respectively. To construct $\mathcal{A}_{\text{target}}$, different sets of patients can be employed. For example, the profile can be computed as an average of $\mathcal{A}_{\text{target}}$ for the whole training cohort. Alternatively, only datapoints of patients with the

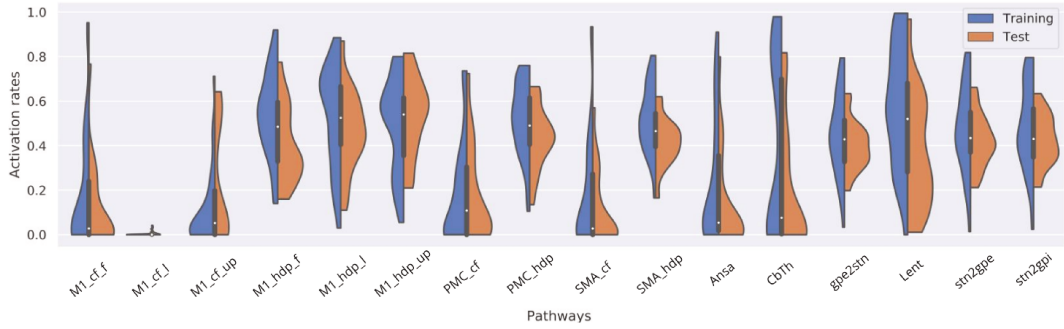


Figure 4.4: Violin plots of pathway activation rates across both cohorts. *M1 and PMC refer to the primary and premotor cortical regions, SMA – supplementary motor area; cf and hdp are the corticofugal and the hyperdirect pathways, respectively; Ansa – ansa lenticularis, Lent – lenticular fasciculus, CbTh – cerebellothalamic pathway; l, f, up - lower extremity, face-neck region, and upper extremity in the primary motor cortex. The cohorts' datapoints provide a wide coverage of the pathway activation space. Noteworthy is the nearly zero activation across both cohorts in the corticofugal branch descending from the region of the lower extremity in the primary motor cortex. The image is adapted from [144].*

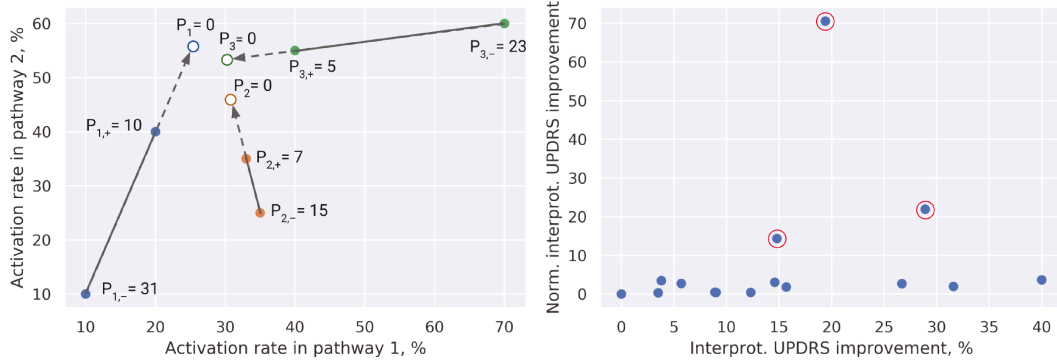


Figure 4.5: *Left:* an example of a target profile derivation from two DBS protocols in a 2-D pathway activation space. Values of P_i denote the corresponding UPDRS-III scores for patient i , "+" and "-" subscripts refer to the more and less effective stimulation protocols, respectively. Note that in our problem the pathway activation space had 16 dimensions. *Right:* the inpatient interprotocol UPDRS-III improvement in the training cohort with and without the normalization by the mean of activation rate differences. The highlighted datapoints were used to derive $\mathcal{A}_{\text{target}}$.

highest interprotocol UPDRS-III improvement might be used. In this study, it was assumed that the activation profile leading to 100% UPDRS-III improvement can be defined with patients who had a higher improvement achieved with a lower interprotocol change of activation rates. Following this criterion, the target profile was constructed based on datapoints of three patients that had a significantly higher normalized²⁴ interprotocol UPDRS-III improvement (see Fig. 4.5, right).

Next, we analyzed a correlation between UPDRS-III improvement (from baseline, DBS-off, off medication) and a "distance" of datapoints to the target profile in the pathway activation space. When comparing different metrics, such as Euclidean distance or Bray-Curtis dissimilarity, the best performance was achieved with the Canberra distance [171]:

$$d(\mathcal{A}_{\text{target}}, \mathcal{A}_a) = \sum_{i=1}^{16} w_i \frac{|\mathcal{A}_{\text{target},i} - \mathcal{A}_{a,i}|}{|\mathcal{A}_{\text{target},i}| + |\mathcal{A}_{a,i}|}, \quad (4.2)$$

where w_i is the weighting factor for the i -th pathway, whose default value is 1.0. The computed distances were negatively correlated with alleviation of motor symptoms ($r = -0.61$, $p < 0.0025$). Moreover, it can be expected that matching activation rates of the target profile is more crucial for some pathways than others. To test this hypothesis, the weighting factors of the Can-

²⁴Empirically, it was observed that for the given training cohort normalization of the UPDRS-III score difference by the mean of activation rate differences yielded the most predictive profile.

berra distance were optimized in order to increase the correlation for the datapoints of the training cohort. Fig. 4.6 shows five pathways that were assigned the highest weighting factors, i.e. their activation was the most significant in predicting stimulation outcomes. A positive correlation with motor symptom improvement was discovered for a moderate activation in two branches of the hyperdirect pathway (descending from face-neck and upper extremity regions of the primary motor cortex) and the pallidothalamic pathways (the ansa lenticularis and lenticular fasciculus), while stimulation of the corticofugal neurons descending from the supplementary motor area (SMA) had a detrimental effect. Naturally, the correlation of the optimized weighted distances and the UPDRS-III improvement in the training cohort was statistically significant (see Fig. 4.7, left), and, in order to validate the correlation model, it was applied to the datapoints of the test cohort. The analysis revealed that their weighted Canberra distances to the target profile (constructed using the training cohort) were significantly negatively correlated with the corresponding UPDRS-III improvement (see Fig. 4.7, right).

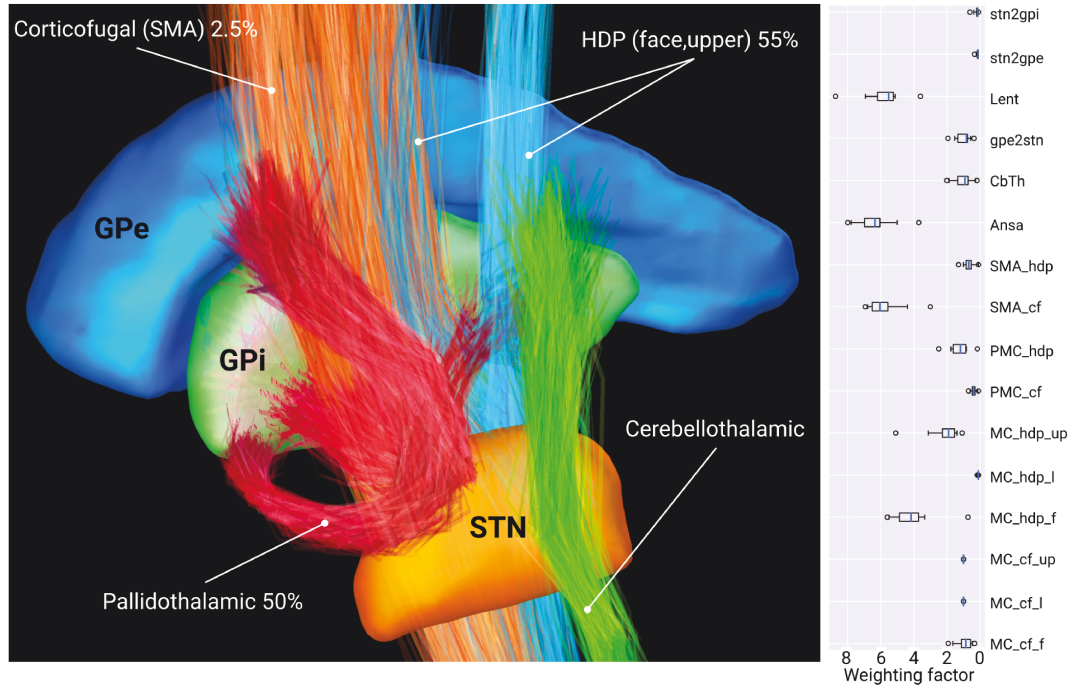


Figure 4.6: Key pathways in the target profile, which activation rates were decisive for UPDRS-III improvement. The box plot on the right shows the optimized weighting factors of the Canberra distance computed with the 'leave-one-out' approach in the training cohort. Note the low number of outliers. The contribution of the cerebellothalamic pathway was not significant in the target profile, but its activation correlated with interprotocol UPDRS-III improvement. The image is adapted from [144].

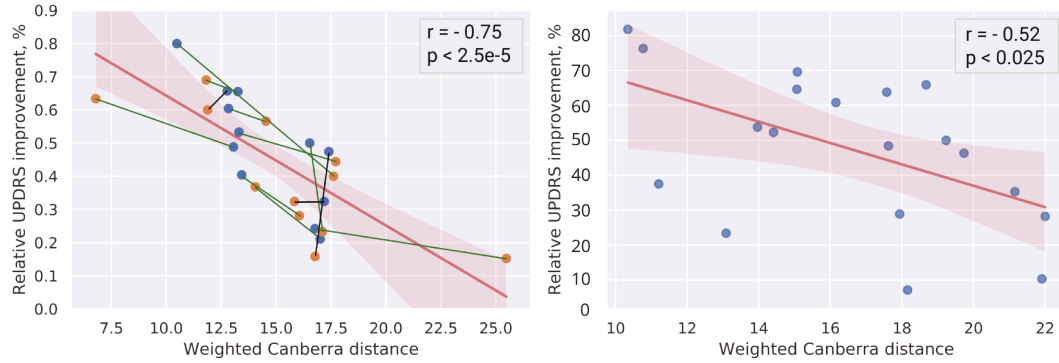


Figure 4.7: Correlation of UPDRS-III improvement in the training (left) and the test (right) cohorts with the weighted Canberra distance (defined in the pathway activation space) to the target profile derived based on three patients with the highest normalized interprotocol UPDRS-III improvement. Colored lines between the data-points highlight the interprotocol binary correlation in the training cohort (green – valid prediction, black – false). The image is adapted from [144].

In agreement with previous studies on STN-DBS [163, 172, 173], it was shown that stimulation of the hyperdirect and the corticofugal pathway leads to beneficial and detrimental effects, respectively. One prominent hypothesis on the HDP-DBS mechanism is an antidromic invasion of the motor cortical regions with a subsequent disruption of the pathological abnormal synchronization [169]. At the same time, alleviation might also arise from a DBS-induced overwriting of the high β -activity, propagating through the hyperdirect pathway and evolving into low β -oscillations [6], which are associated with generation of motor symptoms in PD [174]. A spread of the stimulation to the corticofugal pathway is not only known to evoke motor contractions [163], but is also associated with increased akinesia and bradykinesia for subthreshold levels [165]. Less characterized is the link between motor improvement in PD and the pallidothalamic pathway, though its lesioning was associated with tremor improvement [175]. The results of the present study show that these pathways, which represent a major output of the basal ganglia complex, might be a potential DBS target. The efficacy of their stimulation could also explain a comparable efficiency of GPi- and STN-DBS. The therapeutic effect might arise from a modulation of activity in the VA-thalamic motor neurons that exhibit a presumably pathological bursting in the PD state [9]. In theory, DBS would entrain the inhibitory pallidothalamic neurons to its high-frequency repetition rate, though a complete quenching of firing in the receiving VA neurons is unlikely due to synaptic failures and neurotransmitter depletion. In fact, it was observed that efficient DBS protocols lead to a transformation of the bursting activity to high-frequency oscillations in the thalamus [176], suggesting a beneficial role of a DBS-induced pacing.

Another important finding is the practical applicability of the suggested target profile. For that, a quick optimization of the electrode placement (in MNI space) and the current protocol was conducted with the aim to minimize the weighted Canberra distance. Even after a few optimization steps, a close match of activation profile was observed (see Fig. 4.8). This finding might be important not only for surgery planning, but also when adjusting stimulation protocols for poorly placed electrodes, especially if they support current steering.

Regarding other pathways, it is worthy to note an absence of correlation between UPDRS-III score and activation in the reciprocal subthalamopallidal projections. Undoubtedly, modulation of their activity affects the functional state of the basal ganglia, and it was shown that DBS reduces firing rate of STN neurons via stimulation of GABAergic pallidal afferents [155]. However, pathway activation modeling might not be an appropriate tool for estimating stimulation effects in these projections with a fast endogenous firing. Their excitatory-inhibitory reciprocal communication is a probable source of oscillatory activity [1], and an accurate description of the DBS-induced firing might require explicit modeling of neural dynamics, including refractory

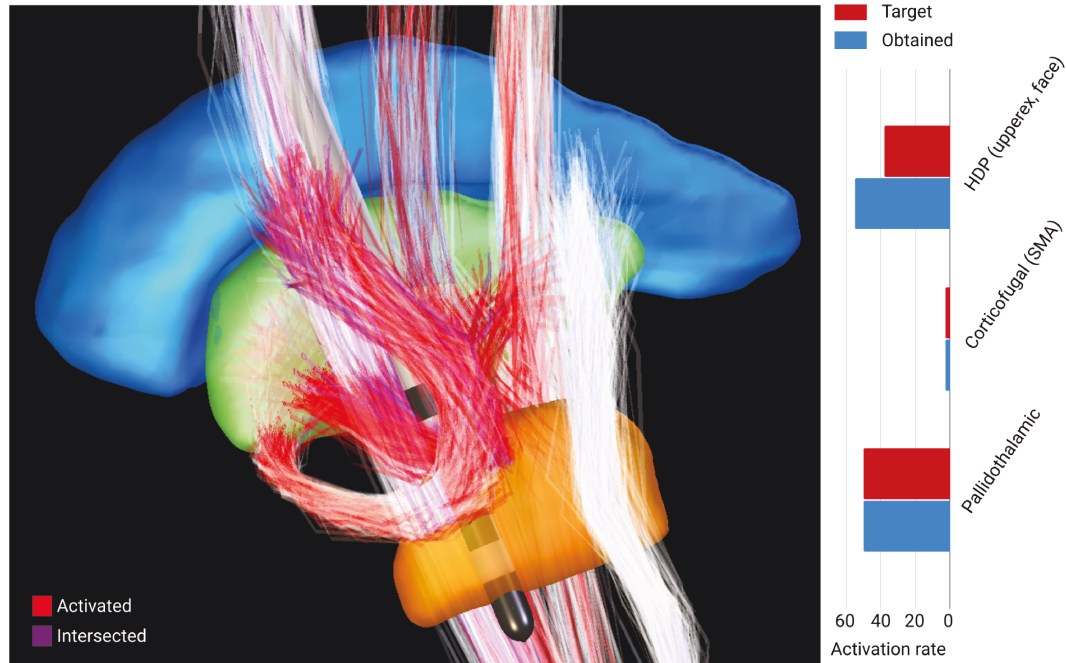


Figure 4.8: An example of electrode placement in the STN (MNI space) with a low weighted Canberra distance to the target profile (defined in the pathway activation space). A half of the lenticular fasciculus was considered "damaged" by the implantation (intersected with the electrode or the 0.1 mm encapsulation layer around it), while the rest were recruited by the DBS. Note that no activation was computed for the cerebellothalamic pathway.

periods, spike threshold adaptation, short-term synaptic plasticity, etc. Furthermore, this circuit of local projections that pass in the vicinity of STN electrodes is likely to be partially damaged or/and displaced during implantation and subsequent microglial reaction (see Fig. 4.2).

At last, an additional symptom-specific analysis was conducted in the study. It was previously reported that tremor alleviation is associated with stimulation of the cerebellothalamic pathway [25, 166, 167], and therefore a correlation between its activation rates and the tremor items of the UPDRS-III score was investigated. Indeed, it was observed that an increase in activation between two DBS protocols correlated with improvement of tremor in the training cohort (see Fig. 4.9). Curiously, there was no correlation for improvement from baseline. Apart from possible contribution of other pathways in tremor alleviation [177], a trivial reason could be ineligibility of the analyzed cohorts that were not formed based on specific symptoms and contained a large number of patients with low tremor scores at baseline. Nevertheless, the results of the interprotocol analysis suggests a beneficial role of the cerebellothalamic pathway in tremor suppression.

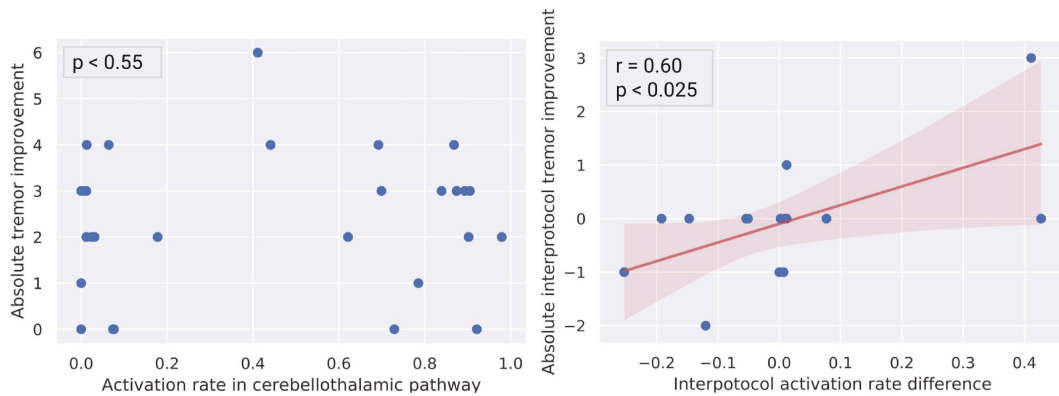


Figure 4.9: *Effect of activation in the cerebellothalamic pathway on tremor alleviation in the training cohort. **Left:** no correlation was observed between activation rates and tremor improvement from baseline. **Right:** the interprotocol difference in activation rates correlated with the corresponding difference in the tremor scores. The image is taken from [144].*

4.3 Network effects of the pathway activation

This section briefly summarizes results of a joint research with Konstantinos Spiliotis, the manuscript is in preparation. In contrast to the previous study, theoretical target activation rates here were not derived using clinical score data, but based on certain biomarkers deemed predictive for alleviation of PD symptoms. For tremor, rigidity and bradykinesia, improvement occurs

within an hour of a continuous stimulation, and the effect wears off in the same period of time upon cessation [178]. Therefore, we focused on short-term DBS-induced network effects and left out a discussion on possible mechanism of neurogenesis and structural reorganization.

During STN-DBS, activation of predominantly GABAergic afferents leads to an increased mean inhibition of STN neurons [155]. Thus, the stimulation was initially considered to be a functional alternative to lesioning. Later, it was shown that DBS recruits in parallel multiple pathways including the excitatory projections to the GPi and GPe, resulting in a mean increase in their firing rates [21]. Moreover, stimulation also alters the firing pattern, reducing presumably pathological β -bursting in the basal ganglia. It was demonstrated that STN regions with an elevated β -activity are efficacious targets for a high-frequency stimulation²⁵, and several studies on adaptive DBS were designed to suppress these oscillations [154, 179, 180]. The excessive β -synchronization might occur due to a dopamine-imbalanced reciprocal excitatory-inhibitory connection of the STN and GPe [1], but a recent study suggested that the pathological activity might be "injected" via the hyperdirect pathway [6]. Stimulation of its fibers was shown to be beneficial in various studies [172, 173], including this thesis, and the mechanism of desynchronization might not be limited to "informational lesioning"²⁶ by DBS, but also include antidromic invasion of cortical neurons [120, 181, 182].

Another potential biomarker is the γ -synchronization (30–100 Hz), which was shown to be positively correlated with alleviation of PD motor symptoms [183] and was theorized to be a "binding band" between spatially distributed brain areas [184]. It is important to note that firing in the major basal ganglia output, the pallidothalamic pathway, is not only modulated by network effects of STN-DBS, but also directly by the stimulation. In the VA-thalamus, effective DBS protocols reduce the previously described bursting rebounds [165], which could be employed as a biomarker for adaptive stimulation. In [9], it was demonstrated that suppression of these bursts by photoinhibition of GABAergic pallidothalamic synapses led to motor improvement in PD mice models. Furthermore, DBS generally reduces the mean activity in the VA-thalamus (in comparison to PD state) and shifts it to higher frequencies, in particular the γ -band, possibly restoring the information flow. As was previously mentioned, it is unlikely that DBS continuously suppresses thalamic motor neurons, but rather paces them by regular single spiking that occurs due to synaptic failures and short-term synaptic depression (STD) [185].

To study DBS effects on these biomarkers, a basal ganglia-thalamo-cortical network of the human brain was developed. The network was built upon the

²⁵Curiously, β -frequency stimulation further worsens PD motor symptoms.

²⁶In this case, "informational lesioning" suppresses low-frequency activity due to neurotransmitter depletion induced by a high-frequency stimulation.

model presented in [186], with the basal ganglia consisting of both segments of the pallidum and the STN. Healthy and pathological striatal activity, arising from degeneration of the substantia nigra pars compacta, was modeled implicitly with current modulations on the GABAergic pallidal inputs. Note that the substantia nigra pars reticulata was not included in the network with the assumption of its functional similarity to the GPi. The thalamus was represented by the ventral anterior nuclei, the recipients of the pallidal efferents. Since the cerebellum was not added to the network, its output thalamic structures were also omitted. Taking into account that involvement of the cerebellothalamic pathway in tremor alleviation was previously reported in the literature [25, 166, 167], including this thesis, the DBS network effects in relation to the symptom were not investigated. Furthermore, later it will be shown that DBS recruitment of the cerebellothalamic pathway is unlikely during rat STN-DBS.

In contrast to [186], the structural connectivity between (and within) brain structures was modeled based on pathway reconstructions. In particular, the previously employed basal ganglia pathway atlas [123] was used to describe the subthalamopallidal, pallidothalamic and corticosubthalamic connectivity. The VA-thalamocortical projections were reconstructed based on a structural group connectome [11, 187]. This anatomically plausible definition of connectivity in the network has also the advantage of explicit coupling with volume conductor models, i.e. the effect of the DBS-induced pathway activation can be propagated in the network and, conversely, the feasibility of an abstract optimal network input can be evaluated with a field modeling. The intranuclear connectivity for pallidal, thalamic and cortical neurons was arranged according to the small-world topology [188], with the proximity defined based on termination points of individual streamlines in the pathways. For the STN, a sparse connectivity was applied [189, 190].

Dynamics of the network were set according to data presented in various studies that conducted neurophysiological recordings in healthy and PD animal models as well as patients [7, 191, 192, 193, 194]. While the main aspects of the basal ganglia dynamics were adapted from [186], some crucial adjustments and enhancements had to be implemented. First of all, the primary motor and premotor cortex, designated together as M1, were explicitly simulated with the resting state dynamics (see Fig. 4.10) that were chosen due to the fact that an increase in β -activity is more prominent before than during voluntary movements [195]. Furthermore, a possible antidromic invasion of M1 via the hyperdirect pathway was considered, with an assumption of comprised fidelity for high-frequency stimulation [196]. Another important addition to the network dynamics was a VA-thalamic rebounding in response to a bursting inhibition via the pallidothalamic pathway [197] (see Fig. 4.11). Additionally, various minor modifications of synaptic weights and time-dependent parameters were made in order to reproduce neurophysiological recordings in the basal ganglia (see Fig. 4.12).

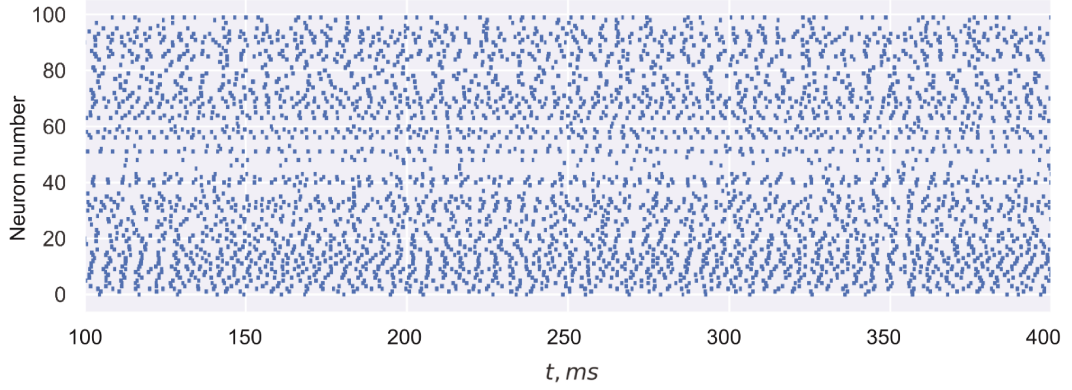


Figure 4.10: Raster plot of a simulated motor cortical activity in the resting state. Oscillatory patterns were modeled with a broad normal distribution centered at 18 Hz. In the PD affected network, the firing in the β -band is increased (see Fig. 4.12), though it cannot be directly observed in the raster plot.

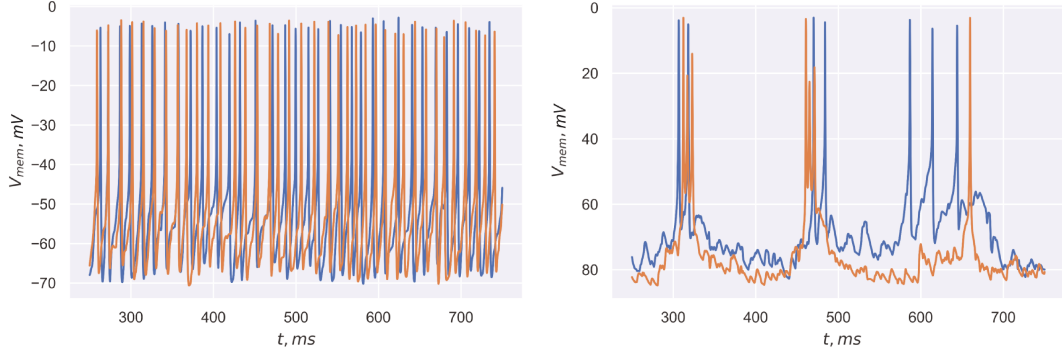


Figure 4.11: Simulated single unit activity in the ventral anterior thalamus shown for two representative neurons. **Left:** a regular single-spike mode in the normal state. **Right:** in the PD state, rebounding occurs in response to the bursting inhibition via the pallidothalamic pathway.

Among various potential biomarkers, here a metric was considered that is not localized in the basal ganglia, but directly modulated by its activity. In particular, we looked into the DBS effect on normalization of the VA-thalamic firing with and without STD in the GABAergic synapses of pallidothalamic neurons. The normalization was quantified with the following goal function:

$$f_{\text{goal}} = \alpha(BR_{\text{Normal}} - BR_{\text{PD}}) + (1 - \alpha)(SP_{\text{Normal}} - SP_{\text{PD}}), \quad (4.3)$$

where α is the balancing parameter set to 0.3, BR is the number of bursts and SP is the number of spikes in a one second interval. To minimize f_{goal} , a gradient-based optimization method was applied to activation rates of the network projections affected by STN-DBS, namely, the reciprocal subthalamic-pallidal pathways, the pallidothalamic tract and the hyperdirect pathway. Particular connections for assigned activation rates within the pathways were

selected randomly at each iteration in order to obtain optimal rates that are not defined by a specific pattern. In the network model, optimization within a pathway might lead to solutions that are not attainable with conventional DBS electrodes. And although random selection decreases the convergence, such "averagely optimal" rates are more feasible to be obtained in the volume conductor model. Results of the network optimization are presented in Fig. 4.13 and Fig. 4.14.

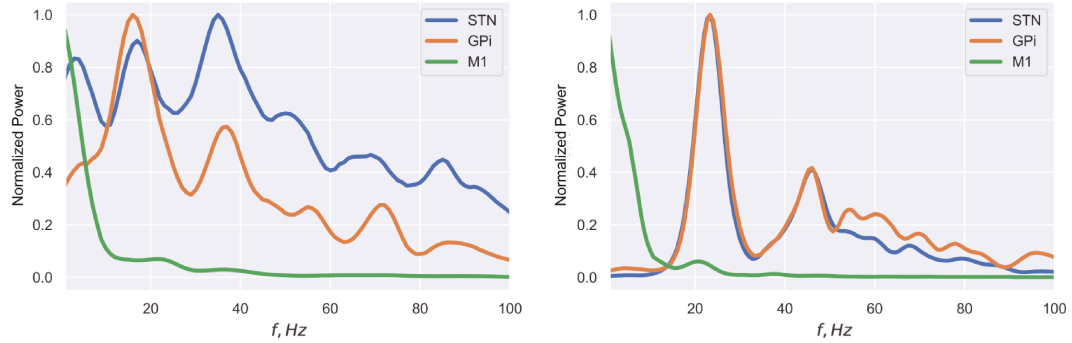


Figure 4.12: Normalized power spectra of the simulated mean activity in the normal (left) and PD-affected (right) network. Note that the β -activity was present in the basal ganglia in both states, but became more prominent in PD due to the abnormal synchronization. Low levels of artificial noise in the simulated basal ganglia nuclei eliminated the $1/f$ trend at the low frequencies.

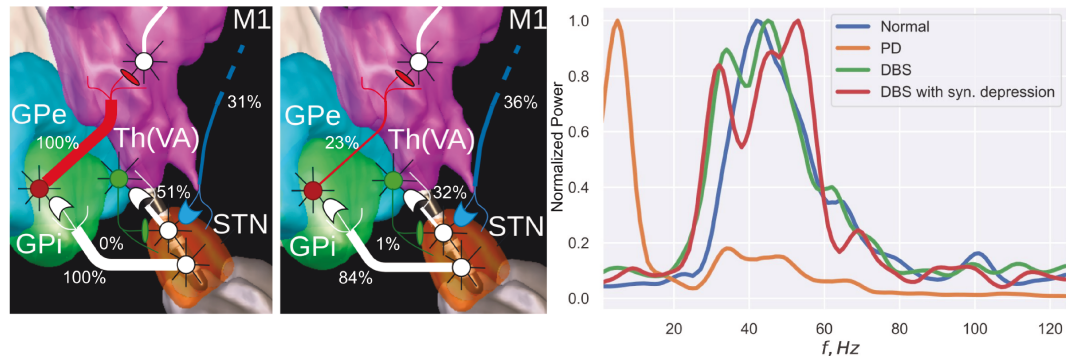


Figure 4.13: Modeling network effects of DBS for normalization of the ventral anterior thalamic firing. **Left:** optimized activation rates induced by DBS without a short-term synaptic depression of GABAergic synapses of pallidothalamic neurons. **Center:** the same with the synaptic depression. Note that in both cases the subthalamopallidal pathways had a large difference in the optimized activation that cannot be achieved with conventional DBS electrodes. **Right:** normalized power spectra of the simulated mean activity of VA-thalamic neurons in four network states. For both DBS-on cases, normalization of the VA-thalamic firing was achieved by elimination of rebounding bursts, but the mechanism was distinctly different (see Fig. 4.14).

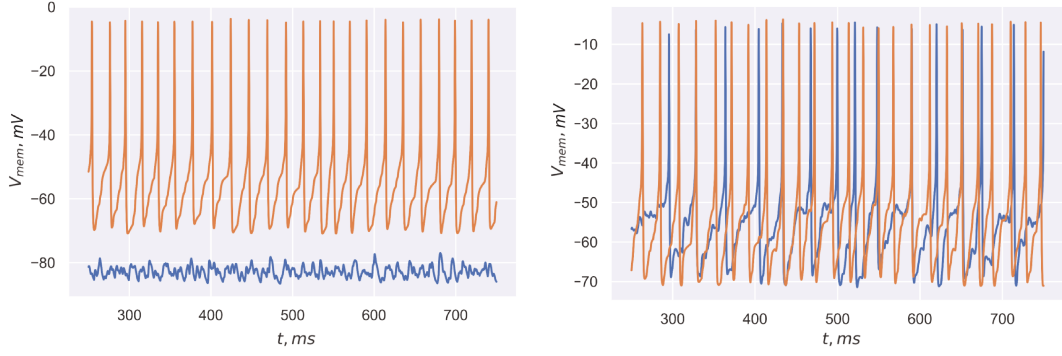


Figure 4.14: *Simulated single unit activity of two representative neurons in the ventral anterior thalamus under STN-DBS. **Left:** without the short-term synaptic depression in the pallidothalamic projections, the stimulation quenched activity in the receiving neurons. **Right:** when the synaptic depression was modeled, the neurons were regularly released from the DBS-induced inhibition, leading to a regular single-spike activity in the γ -band.*

Whether with or without STD, the optimization was able to normalize the VA-thalamic firing (see Fig. 4.13, right). In the latter case, the network model suggested to completely overwrite the activity in the STN-GPi and the pallidothalamic projections, leading to a constant inhibition of the recipient VA-thalamic neurons. Although this would quench the pathological bursting and eliminate the rebounding effect (see Fig. 4.14, left), such a modulation would also disrupt a desirable thalamic release via the direct pathway. On the other hand, this radical stimulation modality might be of interest for animal studies aimed at understanding the role of the basal ganglia output to the thalamus.

In contrast, when modeling the STD of GABAergic synapses of pallidothalamic neurons, normalization was achieved with only a moderate stimulation of the pallidothalamic pathway (23%) and a substantial but not complete recruitment of the STN-GPi projection. In this case, "lesioning" of the β -activity occurred in the pallidum, which bursting patterns were substituted by a high-frequency DBS signal. However, due to the STD, the VA-thalamic neurons failed to follow each pulse and exhibited a regular single-spike firing in the γ -band (see Fig. 4.13, right and Fig. 4.14, right). Hence, it can be theorized that DBS creates a pacing effect that possibly facilitates communication between the basal ganglia and the thalamus. Note that in both cases a moderate excitation of the STN via the DBS-induced hyperdirect pathway activation was also required.

The peculiarity of the presented study is a direct correspondence of the network's structural connectivity to the trajectories of white matter fibers, which "realistic" activation can be quantified by pathway activation modeling. This allows us to evaluate different electrode positions and stimulation protocols with respect to a specific biomarker. The ultimate goal of this on-going project

is to create an automated simulation framework that traces various aspects of neural activity in a patient-specific DBS model. The framework would only require the user to provide a set of multimodal medical imaging, such as MRI and DWI as well as CT data, if the electrode is already implanted, and stimulation protocols for evaluation. Using this patient-specific information, the framework would adjust the model of the basal ganglia-thalamo-cortical network, compute an extracellular field distribution in space and time, quantify its effect on axonal firing and, finally, update the network state. Additionally, implementation of multiscale techniques to the framework would allow a simulation of long-term DBS effects.

4.4 Pathway activation modeling for rat STN-DBS

The two studies presented above used different approaches for estimating an "optimal" pathway activation profile. However, both highlighted the importance of the hyperdirect and the pallidothalamic projections. In this section, I will evaluate how closely these "optimal" profiles can be matched in rat STN-DBS. To do so, the pathways of interest will be reconstructed from water diffusion data, and, using OSS-DBS, activation rate profiles will be computed for different electrode positions (in the vicinity of the STN) and current amplitudes. Although not considered in the basal ganglia-thalamo-cortical network, the activation in the corticofugal pathway will be also controlled, since its stimulation might aggravate akinesia and bradykinesia and evoke motor contractions. Additionally, the cerebellothalamic pathway is included, also omitted in the network analysis. Previous studies have demonstrated an implication of the tract in tremor suppression [25, 166], and in this thesis increase in activation rates has been shown to correlate with improvement of the corresponding UPDRS-III items. In human brain, the cerebellothalamic pathway bypasses the STN, and its stimulation might occur for electrodes medial to the posterior portion of the nucleus. Therefore, it is of interest to investigate whether this mechanism of DBS is utilized when targeting rat STN.

4.4.1 Reconstruction of pathways using diffusion imaging

In Chapter 2, water diffusion in brain tissue were discussed in the context of anisotropic conductivity. Additionally, it was noted that the diffusion can be used to infer the structural connectivity between brain regions. Due to cellular structures, such as white matter fibers, movements of water molecules

are bounded. To assess the effect along different directions, a special sequence of magnetic resonance imaging is applied, where the diffusion is measured in response to gradients of magnetic fields. Acquisition parameters are described by a table that is composed of b-vectors (gradient unit directions) and b-values that define gradient pulse parameters such as width, amplitude and separation in time, with higher b-values corresponding to stronger diffusivity. The displacement of the molecule over diffusion time is estimated by a probabilistic distribution that can be evaluated with different methods such as q-space imaging [198] and diffusion spectrum imaging [199]. Alternatively, one can assume a Gaussian distribution for the diffusion process and describe the measured diffusion-weighted signal $S(\mathbf{r}, b)$ by the Stejskal-Tanner formula [200]:

$$S(\mathbf{r}, b) = S_0 e^{-b\mathbf{r}^T \mathbf{D} \mathbf{r}}, \quad (4.4)$$

where S_0 is the signal measured in absence of magnetic gradients, b summarizes parameters of the measurement, \mathbf{r} is the unit vector in the direction of the gradient and \mathbf{D} is the diffusion tensor, introduced in Chapter 2. By definition, \mathbf{D} is a symmetric positive definite matrix [201], and its six degrees of freedom are obtained by fitting Eq. 4.4. Therefore, at least six gradients in non-collinear directions have to be applied, although it is usual to conduct measurements for multiple angles to obtain a better angular resolution.

Diffusion data are acquired voxel-wise, and, based on directions of principle eigenvectors, which correspond to the largest eigenvalues of \mathbf{D} , one can extract a diffusion trajectory that, in turn, can be used to approximate trajectories of white matter fibers. Note that the resolution of diffusion data in rodents usually varies from 40 to 100 μm , while the fiber thickness is below 10 μm . Therefore, results of tractography do not directly correspond to the distribution of single fibers, but give an approximation of structural connectivity defined by fiber tracts. This is appropriate for our problem, where the relatively large tracts of myelinated axons are reconstructed. In animal studies, it was shown that changes in myelination correspond to changes in fractional anisotropy [202], which is defined as a normalized variation of diffusion along the eigenvectors

$$FA = \sqrt{\frac{1}{2} \frac{(\lambda_1 - \bar{\lambda})^2 + (\lambda_2 - \bar{\lambda})^2 + (\lambda_3 - \bar{\lambda})^2}{\lambda_1^2 + \lambda_2^2 + \lambda_3^2}}, \quad (4.5)$$

where λ is an eigenvalue of \mathbf{D} . In comparison with other diffusion based methods, which were also applied in this section, a tensor-based fiber tractography is the most accessible since data acquisition just for six gradient directions is sufficient. The downside of the method is that only the direction defined by the principle eigenvector is followed, hence it is not able to resolve crossing and branching fibers. For more details on methodology, please refer to [71].

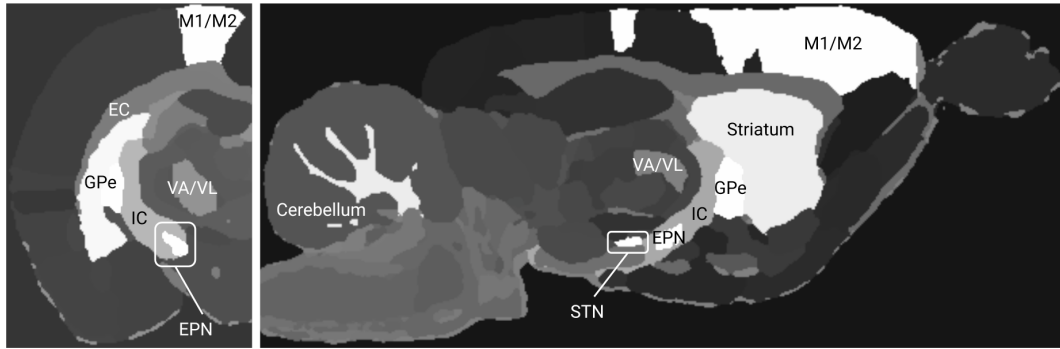


Figure 4.15: *Coronal and sagittal views of brain structures relevant in STN-DBS, visualized in a rat brain atlas [45]. M1/M2 – somatomotor areas, EC and IC – external and internal capsule, respectively, GPe – external segment of the globus pallidus. A delineation of the ventroanterior/ventrolateral nuclei of the thalamus (VA/VL) and the entopeduncular nucleus (EPN, an analogue of the GPi in rodents) was conducted manually following [79].*

In this thesis, fiber tractography is conducted based on high angular resolution diffusion imaging (HARDI) acquired in [45] for the Wistar rat. The data describes diffusion in 61 directions with the b-value set to $3,000 \text{ s/mm}^2$. To classify fiber tracts into pathways, it is convenient to visualize their spatial distribution relative to brain structures. Apart from the diffusion data, Johnson et al supplied a rat brain atlas defined in the same space, sparing the effort of a non-linear normalization of the data to other digitalized atlases. While most of the relevant brain structures were segmented, entopeduncular nucleus (EPN) and the ventroanterior/ventrolateral nuclei of the thalamus had to be delineated manually using the Paxinos and Watson rat brain atlas [79] (see Fig. 4.15).

The HARDI data are truncated and masked to contain only brain voxels (see Fig. 4.16), and diffusion tensors (Fig. 4.17, left) are obtained using the weighted least-squares fitting²⁷ [203]. The fiber tracking is initiated in either of three brain structures depending on the pathway of interest: in the internal capsule for fibers of the hyperdirect and the corticofugal pathways, in the EPN for the pallidothalamic tract and in the cerebellum for the cerebellothalamic tract. The procedure is conducted separately for the pathways in order to reduce computational costs. Purposefully, a relatively low threshold of fractional anisotropy (0.1) is chosen to reduce the number of false negative trajectories, even though it leads to an increase of false positives. The latter are filtered out during a semi-automated pathway classification that imposes additional conditions on the trajectories in relation to brain structures (see Fig. 4.18).

²⁷Additionally, the diffusion tensor data are scaled following the volume conservation approach [75] and used to describe the anisotropic conductivity in the volume conductor model of the rat brain (employed here and in Chapter 3).

In particular, fibers of the hyperdirect pathway have to originate in M1/M2, pass through the internal capsule and terminate in the vicinity of the STN. In reality, the fibers do not terminate in the nucleus, but innervate it with collaterals. However, fiber tractography cannot accurately trace these thin structures, and here it is assumed that a decrease in the fractional anisotropy in the vicinity of the STN corresponds to an inception of the collateral segments. The obtained hyperdirect pathway terminates at the rostro-ventral level of the STN, which is in agreement with a tracing study [204]. In contrast, the corticofugal pathway bypasses the nucleus laterally and merges with the cerebral peduncle. The cerebellothalamic tract is reconstructed from pathways originating in the cerebellum, bypassing the red nucleus and projecting to the ventroanterior/ventrolateral nuclei (Fig. 4.19, left). The pallidothalamic pathway is defined on fibers that connect the corresponding nuclei without trespassing others. Note that unlike in the human brain, the pathway is not clearly separated to ansa lenticularis and lenticular fasciculus in rodents [44]. All reconstruction steps are conducted using the Python package Dipy [71], which was developed specifically for processing of diffusion data, fiber tractography and classification.

Additionally, manual assessment and filtering have to be applied. For example, some fibers, initially classified as the hyperdirect pathway, are removed due to their intersection with the external capsule. These fibers are false positives generated due to the low fractional anisotropy threshold that allowed them to branch off from the internal capsule through the striatum. For the pallidothalamic pathway, fibers have to form a peculiar C-shape [205], and the outliers are removed. The results of the classification were examined by an expert anatomist [206].

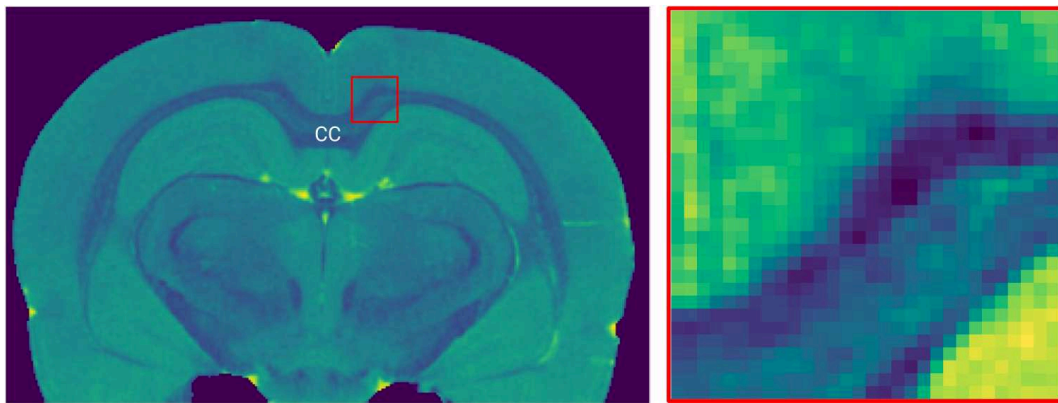


Figure 4.16: Coronal view of the non-diffusion-weighted sequence S_0 in the masked and truncated HARDI data from [45]. The highlighted region in the corpus callosum (CC) is used below to visualize different diffusivity metrics.

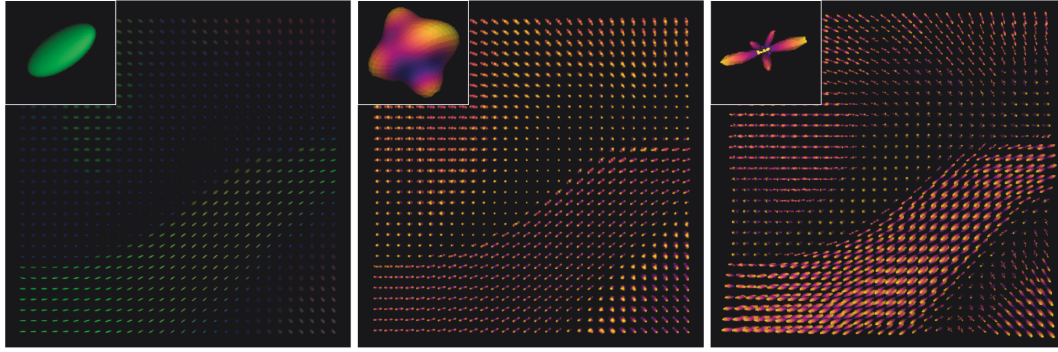


Figure 4.17: *Different representations of the voxel-wise defined diffusivity: tensor ellipsoids (left) and orientation distribution functions using the constant solid angle and the constrained spherical deconvolution methods, respectively. Note that all three methods would be suitable for a reconstruction of the corpus callosum fibers.*

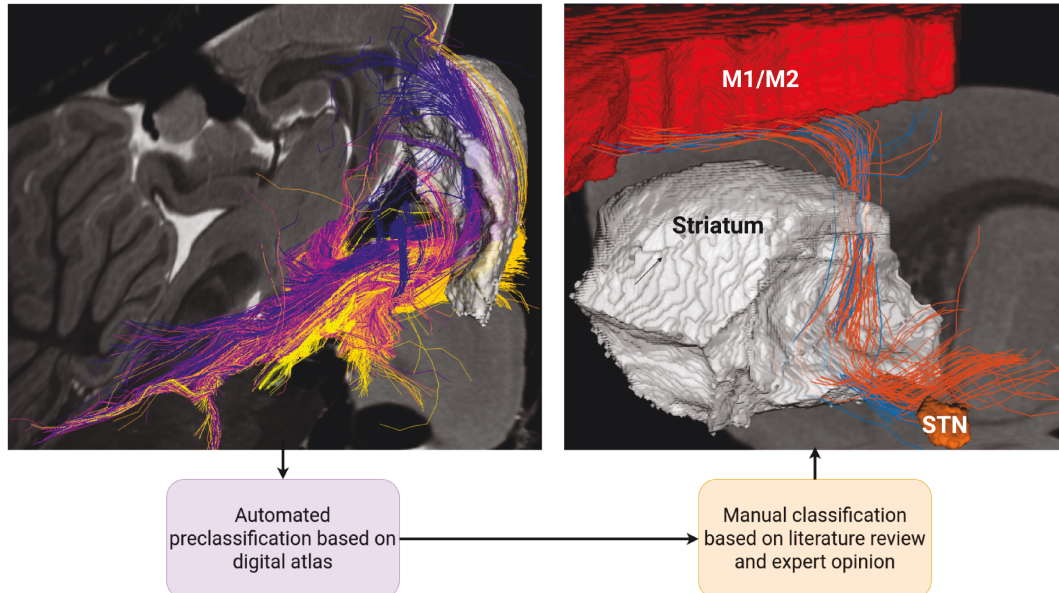


Figure 4.18: *Workflow of the pathway reconstruction for the hyperdirect and the corticofugal pathways. First, tracts are seeded in the internal capsule and have to propagate to the somatomotor area of the cortex. Second, fibers that pass far from the STN are automatically removed. The rest are grouped depending on whether they terminate in the vicinity of the nucleus. If not, the fibers should merge with the cerebral peduncle or they are discarded otherwise. Finally, a manual evaluation is conducted, which removes outliers and non-physical trajectories; in this case these were the fibers trespassing the external capsule. The fibers remaining in the two groups are considered the hyperdirect (blue) and the corticofugal (orange) pathways.*

Dipy also offers other fiber tractography methods that evaluate directionality based on orientation distribution functions (see Fig. 4.17). Here, I used the super-resolved constrained spherical deconvolution [207] with an anatomically-

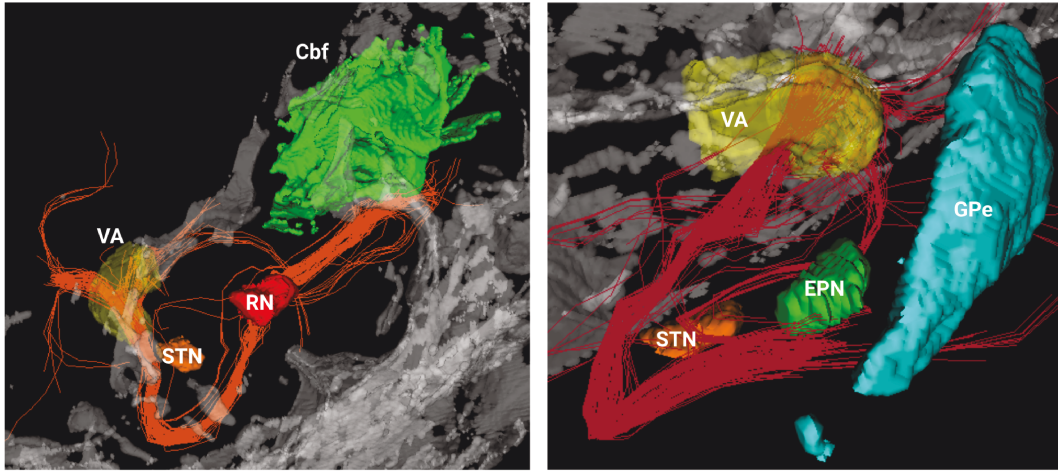


Figure 4.19: *Reconstruction of the cerebellothalamic (left) and pallidothalamic (right) pathways. For the former, more lateral trajectories could be expected. Note the C-shaped trajectory of the pallidothalamic pathway, which is in accordance to [205]. Cbf – cerebellar fibers, RN – red nucleus.*

constrained tractography [208] that accepts fibers terminating in grey matter and rejects those terminating in CSF. Furthermore, I tested the constant solid angle method [209] constrained by a threshold for generalized fractional anisotropy [210]. Results for an attempted hyperdirect pathway reconstruction are presented in Fig. 4.20. Both of these methods, as well as the tensor-based tractography, are applied deterministically, i.e. directions in the voxels are selected based on some criteria (diffusion along the principal axis, orientation distribution function, curvature, etc.). Another approach is a probabilistic tractography that chooses the direction based on a Monte Carlo sampling applied to the orientation distribution function (see Fig. 4.20, right).

Notably, the considered alternative methods failed in the reconstruction of fibers projecting from the cortical areas, and therefore the tensor-based tractography is employed in the thesis. In total, 401 trajectories in four pathways are obtained: hyperdirect – 28, corticofugal – 53, cerebellothalamic – 160, pallidothalamic – 160. It is possible that some fibers that pass through the lateral portion of the striatum and are classified as a part of the hyperdirect or the corticofugal pathways, actually belong to the indirect pathway, which cannot be distinguished using solely geometric considerations²⁸. Again, I have to emphasize that the reconstructed trajectories are not in one-to-one correspondence with white matter fibers. However, in the particular problem, activation rates rather than the absolute number of activated fibers are of interest. Hence, such a description of pathways is appropriate assuming that fibers follow a

²⁸Note that the presented classification method does not allow to reconstruct pathways that transverse brain structures without innervating them. This makes practically impossible to distinguish the direct and indirect pathways that both pass through the GPe.

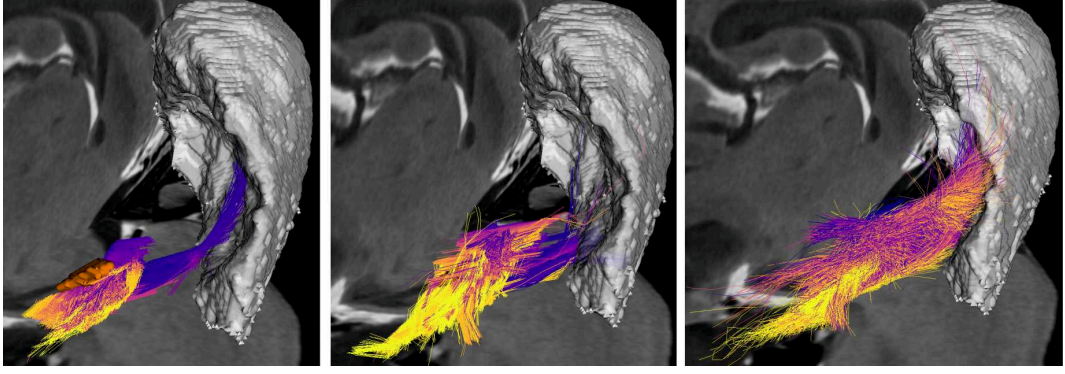


Figure 4.20: *Alternative approaches to fiber tractography considered in the thesis. **Left:** an anatomically constrained tractography using the constrained spherical deconvolution. **Center:** the constant solid angle method with a thresholding by generalized fractional anisotropy. **Right:** a probabilistic sampling of the orientation distribution function. The tensor-based tractography generated more physiologically plausible trajectories (see Fig. 4.18) possibly due to insensitivity to secondary diffusion directions.*

Gaussian distribution along the trajectories. In general, it must be noted that a diffusion based fiber tractography is prone to generate false positive trajectories [211], and an absence of false negatives is not ensured either [212]. Bearing this in mind, diffusion based fiber tractography can be considered as a first approximation of structural connectivity that should be further analyzed with anatomical and histological methods [213].

4.4.2 Optimization of pathway activation

To reiterate, the research question of this chapter is whether stimulation of rat STN can reproduce profiles of activation rates similar to those considered therapeutic in human STN-DBS. Previously, we discussed different approaches to determine therapeutic profiles, and Table 4.1 presents three that are considered in this section, further referred as profiles I, II and III. Note that the local subthalamopallidal pathways are not included in the analysis: apart from complications related to diffusion based pathway reconstruction, it is questionable whether pathway activation modeling is an appropriate method for such local circuits [144], also taking into account a presumable neurological damage in the pathway caused by the implantation (see Fig. 4.2).

With the optimal profiles defined ($\mathcal{A}_{\text{optimal}} = [\mathcal{A}_{\text{HDP}}, \mathcal{A}_{\text{CF}}, \mathcal{A}_{\text{GPi-Th}}, \mathcal{A}_{\text{Cb-Th}}]$), we now have to solve an optimization problem, where the electrode placement and the current amplitude are the optimized parameters, and the goal is to minimize the difference between an optimal profile and activation rates computed in the volume conductor model of the rat brain, with the difference

Table 4.1: *"Optimal" pathway activation profiles of human STN-DBS derived in the retrospective clinical study on motor improvement [144] and in the network analysis of neural activity normalization in the ventral anterior nuclei of the thalamus (VA). The latter was conducted with and without the short-term synaptic depression (STD) in the pallidothalamic neurons. For the corticofugal pathway, which stimulation is associated with motor contractions and dysarthria, the penalization is set for activation rates above a threshold of 2.5%. The cerebellothalamic pathway is added to the analysis due to its involvement in tremor alleviation.*

Pathway	UPDRS-III score improvement	VA norm. (no STD)	VA norm. (with STD)
HDP	55%	31%	36%
Pallidothalamic	50%	100%	23%
Corticofugal	$\leq 2.5\%$	$\leq 2.5\%$	$\leq 2.5\%$
Cerebellothalamic	60%	—	—

measured by the previously described Canberra distance [171]. Since it is a normalized metric, smallest differences in activation rates for detrimental pathways result in high contributions to the distance. In the retrospective clinical study, the target activation rates for the corticofugal tract were nearly zero, and, considering its proximity to the hyperdirect pathway, that would lead to a stalling of optimization. Therefore, a threshold of 2.5% is chosen that was optimal for the tract descending from the SMA, which had the highest impact among the corticofugal branches in the weighted target profile (see Fig. 4.6). Contributions for lower activation rates are nullified, but in order to emphasize the importance of low activation in the pathway, its weighting factor in the Canberra distance is set to 4.0^{29} . For the cerebellothalamic pathway, which activation did not significantly influence the correlation of the weighted profile with motor improvement (see Fig. 4.6), the weighting factor is decreased to 0.25 (1.0 for the rest).

The goal function defined by the Canberra distance depends on activation rates of the non-trivially distributed pathways, and it belongs to the class of non-convex functions with multiple local minima. In a preliminary analysis, it was determined that the simulated annealing algorithm [214] is well suitable for the particular problem. In short, the algorithm follows an analogy of annealing process for a metal, where the global minimum corresponds to the state of the maximal crystallization ergo the minimal energy. Transitions between states are based on random perturbations of optimized parameters, and those result-

²⁹The choice of the weighting factors here is heuristic in order to generalize the conclusion on the translatability. Ideally, when considering a specific hypothesis, the weighting factors should be set to the same values within one study, independent from the brain anatomy.

ing in a lower energy state are always accepted. The peculiarity of the process is a probabilistic acceptance (governed by a special case of the Metropolis–Hastings algorithm [214, 215]) of transitions that lead to states of a higher energy at high temperatures, allowing a better exploration of the parameter space. During the cooling, regulated by an annealing schedule, the probability of acceptance for a higher energy solution is decreasing. The particular implementation employed here is the generalized simulated annealing [216] that combines the classical and the fast simulated annealing, providing a fast convergence yet avoidance of local minima by balancing between those strategies.

The optimization is conducted in two loops: the outer moves the electrode in the vicinity of the STN, and the inner optimizes the current amplitude for the given electrode placement. The reason for this separation is the computational efficiency. While repositioning requires to recompute the whole FEM model, results for different current amplitudes are obtained by simple scaling of the field solution in time domain, allowed due to the linearity of *Laplace’s equation* (Eq. 2.14). In this case, only the cable equation has to be recomputed to obtain activation rates for a new current protocol. For this study, the spatial parameters of the electrode placement are bounded by a 2 mm box, centered at the STN and aligned with the main brain axes. In rodents, electrodes are usually concentric and implanted vertically without a tilt, and therefore only three parameters, namely, the tip coordinates, are required to define the position. The current amplitude is limited by 60 μA , but both polarities are allowed. The local optimization is disabled, since the precision of electrode placement in rodent DBS is limited [51]. Moreover, it is also not used when optimizing the current: a precise amplitude is not of interest considering uncertainties introduced by the fiber tractography, the volume conductor model, the axon model, etc. The simulated annealing algorithm is employed for a general exploration of a relatively large spatial parameter space, and, additionally, a grid search is conducted for visualization purposes. It is bounded by a 1 mm box with 0.25 mm step, which is reasonable taking into consideration implantation inaccuracies [51].

The volume conductor model employed in this analysis was previously described in Chapter 3. Since the electrode position varies considerably over the optimization, and conducting mesh refinement for each iteration is costly, a pre-refined initial meshing is used, which accuracy was assessed at ten random positions. McIntyre’s mammalian axon models are allocated on the trajectories previously reconstructed with the diffusion based fiber tractography. For the hyperdirect pathway, the seeding of an axon starts from the trajectory’s closest point to the nucleus’ center of mass, while for passing fibers it is seeded as the midpoint of an axon (see Fig. 4.21). All axons are modeled with a 2.0 μm fiber diameter, the thinnest available for the model. In order to reduce the computational effort, minimal lengths of axon models that do not alter activation rates were determined in a preliminary analysis. For the cerebel-

lothalamic tract, 6 *mm* models are deployed (31 nodes of Ranvier per axon), and the rest of the pathways are simulated with 4 *mm* axons (21 nodes of Ranvier).

Pathway activation modeling is conducted for two electrodes, already considered in Chapter 3: SNEX-100 (Microprobes, MD, USA) and the custom design with the blunt tip suggested in [145]. Apart from the conventional rectangular pulse, a centered triangular and ramp shapes are tested that deliver the half of the charge per phase, which could be an energy efficient alternative [56]. Moreover, the computational model allows to simulate various pulse widths and repetitions rates, but here a conventional clinically relevant 130 *Hz* 60 μ s pulse is employed. Optimized electrode positions, defined by the tip coordinates, are presented in the left column of Figs. 4.22, 4.23, 4.24 for the three optimal profiles.³⁰ The positions are shown in the rat brain atlas [45], and the used abbreviations are collected in Table 4.2. The right column of the figures shows the goal function distributions of the overall most effective simulation protocol, namely, the rectangular pulse injected via SNEX-100. The performance of the custom design electrode for the optimal profiles is presented in Fig. 4.25.

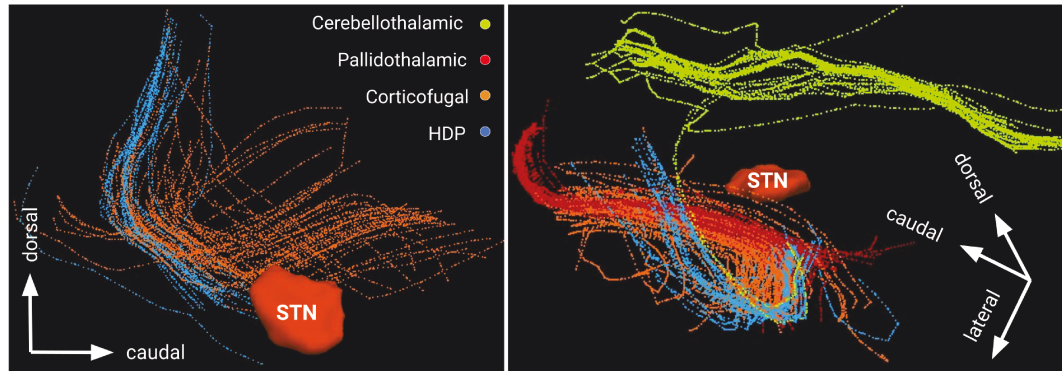


Figure 4.21: Allocation of axon models on the classified pathway trajectories. The models are comprised of compartments that are depicted as separate points. Note that compartments far from the STN are not affected by the extracellular stimulation and are truncated in order to reduce the computational costs.

³⁰Particular activation rates at these optimized positions will be discussed in the next section.

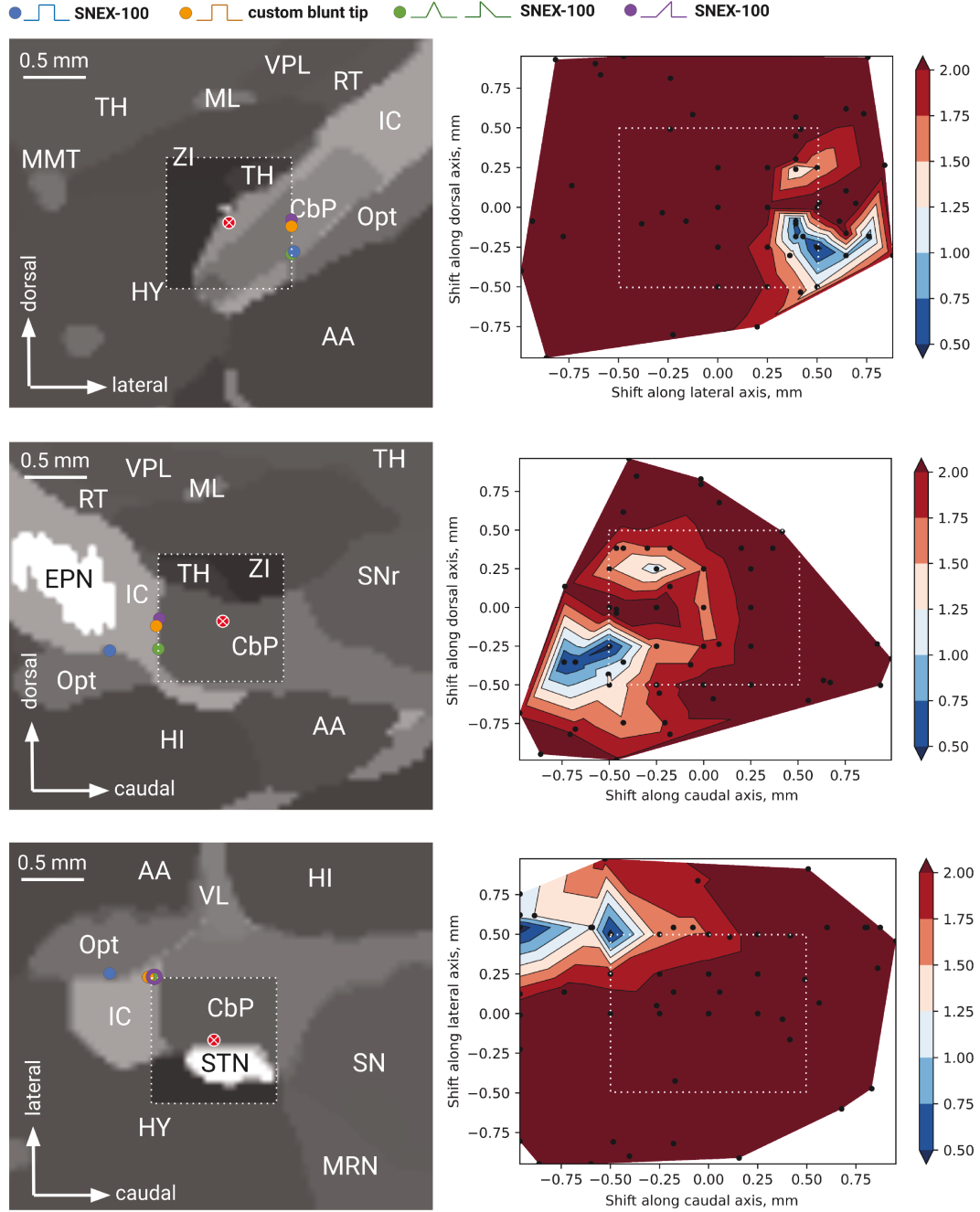


Figure 4.22: Optimizing rat STN-DBS to match the optimal profile that was predictive for clinical motor improvement. **Left column:** optimized placement of the electrodes for various pulses in the coronal, sagittal and axial planes of the rat brain atlas [45], respectively. The planes are shown at the optimal position of SNEX-100 (rectangular pulse), where the STN is not entirely visible (its center of mass is marked in red, and the 1 mm vicinity is highlighted). For abbreviations see Table 4.2. **Right column:** the goal function (the Canberra distance to the optimal profile) visualized in the same planes (with ± 0.1 mm aggregation along the transversal axis) for the stimulation with the rectangular pulse using SNEX-100. The results indicate that the anterior lateral electrode placement relative to the STN is the most effective for matching the pathway activation profile suggested in [144].

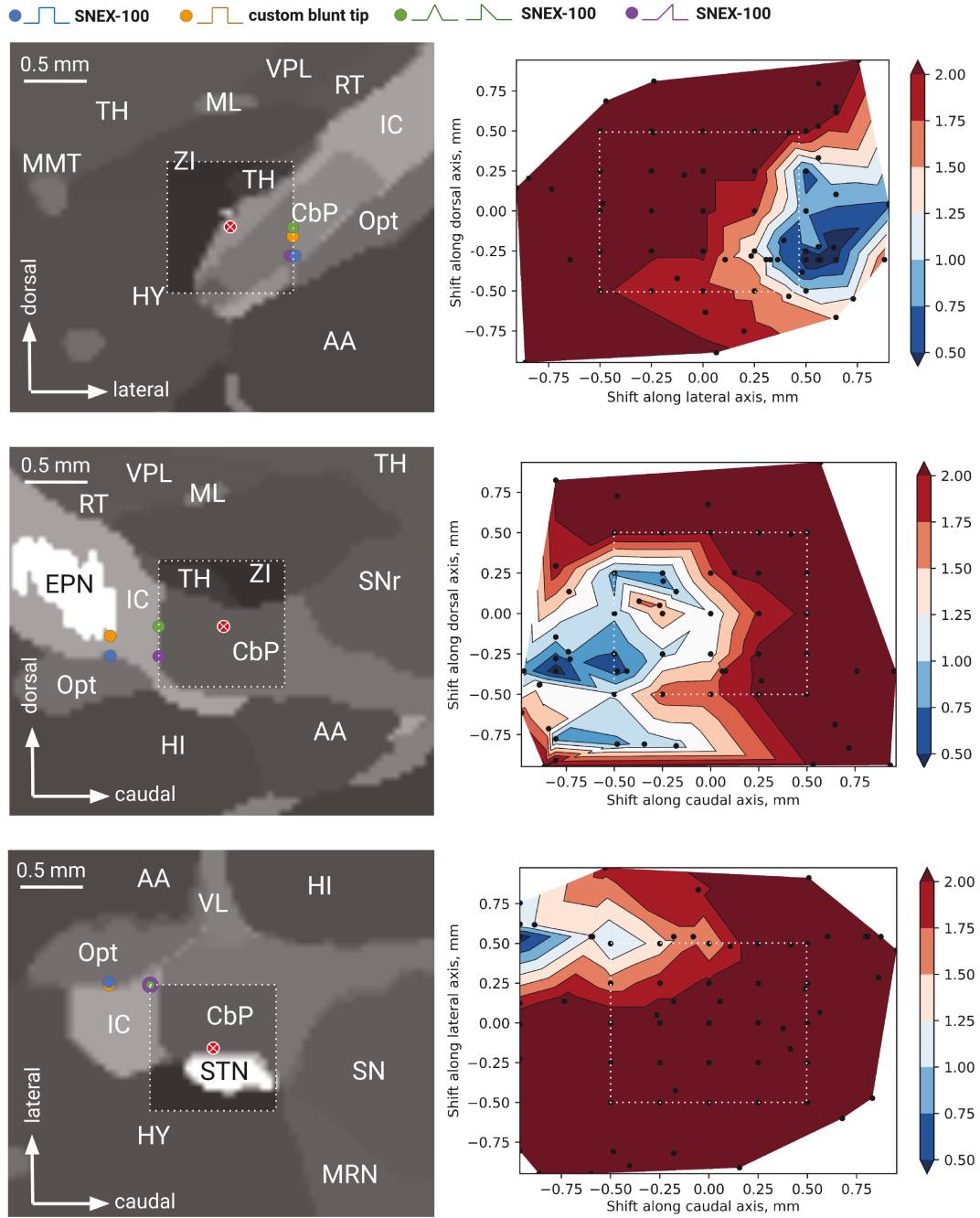


Figure 4.23: Optimizing placement of the electrodes for rat STN-DBS to match the optimal profile that led to normalization of the neural activity in the ventral anterior nucleus simulated in the basal ganglia-thalamo-cortical network (without the short-term synaptic depression of pallidothalamic neurons). The goal function on the right is shown for SNEX-100, conventional rectangular pulse. The results indicate that the anterior lateral electrode placement of relative to the STN is the most effective for the normalization. For abbreviations see Table 4.2.

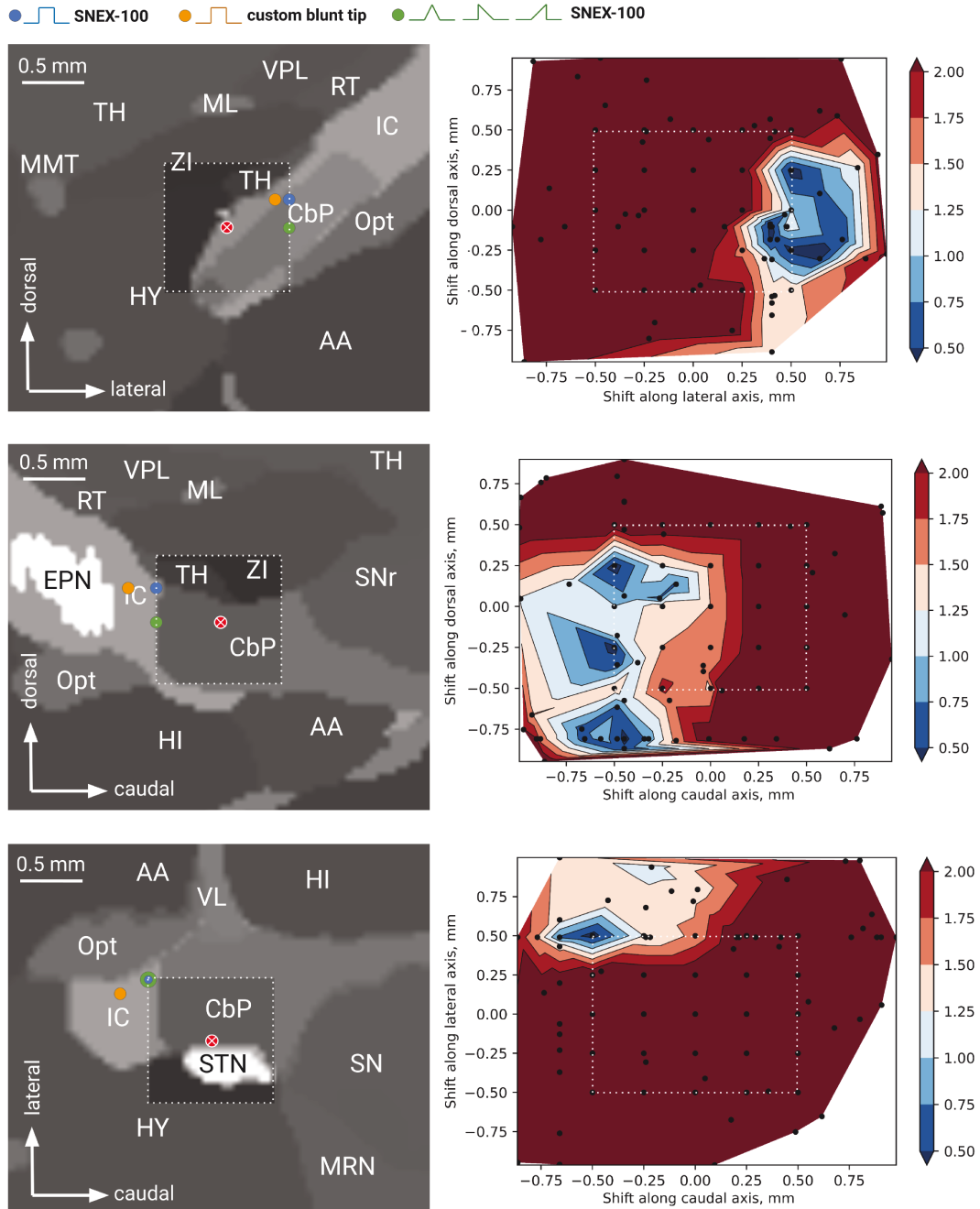


Figure 4.24: Optimizing placement of the electrodes for rat STN-DBS to match the optimal profile that led to normalization of the neural activity in the ventral anterior nucleus simulated in the basal ganglia-thalamo-cortical network (with the short-term synaptic depression of pallidothalamic neurons). The goal function on the right is shown for SNEX-100, conventional rectangular pulse. The results indicate that the anterior lateral electrode placement relative to the STN is the most effective for the normalization. Note that different positions along the dorsal axis are comparably effective. For abbreviations see Table 4.2.

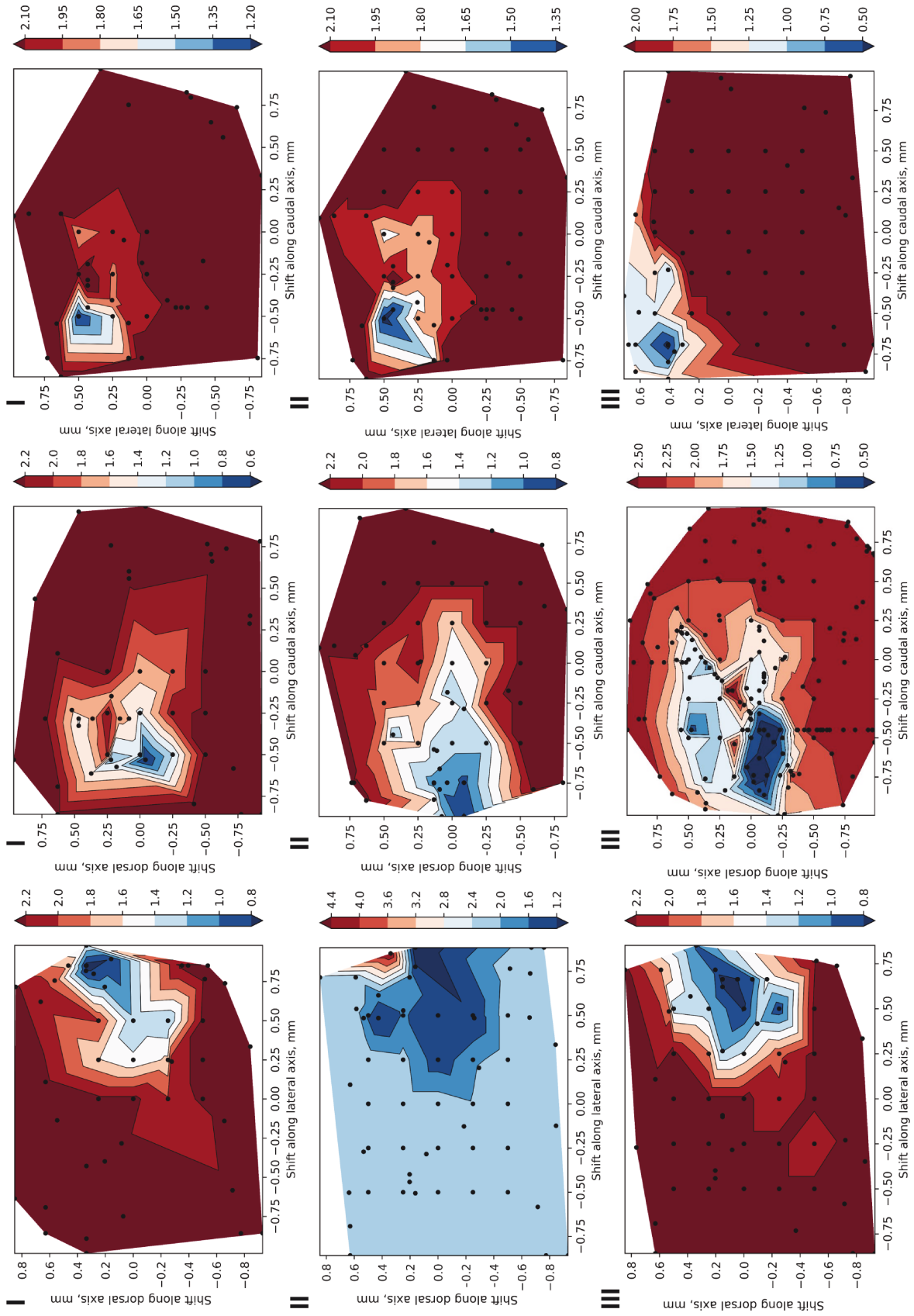


Figure 4.25: Goal functions in the coronal, sagittal and axial planes computed for profiles I, II and III (row-wise) when optimizing placement of the custom electrode design with the blunt tip. The planes are shown at the optimal position of SNEX-100 (rectangular pulse), and therefore minimal values might differ for the same profile. Note that for profile II (coronal plane), a suprathreshold activation of the corticofugal pathway can be observed (trivial null-activation solutions were discarded if possible).

Table 4.2: *Abbreviations for brain structures in Figs. 4.22, 4.23, 4.24. Note that the number of structures listed here are also targets used in human DBS for various diseases, hence their stimulation might compromise the integrity of experiments.*

Abbreviation	Brain structure	DBS target
AA	Amygdalar area	
CbP	Cerebellar peduncles	✓
EPN (GPi)	Entopeduncular nucleus	✓
HI	Hippocampal formation	
HY	Hypothalamus	
IC	Internal capsule	
ML	Medial lemniscus	
MMT	Mammillothalamic tract	
MRN	Midbrain reticular nucleus	
Opt	Optic tract	
RT	Reticular nucleus	
SNr	Substantia nigra pars reticulata	✓
STN	Subthalamic nucleus	✓
TH	Thalamus uncharted	✓
VL	Lateral ventricle	
VPL	Ventral posterolateral nucleus	✓
ZI	Zona incerta	✓

For optimal profiles I and II, the most effective stimulation sites coincide, but with different current amplitudes ($-60 \mu A$ and $-40 \mu A$, respectively). It should be noted, however, that the sites are located outside of the 1 mm box around the STN, and can be considered as EPN targeting. For profile I, a comparable solution (+9% of the Canberra distance) is found in the close vicinity of the nucleus, but it is not the case for profile II (+54%). The most favorable stimulation site for profile III is located in the vicinity of the STN ($-60 \mu A$), and different depths of the implantation can be considered (see Fig. 4.24, middle row).

For the unconventional signals, only results of the grid search are presented. The performance of these protocols³¹ is significantly lower in comparison with grid solutions for the rectangular pulse for all three profiles: +130%, +54%

³¹Results among the unconventional signals are comparable, but, on average, the decreasing ramp shape performed better.

and +166%, respectively. Hence, the efficiency of these signals for the particular problem is questionable. If they are to be tested in animal experiments, the ramp pulses are preferred over the centered triangular due to the relative energy efficiency. The spectrum of the latter contains more power at the lower frequencies, at which the impedance is significantly higher due to the electrical double layer [96].

The custom design electrode also performs worse than SNEX-100 (+53%, +24%, +9%), though the difference is moderate for optimal profile III. The optimized stimulation sites are comparable among the electrodes, with a slightly more dorsal placement of the custom design. The overall lower efficiency is attributed to the field focalization, while the stimulation of the spatially distributed axons would require higher current amplitudes, which are, however, limited by the charge density per phase. It can be concluded that the custom electrode is less applicable than SNEX-100 for simultaneous neural modulation in several pathways.

For the considered optimal profiles, the optimized implantation sites are located anterior and lateral to the STN, independent of the electrode and signal type (see Fig. 4.26). It is of no surprise since the reconstructed hyperdirect pathway, moderately activated in the profiles, terminates in this area. However, the fact that the optimized electrode trajectories reside in the vicinity of the EPN is not fully consistent with reports on EPN-DBS, which has been shown to be inefficient against parkinsonian symptoms [217] in contrast to GPi-DBS in humans. Furthermore, an electrode implantation for optimal profiles I and II might induce a significant lesioning of the caudal EPN and the pathways of interest: OSS-DBS reported that 21% and 18% of streamlines in the pallidothalamic and hyperdirect pathways, respectively, intersected with the SNEX-100 geometry or the encapsulation layer. Taking into account probable inaccuracies of the diffusion based tractography for collaterals of the hyperdirect pathway, it is advised to pursue a more conservative implantation strategy, which can be defined according to Fig. 4.22 and Fig. 4.23. Most importantly, the goal functions shown in the figures reveal an overlap of the optimal sites in 0.5 mm vicinity of the STN center of mass. This finding implies that various activation profiles might be tested in one animal only by adjusting the stimulation current.

4.4.3 Effect of uncertainty in tissue conductivity

Since pathway activation modeling involves various uncertain parameters, reporting exact activation rates for the optimized implantation sites might not be reasonable. A major uncertainty in the model is introduced by the brain

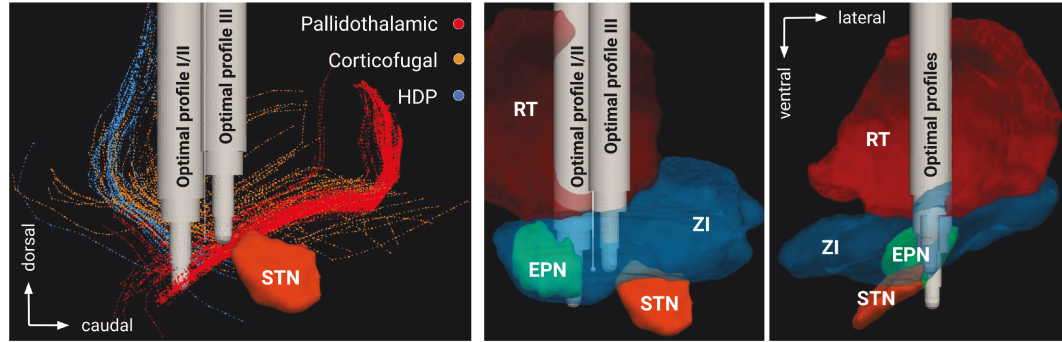


Figure 4.26: *Optimized electrode placement (for profiles I, II and III) relative to the classified pathways and relevant brain structures. For visualization purposes, only the trajectory (line with a sphere) is shown for the custom electrode with the blunt tip, which performed comparably to SNEX-100 for normalization of the neural activity in the ventral anterior nucleus (with enabled short-term synaptic depression of pallidothalamic neurons). Note that all trajectories are anterior lateral to the STN and potentially cause a neurological damage in the zona incerta (ZI). RT – reticular nucleus of the thalamus.*

tissue conductivity³² [65], and here its effect is quantified with the analysis previously described in Chapter 3. Based on variations reported in [60], probability density functions are defined for scaling factors of grey and white matter conductivity (see Fig. 4.27). Using UncertainPy [149], a polynomial chaos expansion is computed by solving the model for conductivity values determined by the collocation method with Hammersley sampling [148]. Pathway activation rates at the collocation points and the first order Sobol’ indices for the optimized implantation sites are provided in Fig. 4.28 and Fig. 4.29, while the mean values and the standard deviations, computed from the expansion, are collected in Table 4.3.

When comparing Tables 4.1 and 4.3, it can be seen that relatively close matches are possible for optimal profiles I³³ and III, though the exact activation level in the hyperdirect pathway could not be achieved. A high activation of the pallidothalamic tract in optimal profile II is hampered by the required moderate activation in the hyperdirect pathway and the avoidance of the corticofugal tract. In general, it can be stated that rat STN-DBS with the considered electrodes allows to induce a pattern of balanced activation, but not a precise targeting of pathways.

Uncertainty in the tissue conductivity significantly affects the levels of activation, especially in the hyperdirect pathway. From the computed Sobol’ indices,

³²While a misplacement of the electrode would significantly alter the pathway activation, the effect can be assessed from the previously conducted placement optimization.

³³Bear in mind that the activation level in the cerebellothalamic pathway has a low weighting factor for optimal profile I.

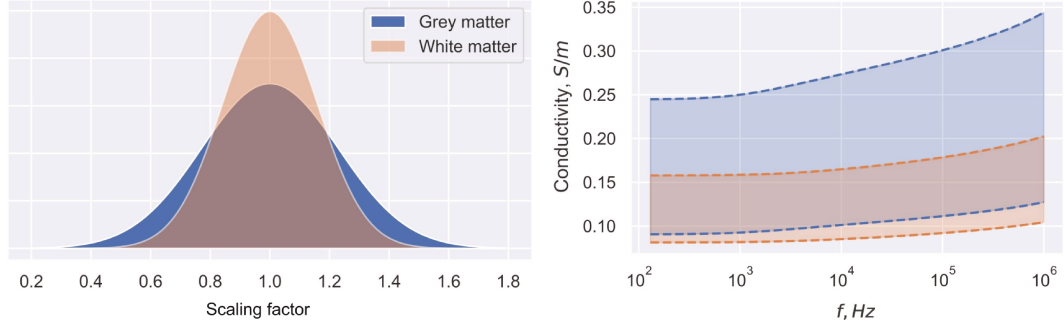


Figure 4.27: *Uncertainty in brain tissue conductivity. **Left:** stochastic scaling factors for the conductivity are chosen from the normal distributions, which standard deviations are derived from [60]. **Right:** actual conductivity values used in Eq. 2.14 over the DBS power spectrum shown within the two standard deviation margins (95.45%).*

Table 4.3: *Mean values \pm standard deviations of approximated pathway activation for the optimized protocols for profiles collected in Table 4.1. The approximation is calculated using the surrogate polynomial expansion model for the considered uncertainties in grey and white matter conductivity. Activation of the cerebellothalamic pathway was not observed in the computational model throughout the optimization and uncertainty quantification. Note that the surrogate model could not accurately evaluate the standard deviation for the corticofugal pathway, which activation dependency violated the smoothness criterion.*

Pathway	Profile I	Profile II	Profile III
HDP	48.5% \pm 7.1%	28.0% \pm 11.7%	29.7% \pm 18.4%
Pallidothalamic	52.9% \pm 4.4%	50.1% \pm 3.8%	24.5% \pm 3.2%
Corticofugal	1.6% \pm 7.2%	—	2.9% \pm 3.0%

it is evident that white matter has a higher effect, which could be expected since the optimized implantation sites and the axonal pathways reside in this tissue. The effect is also observed in the isotropic version of the volume conductor model. Based on these results, it can be concluded that a further investigation of the dielectric properties of brain tissue is required when modeling pathway activation in rodents. It should be noted that the standard deviation of activation in the corticofugal pathway could not be accurately estimated with the polynomial chaos expansion, which is evident from the results of Hammersley sampling (see Fig. 4.28). The reason is a non-smooth dependency of the model's output on the uncertain parameters. Overall, the activation in the corticofugal pathway for the optimized protocols is low, so the motor contractions would not be expected. The results imply that the current amplitude in rat STN-DBS is limited by the safety issues related to the electrode integrity,

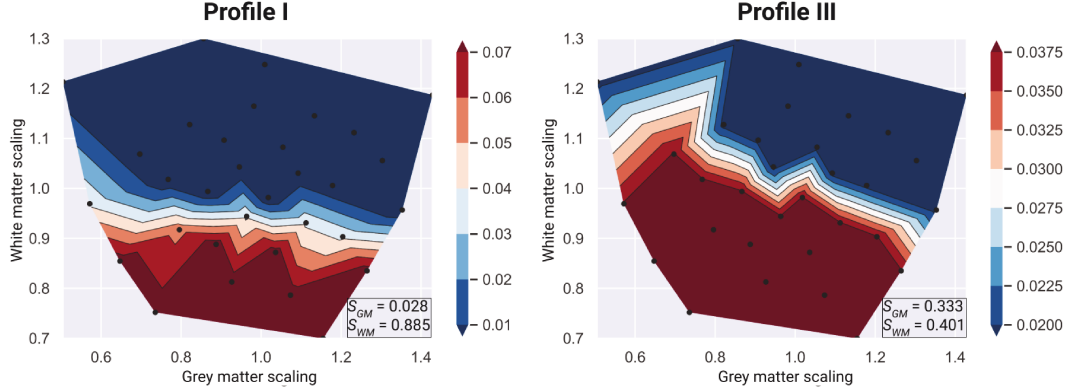


Figure 4.28: Activation rates in the corticofugal pathway computed on the collocation points with Hammersley sampling, further used to derive the surrogate polynomial expansion model. Rows correspond to the optimized protocols for pathway activation profiles I and III suggested in Table 4.1. No corticofugal activation was computed using the optimized protocol for profile II. S_{GM} and S_{WM} are the first order Sobol' indices for the scaling factors of the grey and white matter conductivities, respectively. Note that their effect is comparable for the optimized protocol of profile III, but not for profile I.

such as charge density per phase, rather than stimulation thresholds for capsular side-effects, which is the case in clinical application. This aspect is of importance when choosing a polarity of the stimulation, since anodic pulses, which locally hyperpolarize the neural membrane, are associated with higher thresholds for initiation of side-effects [218]. In contrast, cathodic pulses (locally depolarizing) perform better for the considered optimal profiles, while the same anodic amplitudes yield significantly lower activation, especially in the hyperdirect pathway.

At last, one could note that the cerebellothalamic pathway is not extensively discussed in the section. For its reconstructed trajectories, the DBS-induced activation is not observed in the model, and it was also negligible during the electrode placement optimization. It is important to mention that the reconstructed pathway does not contain fibers that ascend more laterally, near the zona incerta, to the ventral thalamus [219]. Nevertheless, it can be theorized that the cerebellothalamocortical network, associated with tremor modulation, is not extensively engaged by STN-DBS in the rat brain. At the same time, it might not be crucial for behavioral rodent studies, where tremor related symptoms are rarely investigated.

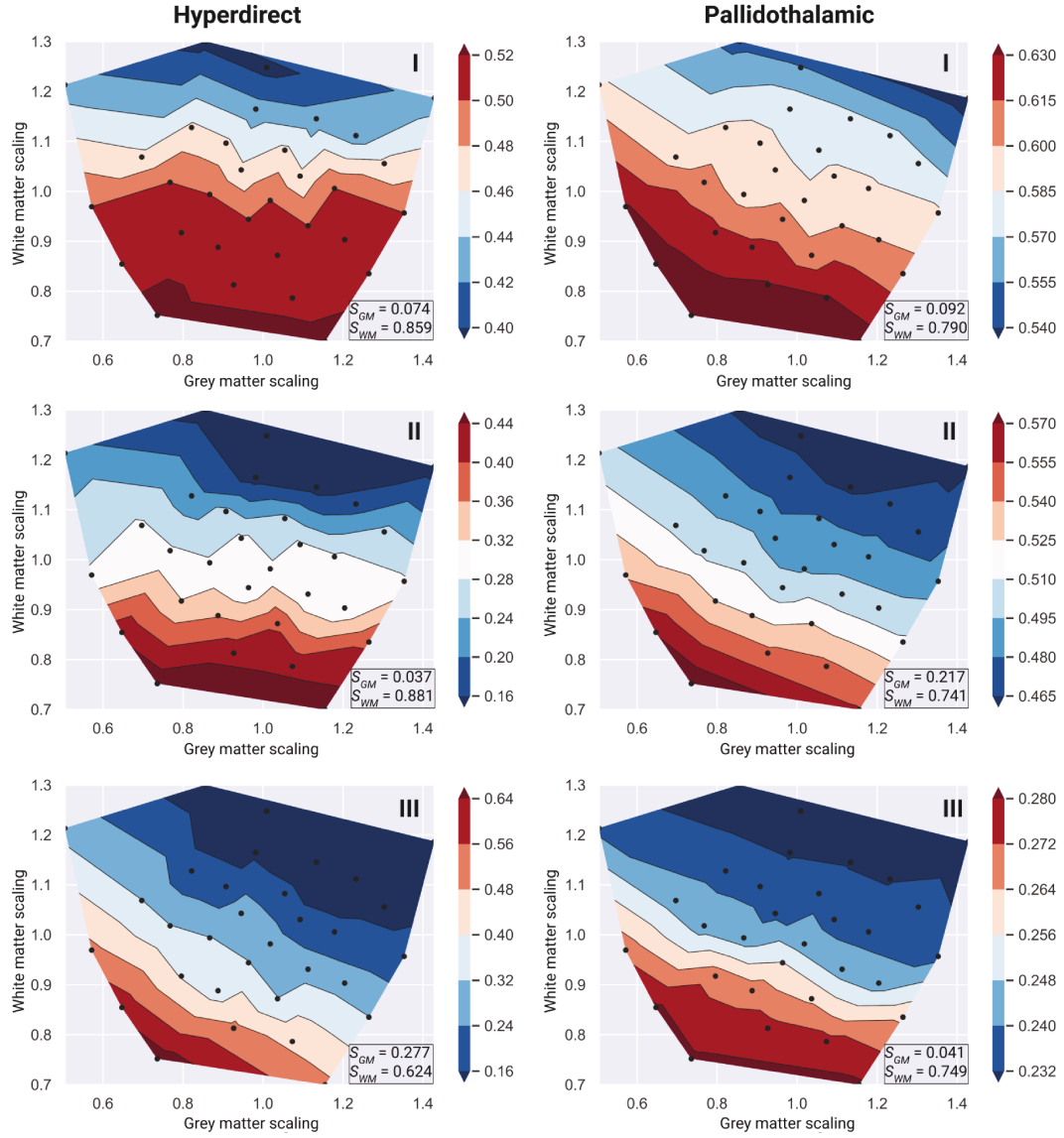


Figure 4.29: Activation rates in the hyperdirect and pallidothalamic pathways computed on the collocation points with Hammersley sampling, further used to derive the surrogate polynomial expansion model. Rows correspond to the optimized protocols for the three pathway activation profiles suggested in Table 4.1. S_{GM} and S_{WM} are the first order Sobol' indices for the scaling factors of the grey and white matter conductivities, respectively. Note that the uncertainty has a larger effect on the hyperdirect pathway activation, and the variation of the white matter conductivity has a higher impact on the activation for all three protocols.

4.5 Limitations of the pathway activation modeling

Apart from simulation inaccuracies that are inherent to volume conductor modeling³⁴, additional limitations are introduced by the parameteric uncertainty of pathway activation modeling. First of all, reconstruction of pathways using diffusion based tractography and basic anatomical considerations is prone to generate both false positive and false negative trajectories. The latter is predominant in the thesis since a conservative strategy was pursued during the reconstruction. As it was conducted using the rat brain atlas, averaged among six healthy animals, and the diffusion data, obtain in one animal, an assumption of low individual and disease related variability had to be made³⁵. Secondly, the local subthalamopallidal circuitry was not reconstructed since no clear distinction between the direct and the indirect pathway could be observed with the employed approach. Yet, even interpretation of pathway activation results is challenging for these short projections that are greatly affected by the electrode implantation. Furthermore, data on the pathway-specific axonal morphology are scarce, and even within a pathway, there might be significant differences in myelination ergo excitability of neurons. In general, one can argue that even smaller fiber diameters should be considered for rat brain modeling [204]. Apart from that, the thesis did not elaborate on the SNr projections, since they were not discussed in the presented studies on pathway activation in human DBS. While the SNr is functionally similar to the EPN in the basal ganglia circuitry, its structural connectivity is unique, and inclusion of the corresponding pathways is important for an accurate representation of the DBS-induced neuromodulation. Nevertheless, following the state-of-the-art methods, the presented study was able to elucidate the translatability problem formulated in this thesis.

³⁴Among those are inaccuracies arising from tissue segmentation, conductivity and anisotropy assessment, simplification of the effects on the electrode-tissue interface, etc.

³⁵In [45], it has been show that individual variations within the same strain and sex are not extensive.

Chapter 5

Conclusion

The aim of this thesis was to evaluate the translatability of DBS studies in humans and rodents using modeling techniques of brain stimulation. Although clinical effects of DBS on PD motor symptoms have been reliably reproduced in rodent studies [220, 221, 222], it is not yet clear how similar mechanisms of action are in these brains of the radically distinct anatomy. Importantly, discrepancies in the mechanisms could lead to unsuccessful translation of findings discovered in animal studies to clinical practice. Therefore, it is crucial to conduct comparative analysis not only for behavioral outcome but also for electrophysiological and neurochemical changes induced by the stimulation. Complementary to *in vivo* research and analysis of biological samples, *in silico* computational models can be employed to simulate various aspects of DBS that are impossible or extremely challenging to be studied directly. Furthermore, such models can provide an additional guidance to increase the integrity of animal experiments.

It is well known that DBS exerts a wide range of electrochemical and biological effects on a different temporal and spatial scale. In the context of motor symptoms' treatment in Parkinson's disease, fast emerging alleviation of tremor and rigidity is observed [223], supposedly caused by the DBS-induced neuromodulation. In particular, altering the extracellular electric potential creates a short-term depolarization of the neural membrane that might lead to an initiation of action potential. Nowadays, it can be stated that computational models allow simulating these effects with a certain level of confidence. By incorporating heterogeneity, anisotropy and dispersiveness of brain tissue in a volume conductor model, a highly accurate electric field distribution in space and time can be obtained. For large-scale neural simulations, cable equation models of different complexity were suggested, which can be solved efficiently using advanced methods of numerical integration. The placement of these abstract neurons in the volume conductor model may be inferred from medical

imaging, e.g. axon allocation can be conducted based on water diffusion in white matter fibers.

In the course of my doctoral studies, these and other relevant methods were incorporated into the simulation software OSS-DBS [140] that was later used to conduct various studies [51, 61, 144, 145], both in human and rodent DBS. In this thesis, OSS-DBS was employed for two distinctly different analyses. First, local effects of rat STN stimulation were modeled. Apart from computing the volume of tissue activated and its approximations, a direct effect of the electric field on isolated neurons (soma and dendritic trees) was investigated. The second part of the thesis focused on the stimulation of white matter tracts assessed in OSS-DBS using pathway activation modeling. Applying this method to clinical data on motor improvement in Parkinson's patients allowed us to evaluate the DBS performance based on fiber recruitment in specific tracts and derive a theoretical 100% improvement pathway activation profile. Furthermore, the role of pathway activation was studied in the context of DBS input to the simulated human basal ganglia-thalamo cortical network. The network architecture was partially inferred from structural connectomes, and it could reproduce normal and PD state electrophysiological data acquired from the literature. As a result of the network optimization, two activation profiles were suggested that theoretically lead to normalization of the neural activity in the ventral anterior thalamus, which receives the basal ganglia output.

Next, the feasibility of reproducing these profiles in rat STN was evaluated. For that, a fiber tractography and a pathway classification had to be conducted using water diffusion data and a digital atlas of the rat brain [45]. Further, an optimization problem for pathway activation had to be solved to determine electrode placements and current amplitudes that led to the closest match with the three optimal profiles. To address field focalization and energy consumption concerns, the problem was solved for two distinctly different electrode configurations and four pulse shapes. Moreover, for both local and pathway activation analyses, OSS-DBS was coupled with an uncertainty quantification software to assess the influence of variation in brain tissue properties and implantation precision on the extent of neural activation.

Based on this work, the following results were obtained, and conclusions could be drawn. According to the volume of tissue activated modeling for rat STN-DBS, the local activation is not limited to the nucleus but could also spread to the adjacent EPN and SNr. Furthermore, for cranial implantations, intended to spare the targeted nucleus, there is a high probability of activation in the dorsal structures when using bipolar electrode configurations. To tackle the latter issue, a novel lead design was suggested [145] that provided a higher focalization of the electric field below the electrode tip. Nevertheless, an activation could not be fully avoided in the EPN and SNr for axon models oriented along the posteroanterior axis of the rat brain. On the other

hand, the sensitivity analysis revealed that the main factor leading to the activation is a misplacement of the electrode along this axis, which could be reduced by improvements in the methodology of stereotactic surgery. It was also demonstrated that DBS could directly activate neurons by depolarizing cell membranes and dendrites. However, the extent of activation and the fidelity was low for a conventional 130 Hz DBS signal, and it was concluded that axonal rather than somatic activation is the primary mechanism of direct neuromodulation in DBS, which is in accordance with previous studies [101].

When analyzing the clinical effects of axonal activation, it could be observed that a balanced recruitment of several pathways rather than activation of particular tracts correlates with a general UPDRS-III score improvement. It is important to remember that STN-DBS affects not only projections of the nucleus, but also passing fibers. Although it is usually discussed in the context of the internal capsule activation, which might produce side-effects, recruitment of other pathways were shown to be beneficial for alleviation of motor symptoms. For example, activation of the cerebellothalamic pathway is associated with tremor improvement [25, 166, 167], and the effect was also reported in this thesis. In [144], it was demonstrated that motor improvement in STN-DBS can be achieved by stimulation of the afferent hyperdirect pathway and the passing pallidothalamic pathway while avoiding a current spread to the internal capsule.

An electrophysiological insight into the mechanism could be gained by modeling DBS effects in the basal ganglia-thalamo-cortical network. In the thesis, one particular aspect was investigated, namely, a thalamic rebounding after pallidal bursting, that had been demonstrated to correlate with PD-like motor symptoms in mice [9]. By optimizing a DBS-induced pathway activation, the pathological rebounding was reversed to a single-spike mode. Curiously, the optimal activation rates were highly dependent on a short-term synaptic depression in the pallidothalamic projections³⁶, and differed considerably from the pathway activation profile derived in the study on clinical effects. When simulating the synaptic depression, a high recruitment of the STN-GPi projections was suggested, which effectively disrupted the abnormal β -band synchronization in the basal ganglia. Furthermore, moderate activation rates were assigned to the hyperdirect and the pallidothalamic pathways. In the network, it could be observed that a high-frequency DBS and the short-term synaptic depression create a γ -band pacing effect in the thalamus, which might facilitate propagation of the physiologically relevant information from the basal ganglia. The effect of the hyperdirect pathway activation has to be further investigated. On the one hand, it could serve as an imbalancing excitatory factor in the abnormally synchronized basal ganglia. At the same

³⁶Though there is an evidence of the synaptic depression [185], it is not yet clearly characterized.

time, high-frequency DBS can create an "informational lesion" that disrupts a pathological high β -activity from the cortex [6].

The central question of this thesis was whether pathway activation profiles, obtained in these two studies, could be reproduced in rat STN-DBS. The results of optimization for the electrode placement and the current amplitude indicated that two out of three profiles could be roughly approximated on the reconstructed pathways.³⁷ Notably, no activation in the cerebellothalamic tract was observed, though it might be partially explained by missing trajectories due to the conservative reconstruction strategy. The uncertainty quantification analysis revealed a non-negligible effect of the variation in the white matter conductivity on the activation rates, especially in the hyperdirect pathway. Therefore, a current adjustment might be required, though one should bear in mind that uncertainties in tissue properties also significantly affect the electric field distribution for the current-controlled mode, unlike uncertainties in the electrode-tissue interface.

It can be concluded that the translatability of pathway activation profiles between human and rat STN-DBS is feasible but limited. Apart from significant differences in the brain anatomy, the primary reason is a simplified electrode design, usually restricted to concentric monopolar or bipolar configurations. Furthermore, rodent DBS electrodes impose a relatively large neurological damage, while implantations cranial to targeted nuclei might lead to a DBS-induced activation in the adjacent structures. In general, precise electrode placement is challenging in rodent surgeries [51], and in Chapter 3 it was shown to be a major factor in the non-targeted stimulation that can compromise the integrity of animal experiments. Nevertheless, the results presented in this thesis suggest that comparable neuromodulatory effects of DBS can be reproduced in the rat basal ganglia, under the stipulation that the listed issues are addressed in the experiment design.

5.1 Outlook

The main methodological contribution of my doctoral studies is the release of OSS-DBS software that encapsulates various aspects of advanced DBS modeling. An important milestone of the development was the integration of OSS-DBS with Lead-DBS, a toolbox for processing medical imaging, which facilitates patient-specific studies. The coupled software was already employed in [144] and in several ongoing studies that investigate fiber recruitment during DBS. A short-term goal for the OSS-DBS team is to show the utility of

³⁷Whether these optimal profiles could be attained in human STN-DBS was not investigated in the thesis. However, it was shown that the profile associated with clinical improvement could be approximated just after several optimization steps.

pathway activation modeling and establish it as a part of the clinical routine for DBS programming, especially since complexity of the latter gradually increases with the growing number of electrode contacts and complex stimulation patterns. If proven successful, the software could be further extended for the use in pre-operative planning, where optimal stimulation sites and parameters will be evaluated based on out-of-sample predictions.

Although OSS-DBS already uses empirically robust discretization and FEM algorithms as well as parallel processing, further improvement of performance is possible and desirable, especially for clinical application. For example, more mathematically sound refinement algorithms should be considered, which could be further accelerated with parallelization using a message passing interface (MPI)³⁸. Furthermore, the utilized FEM formulations could be adjusted to allow explicit modeling of multicontact current-controlled mode and electro-tissue interface.

In the context of rodent DBS, routine application of pathway activation modeling is obstructed. One of the main reasons is a lack of an established pathway atlas. Although diffusion based tractography can delineate major white matter tracts, its accuracy is limited. Moreover, conducting tracts-to-pathways classification based solely on geometrical considerations might lead to a large number of false negatives. The ideal solution would be to adopt best practices of pathway reconstruction in human brain, utilizing histological and structural MRI data, accessed by expert neuroanatomists via a holographic interface as in [123]. Another aspect not addressed in this thesis but crucial for rat STN-DBS translatability is the extent of activation in pathways that are usually not recruited in human brain stimulation, e.g. the medial lemniscus.

In the thesis, it was also shown that uncertainties in brain tissue conductivity have a significant influence on pathway activation. The nature of these uncertainties is rather epistemic than aleatoric, and they partly occur due to the lack of a unified methodology for conductivity measurements. In animal research, invasive *in vivo* approaches could be employed, for example, the method proposed in [60]. It should be noted that if the specified conductivities significantly differ from the probability density functions considered in Chapter 4, then the optimization of electrode placement and current amplitude will have to be repeated. Another factor of uncertainty is the electrode-tissue interface. Although the current-controlled mode, usually used in rodent DBS, effectively compensates for the interface impedance, it is still important to gain a better understanding of the interface effects, and especially the electrical double layer. This is of concern considering higher impedances and the nonlinear regime at high overpotentials, where irreversible faradaic reactions might occur.

³⁸Although an MPI version of mesh refinement was implemented in OSS-DBS using FEniCS routines, it was not stable when a large number of cores was drawn.

Nevertheless, these hurdles are surmountable, and the further advance in computational modeling for animal DBS research is inevitable. Its primary task is to facilitate thorough planning of experiments necessitated by strict regulations of animal welfare. For instance, modeling can provide an insight into stimulation targets and protocols that are the most efficient for hypothesis testing. Such a study was conducted in this thesis for suppression of pathological thalamic rebounding, which was achieved by optogenetics in mice [9], but has not yet been tested in rodent DBS. Furthermore, the incorporation of multimodal electrophysiological recordings into the computational model allows to analyze systematically complex network effects, which is of a great interest for network disorders such as PD. For example, the model can be employed to investigate the inefficiency of EPN stimulation in contrast to GPi [217], which in turn could expand our understanding of the DBS mechanism. Computational modeling could also drive the development of novel stimulation setups, e.g. using microelectrode arrays for pilot studies on a targeted pathway activation and a coordinated reset approach.

Appendix A

Appendix

A.1 Mesh refinement

This section is a part of the OSS-DBS publication [140] and it describes the implemented mesh refinement routines.

As was previously mentioned, the convergence of the solution on neuron model compartments is the criterion for mesh adaptation. The adaptation is carried out in two steps. At first, the algorithm evaluates the effect of CSF refinement on the pointwise solution for the magnitude of the electric potential, represented by φ_{aim} . CSF is 10–20 times more conductive than grey and white matter, and therefore the accurate mapping of CSF space is crucial. The adaptive algorithm starts by refining all cells that contain CSF voxels and reside in the vicinity of the deployed neuron models until the cells do not exceed a certain size, e.g. MRI voxel dimensions. Next, φ_{aim} is computed on the obtained mesh. The CSF refinement trigger criterion is defined as

$$\left\| \frac{\varphi_{\text{aim}} - \varphi_k}{V_{\text{drop}}} \right\|_{\infty} > \Theta_{\text{CSF}}, \quad (\text{A.1})$$

where φ_k is the solution in the k -th refinement iteration, V_{drop} is the magnitude of the voltage drop across the tissue, and Θ_{CSF} is the deviation threshold for the electric potential on the neuron compartments during CSF refinement. The zero iteration corresponds to the initial mesh and the subsequent iterations have descending cell size for CSF voxels.

In the second step, the refinement is carried out in the three brain regions separately (the region of interest, rest of the tissue and the vicinity of contacts) in order to reduce the computational effort. Firstly, a submesh is refined

uniformly and φ_{new} is computed. The trigger criterion for adaptive refinement is

$$\left\| \frac{\varphi_{\text{new}} - \varphi_{\text{old}}}{V_{\text{drop}}} \right\|_{\infty} > \Theta_{\varphi}, \quad (\text{A.2})$$

where Θ_{φ} is the deviation threshold during adaptive refinement. If Criterion A.2 is not fulfilled, the algorithm refines cells in the subdomain on the initial mesh, where the change of the solution for the electric field \underline{E} is above the relative field deviation threshold Θ_E

$$\frac{\left\| \underline{E}_{\text{new}} - \underline{E}_{\text{old}} \right\|_2}{\left\| \underline{E}_{\text{new}} \right\|_2} > \Theta_E, \quad (\text{A.3})$$

computes φ_{new} and checks Criterion A.2 again. Further refinement will be conducted on the mesh from the preceding iteration. If the required convergence is achieved, the adapted region will be tested again with a uniform refinement to avoid the local convergence effect. Note that the trigger criteria are evaluated on the compartments of the neuron models when the meshes are compared qualitatively. However, to locate cells with a poor convergence, Criterion A.3 is estimated on midpoints of cells in the region.

The current-controlled mode requires an additional evaluation of a current convergence criterion. The criterion is based on the change of currents integrated over mesh interfaces of electrode contacts. If the change due to refinement exceeds a prescribed threshold, the refinement algorithm looks for cells where

$$\frac{\sum_{i=1}^n \left(\iiint_{\text{cell}} |\underline{\mathbf{J}}(\mathbf{r})| d\Omega_i \right) - \iiint_{\text{Cell}} |\underline{\mathbf{J}}(\mathbf{r})| d\Omega}{\sum_{i=1}^n \iiint_{\text{cell}} |\underline{\mathbf{J}}(\mathbf{r})| d\Omega_i} > \Theta_{\mathbf{J}}, \quad (\text{A.4})$$

Here $\underline{\mathbf{J}}(\mathbf{r})$ is the complex current, *Cell* refers to the cell in the initial mesh, n is the number of *cells* that comprise *Cell* in the refined mesh and $\Theta_{\mathbf{J}}$ is the relative deviation threshold for the current. This condition will not be evaluated in the cells with small currents as their refinement will not influence the solution. It is important to note that the current is not dependent on the potential itself, but its spatial derivative. Therefore, in order to ensure a non-constant gradient over a cell, the platform employs at least the second order basis functions for the evaluation of the electric potential.

A.2 Modeling of human STN-DBS

This section lists settings that were used in the study on pathway activation and its correlation with UPDRS-III score improvement [144]. For further details on the retrospectively recruited cohorts, please refer to the publication.

Table A.1: *Simulation settings.*

Electrode type:	Boston Scientific Vercise (Cartesia)
DBS pulse type:	rectangular (low amplitude charge-balancing)
DBS pulse width:	20–60 μs
DBS repetition rate:	79–185 Hz
DBS mode:	multipolar current-controlled
Simulation coordinates:	native (patient-specific)
Computational domain:	80 mm spherical approximation around target
Brain heterogeneity:	segmentation of MRI preoperative T1
Brain anisotropy:	co-registered diffusion atlas [67]
Fiber trajectories:	co-registered pathway atlas [123]
Brain dispersiveness:	according to [58] with a correction from [59]
Laplace’s formulation:	quasistatic (Eq. 2.14)
Solver:	GMRES [139]
Spectrum truncation:	octave band method [61]
Mesh refinement:	disabled (manually pre-refined)
FEM element order:	3rd
Thickness of encapsulation:	0.1 mm
Encapsulation conductivity:	same as white matter
Constant phase element:	disabled (current-controlled mode)

List of Acronyms

Brain structures

AA	Amygdalar area
CC	Corpus callosum
Cbf	Cerebellar fibers
CbP	Cerebellar peduncles
EPN	Entopeduncular nucleus
GPe	External globus pallidus
GPI	Internal globus pallidus
HDP	Hyperdirect pathway
HI	Hippocampal formation
HY	Hypothalamus
IC	Internal capsule
M1	Primary motor and premotor cortex
M1/M2 (rat brain)	Sensorimotor regions of cortex
MC	Primary motor cortex
ML	Medial lemniscus
MMT	Mammillothalamic tract
MRN	Midbrain reticular nucleus
Opt	Optic tract
PMC	Premotor motor cortex
RN	Red nucleus
RT	Reticular nucleus
SMA	Supplementary motor area
SN	Substantia nigra
SNr	Substantia nigra pars reticulata
STN	Subthalamic nucleus

TH (Th)	Thalamus
VA(/VL)	Ventral anterior (lateral) nuclei of thalamus
VL	Lateral ventricle
VPL	Ventral posterolateral nucleus
VPM	Ventral posteromedial nucleus
ZI	Zona incerta

Other abbreviations

2-D	Two Dimensional
3-D	Three Dimensional
6-OHDA	6-hydroxydopamine
AP	Action Potential
CAD	Computer-Aided Design
CPE	Constant Phase Element
CSF	cerebrospinal fluid
CT	Computed Tomography
DBS	Deep Brain Stimulation
DTI	Diffusion Tensor Imaging
DWI	Diffusion-Weighted Imaging
ECoG	electrocorticography
EDL	Electrical Double Layer
EEG	electroencephalography
EMG	electromyography
EQS	electro-quasistatic formulation of <i>Maxwell's equations</i>
FEM	Finite Element Method
FFEM	Fourier Finite Element Method
FGATIR	Fast Gray matter Acquisition T1 Inversion Recovery
fMRI	functional Magnetic Resonance Imaging
GABA	gamma-aminobutyric acid
HARDI	High Angular Resolution Diffusion Imaging
IIT	Illinois Institute of Technology
LFP	Local Field Potential
MDF	Modified Driving Force
MEG	magnetoencephalography

MNI	Montreal Neurological Institute
MPTP	1-methyl-4-phenyl-1,2,3,6-tetrahydropyridine
MRI	Magnetic Resonance Imaging
PAM	Pathway Activation Modeling
PD	Parkinson's Disease
QS	quasistatic formulation of <i>Maxwell's equations</i>
STD	short-term synaptic depression
UPDRS(-III)	Unified Parkinson's Disease Rating Scale (motor score)
VTA	Volume of Tissue Activated

List of Symbols

Symbol	Description
\mathbf{A}	Magnetic vector potential
\mathcal{A}	Profile of activation rates
\mathcal{A}	Activation rate
$\tilde{\mathcal{A}}$	Approximated activation rate
\mathbf{B}	Magnetic flux density
b	parameters of diffusivity measurement
C_M	Membrane capacitance
Cl^-	Chloride ion
c_i	Expansion coefficient in surrogate polynomial expansion
\mathbf{D}	Diffusion tensor
\mathbf{D}	Electric flux density
d_e	Coefficient of microscopic extracellular diffusivity
d_i	Coefficient of microscopic intracellular diffusivity
\mathbf{E}	Electric field strength
E	Shifted Nernst equilibrium potential
\mathbb{E}	Expected (mean) value
f	Frequency
\mathbf{f}	Vector of coefficients in FEM problem
f_j	Unknown coefficient in FEM problem
f_{goal}	Goal function in optimization problem
G	Conductance (in neuron model)
g	Time and voltage dependent conductance of ion channel
\mathbf{H}	Magnetic field strength
I_m	Total membrane current

Symbol	Description
j	Imaginary unit
\mathbf{J}	Current density
J_{el}	Integral of current over FEM element
K	Scaling factor of constant phase element
K	Potassium
\mathbf{L}	Arbitrary differential operator
\mathbf{M}	Magnetization field
N_{comp}	Total number of computations at collocation points
N_p	Number of expansion factors
Na	Sodium
\mathbf{P}	Polarization field
$P_{5,95}$	5th and 95th percentiles
p	Polynomial order
p	Probability of true null hypothesis
\mathbf{Q}	Vector of uncertain parameters
Q	Uncertain parameter
R_{CT}	Charge transfer
R_{max}	Largest brain dimension
\Re	Real part of complex number
r	Residual
r	Pearson's correlation coefficient
r_a	axial resistance per unit area
r_{encap}	thickness of encapsulation layer
\mathbf{r}	Position vector
\mathbf{r}	Unit vector in direction of magnetic field gradient
s	Source in FEM problem
\mathbf{S}	Stiffness matrix
S	Measured diffusion-weighted signal
S_0	Signal measured in absence of magnetic gradients
S_{encap}	Scaling factor of encapsulation layer conductivity
S_Q	First order Sobol' index for parameter Q
t	Time
V_D	Matrix composed of eigenvectors of diffusion tensor

Symbol	Description
V_e	Extracellular potential
V_m, V_{mem}	Membrane potential
V_i	Intracellular potential
V_r	Resting potential
\mathbb{V}	Variance
w_j	Weighting function in FEM problem
w_i	Weighting factor in Canberra distance
Z_{CPE}	Impedance of constant phase element
α	Balancing parameter
α -dispersion	Dispersion in dielectric properties below 1 kHz
β	Capacitive contribution in constant phase element
β -band	13–30 Hz (neural oscillation)
Δ	Difference operator
Γ	Boundary of computational domain
γ -band	30–100 Hz (neural oscillation)
ε	Absolute permittivity of material
ε_0	Vacuum permittivity
ε_r	Relative permittivity of material
η	Weighting factor in modified driving force
$\underline{\kappa}$	Complex conductivity
$\mathbf{\Lambda}_{\text{scaled}}$	Diagonal matrix of scaled eigenvalues of diffusion tensor
λ	Eigenvalues of diffusion tensor
μ_0	Vacuum permeability
μ_r	Relative permeability of material
ξ_i	Polynomial in surrogate polynomial expansion
ω	Angular frequency
Ω	Computational domain
π	Mathematical constant
$\mathbf{\Sigma}$	Voxel-wise conductivity tensor
σ	Electrical conductivity of material
σ_e	Microscopic extracellular conductivity
σ_{iso}	Isotropic conductivity of material
ϕ	Phase angle

Symbol	Description
φ	Electric potential
ψ_i	Basis function in FEM problem
∇	Nabla-Operator
$\frac{\partial}{\partial t}$	Time derivative
$\frac{\partial^2}{\partial x^2}$	Second order 1-D spatial derivative
$\frac{\partial}{\partial \mathbf{r}}$	3-D spatial derivative
$ \cdot $	L1-norm
$ \cdot _2$	L2-norm

List of Figures

- 1.1 Coronal and sagittal view of the selected structures of the basal ganglia visualized using a high resolution and subcortical atlases [10, 11] of the human brain in Lead-DBS [12] (STN – subthalamic nucleus, GPe and GPi – external and internal segments of the globus pallidus, respectively). 2
- 1.2 Circuit diagram of the human brain basal ganglia-thalamo-cortical activity in the healthy (left) and the parkinsonian (right) states. Red and blue colors correspond to inhibitory and excitatory projections, respectively, and the intensity reflects the activity level. Brain structures are visualized using a subcortical atlas [11] in Lead-DBS (GPe and GPi – external and internal segments of the globus pallidus, respectively, Th(VA) – ventral anterior nucleus of the thalamus, STN – subthalamic nucleus, SN – substantia nigra, MC/PMC – primary motor and premotor cortical regions, SMA – supplementary motor area, D1/D2 – dopamine receptors). The distinctive trait of the parkinsonian state is the imbalanced striatal output that leads to higher activity in the GPi, SN and STN. The reciprocal coupling of the latter with the GPe (white dash-line) is a probable source of the abnormal oscillatory activity [1]. 3
- 1.3 Circuit diagram of the human brain basal ganglia-thalamo-cortical activity during DBS in the STN (left) and the GPi (right). Red and blue colors correspond to inhibitory and excitatory projections, respectively, and the intensity reflects the activity level. Dotted lines show projections that are likely to be directly stimulated by the DBS-induced electric field. The stimulation extent of the hyperdirect pathway by DBS-GPi and the pallidothalamic projection by STN-DBS (dash-lines) is limited due to the relative remoteness. Note that stimulations lead to a modulation of the basal ganglia output to the thalamus. . . 6

1.4	Pathways relevant for STN-DBS, reconstructed in the rat brain using a water diffusion imaging data from [45]. The brain structures are visualized using a rat brain atlas [45] (GPe – external segment of the dorsal pallidum, EPN – entopeduncular nucleus (analogue of the GPi in rodents), Th(VA/VL) – ventral anterior and ventral lateral nuclei of the thalamus, STN – subthalamic nucleus, M1/M2 here are the sensorimotor regions of the cortex). The central question of the thesis is whether DBS-induced activation patterns in the hyperdirect (blue), the cerebellothalamic (green) and the pallidothalamic pathways (red) are comparable in human and rat from the modeling perspective.	9
1.5	Schematic depiction of a DBS setup in rats. 1 – DBS electrode, 2 – cables to connect to the pulse generator, 3 – grounding gold wire (note that it is placed outside of the skull), 4 – acrylic mounting, 5 – fixating screw that can be used for grounding. The image is adapted from [47].	10
2.1	Rectangular DBS signals with different repetition rates (left, note the time lapse) and the magnitude of their power spectra (right). The contribution of individual frequency components is important in the context of dispersive dielectric properties of brain tissue.	13
2.2	Alternative triangular DBS signals with a 130 <i>Hz</i> repetition rate (left) and the magnitude of their power spectra (right). Note that the signal depicted in orange is cropped due to the inappropriately large time step.	13
2.3	Two types of charge balancing for a 130 <i>Hz</i> DBS signal (left) and the magnitude of their power spectra (right). Note the shift to higher frequencies for the biphasic symmetric pulse. The left plot also illustrates the ratio of the pulse width to the signal period.	16
2.4	Dielectric properties of the main brain tissue types in the frequency domain. The dispersive values were taken from Gabriel et al [58], but adjusted by omitting the α -dispersion as proposed in [59] and additionally upscaled to match the grey and white matter electrical conductivities at 50 <i>kHz</i> , computed as the mean of the values reported in [58] and [60]. Left: electrical conductivity of the tissue (CSF conductivity is not dispersive and ≈ 2 <i>S/m</i>) and the magnitude of the power spectrum for the 130 <i>Hz</i> DBS signal (shown in teal on the background). Right: relative contribution of the capacitive term in the <i>Laplace's equation</i> depending on the brain tissue. Note that the omission of the α -dispersion significantly reduces the capacitive contribution at low frequencies.	16

2.5	Tissue-voltage response for different DBS power spectrum approximation methods [61] when solving the electroquasistatic formulation of <i>Maxwell's equations</i> . Here, the cutoff method picks the first 500 frequencies in the spectrum, while the high amplitude method picks 500 frequencies with the largest contribution. The octave bands deployed over the power spectrum starting from 1040 Hz are shown on the right (orange dash). The idea is to compute the field distribution only for one frequency in the band and extrapolate on the rest. Evidently, the octave band method is more efficient and accurate approximation. Note the voltage growth over the pulse due to the capacitive charging.	17
2.6	Three formulations for modeling the DBS-induced field in brain tissue. Left: tissue-voltage response during the constant current stimulation solved for the dielectric properties of grey matter [58]. The electro-quasistatic formulation clearly demonstrates a capacitive charging effect, while the stationary model, where dispersion is neglected, shows a lower tissue resistance (the conductivity is assessed at the median frequency of the power spectrum of 130 Hz 60 μs rectangular signal). Insignificant rippling occurs due to the truncation of the spectrum. Right: equivalent circuits of the formulations. The image is taken from the author's book chapter [64] with a permission of the publisher.	18
2.7	Example of medical imaging data required for a detailed volume conductor model. Left: T1-weighted (longitudinal relaxation time) MRI sequence allows to clearly visualize myelinated tissue (white matter) as high intensity regions, while CSF appears dark. Center: a segmentation of the brain tissue with distinctly different electrical conductivities. Right: the distribution of the anisotropic tissue, visualized using the IIT human brain atlas [67]. The intensity corresponds to the magnitude of the voxel-wise normalized water diffusion tensor data. Here, the anisotropy is especially prominent in the corpus callosum (CC) and the internal capsule (IC), which passes in the vicinity of the STN.	19

2.8	Effect of complexity of a volume conductor model. Note that for DBS modeling, a brain geometry can be usually approximated with an elliptic or spherical domain. Left: a segmentation of brain tissue mapped onto an FEM mesh. Grey and white matter are depicted in the corresponding colors, CSF in blue, encapsulation layer (scar tissue formation) in red and the highly conductive electrode contacts in orange (the rest of the electrode is assumed to be insulated and removed from the volume conductor model). A precise mapping in the whole domain is often not required, especially for bipolar stimulations, where the current path is confined to the vicinity of the electrode contacts. Center and right: the distribution of the electric field magnitude (log scale) in homogeneous isotropic and heterogeneous anisotropic volume conductor models, respectively.	19
2.9	An example of elliptic representation of conductivity tensors in the vicinity of the STN obtained using [75] and [74] scaling methods, respectively. Note that the former yields a higher anisotropy (see the colorbars). The image is taken from the author's book chapter [64] with a permission of the publisher.	21
2.10	Phases of encapsulation layer around an implanted electrode (not a realistic scale). Left: the acute phase is characterized by a microglial activation and degeneration of neurons. The electrode surface is covered by blood and cerebrospinal fluid. Right: in the chronic phase, the electrode is encapsulated by glial scarring formed by reactive astrocytes, while the neuron density is decreased.	23
2.11	Electrode–tissue interface. Top left: the equivalent circuit of the interface for monopolar stimulation with highlighted dominating elements. Top right: a depiction of the electrical double layer and the charge transfer on the metal–electrolyte interface due to an electron-ion interaction. Bottom: the interface components on a DBS electrode. Note that the interface also occurs on inactive contacts that are sometimes used for measurements. The image is adapted from the author's book chapter [64] with a permission of the publisher.	24
2.12	Action potential initiation in response to a current injection. The resting potential (here ≈ -60 mV) is a relatively constant membrane potential that originates from differences in membrane permeabilities of ions.	27
2.13	Electron microscopy of myelinated axons. Left: nodes of Ranvier are located at the gaps of myelination. Right: a cross-section of a myelinated axon. The images are taken from [102].	28

2.14	McNeal's circuit representation of a myelinated axon [104] composed of three components: the ideally insulating myelin sheath (violet), the nodes of Ranvier (orange) and the axon itself. The conductances and capacitances are marked with the corresponding subscripts, where the nodal conductance $G_n = (I_K + I_{Na} + I_L)/V_m$. V_{rest} and V_e denote the resting and the extracellular potentials. Note that in McNeal's model, the nodal parameters correspond to the membrane parameters in Eq. 2.21.	29
2.15	Artistic sketch (top) and circuit representation (bottom) of a mammalian myelinated axon composed of five components: the myelin sheath (violet), the periaxonal space (green), the internodal axolemmas, the nodes of Ranvier (orange) and the axon itself. The conductances and capacitances are marked with the corresponding subscripts. V_{rest} and V_e denote the resting and the extracellular potentials. The voltage-gated ion channels at the nodes of Ranvier include slow potassium K_{slow} , fast and persistent sodium channels Na_{fast} and Na_{pers} in parallel to a non-specific leakage. The image is taken from the author's book chapter [64] with a permission of the publisher.	31
2.16	Activation extent of a monopolar stimulation computed with different volume conductor models. From left to right: activation contours for coronal, sagittal and axial planes, respectively. Volume conductor models from top to bottom: homogeneous isotropic, heterogeneous, heterogeneous and anisotropic (diffusion tensors were normalized using the volume conservation method). Note that the homogeneous isotropic model returns a cylindrically symmetric activation contour. The image is adapted from the author's book chapter [64] with a permission of the publisher.	32
2.17	Modeling the effect of bipolar DBS on the extent of neural recruitment in the pallidothalamic and corticofugal fibers with $ \mathbf{E} _2$ -based approximation of volume of tissue activated (VTA) and pathway activation modeling. The active electrode contacts are highlighted. Marked in red are the fibers predicted to be activated by the pathway activation modeling. Note that for the corticofugal pathway, the VTA approximation overlaps mostly with the red fibers, which is not the case for the pallidothalamic tract that swirls around the electrode. Fiber trajectories are taken from [123].	34
2.18	Lagrange basis functions of different order.	37
2.19	Solvers' performance for the quasistatic formulation of <i>Maxwell's equations</i> (Eq. 2.14) depending on the degrees of freedom and refinement type. Solid lines show the results for the p -refinement, dashed for the h -refinement.	40

2.20	An example of mesh refinement based on the electric field convergence. Left: the distribution of the electric field magnitude (log scale) on the electrode surface and FEM elements marked for a subsequent refinement. Note the high magnitude at the edges of the active contacts and the low magnitude (blue area) at the floating contact. Right: wire view of the meshed surface after all refinement steps are completed. Note the fine discretization at the edges of the contacts and a part of the upper active contact.	42
2.21	Workflow of OSS-DBS. Input data are provided either directly or after Lead-DBS processing that facilitates patient-specific studies. OSS-DBS computations are encapsulated in a Docker container that can be deployed on all major operating systems. .	43
2.22	Workflow for uncertainty quantification using the generalized polynomial chaos implemented in UncertainPy. For uncertain parameters \mathbf{Q} , the user provides estimated probability density functions for which UncertainPy selects an appropriate polynomial expansion to approximate the neural activation $\tilde{\mathcal{A}}(\mathbf{Q})$. Coefficients of the polynomials are computed by solving the original computational model in OSS-DBS for parameters \mathbf{Q}_c defined by the collocation method with Hammersley sampling. Statistical metrics and Sobol' indices S_{Q_1}, S_{Q_2} are either estimated directly from the polynomial expansion or by solving the computationally inexpensive surrogate model using a Monte Carlo sampling.	45
3.1	Direct local activation induced by rat STN-DBS. Top left: the geometry of the STN projection neuron [113] in comparison to the STN (in orange) and the stimulating tip of the bipolar electrode SNEX-100 with a 50 μm encapsulation layer (in red). Top center and right: only cells marked in red respond with an action potential to five DBS pulses (see Fig. 3.3). Bottom: VTA contours in coronal, sagittal and axial planes, respectively. Blue voxels correspond to the axons considered damaged by the implanted electrode. Note the wide extent of activation for axons oriented parallel to the electrode.	47

3.2	Volume conductor model for rat STN-DBS. A: the distribution of grey and white matter, depicted with the corresponding colors, as well as CSF (blue) and the encapsulation layer (red). The STN is shown in orange. The electrode is assumed to be highly conductive and removed from the model, preserving the appropriate boundary conditions. The large computational domain is shown here for visualization purposes, but can be significantly truncated for the bipolar stimulation. B: the elliptic representation of conductivity tensors obtained based on water diffusion data [45] and scaled using the volume conservation method [75]. C: the electric potential distribution in the vicinity of the electrode contacts. Due to the linearity of Eq. 2.14, the solution can be scaled to compute activation for different amplitudes.	48
3.3	Response of an isolated STN projection neuron (without an axon, see Fig. 3.1, top left) to the DBS-induced extracellular field modulation. Note that the anodic stimulation (locally hyperpolarizes the neural membrane) postpones but does not suppress the endogenous firing, while the cathodic stimulation (locally depolarizing) provokes an action potential initiation, but with a low fidelity.	49
3.4	Activation in the STN and adjacent EPN and SNr for a cranial implantation (0.4 mm above the STN). A: VTA grids over the brain structures. B: $ \mathbf{E} _2$ -based VTA approximation ($> 0.323 V/m$ in red, $> 0.2 V/m$ in yellow). Evidently, most of the activated tissue is outside of the target. C: statistical metrics for the VTA arrays (STD – standard deviation, P_5 and P_{95} are the 5th and the 95th percentile, respectively). D: the first order Sobol’ indices for the VTA arrays. The precision of the electrode implantation is found to be the dominant factor, especially for the non-targeted nuclei.	50
3.5	Assumed probability density functions for the thickness of the encapsulation layer (A), its conductivity scaling (B), and the deviation from the implantation site along the posteroanterior axis of the rat brain (C).	51
3.6	VTA contours in coronal (left) and sagittal (right) planes computed for the precise cranial implantation (red – activated axon, blue – excluded due to the intersection with the electrode or CSF). Activation in the SNr occurs due to the membrane polarization on the axons oriented towards the STN.	51

3.7	Activation in the STN and adjacent EPN and SNr for a cranial implantation of a custom electrode with the blunt tip design. A: schematics of the custom electrodes (adapted from [145]). B: $ \mathbf{E} _2$ -based VTA approximation ($> 0.323 \text{ V/m}$ in red, $> 0.2 \text{ V/m}$ in yellow). C: statistical metrics for the VTA arrays (STD – standard deviation, P_5 and P_{95} are the 5th and the 95th percentile, respectively). Note the higher overall activation than for the SNEX-100 electrode. D: the first order Sobol’ indices for the VTA arrays. Again, the precision of the electrode implantation is found to be the dominant factor, but in this case the radius of the encapsulation has a prominent effect on the VTA in the STN.	52
3.8	Field focalization for the cranial implantation (coronal view). Left: brain structures above the STN, which are likely to be affected by the implantation (ZI – zona incerta, Th – thalamus, HY – hypothalamus, VPM – ventral posteromedial nucleus). The rest: VTA contours for SNEX-100 and the custom electrodes (blunt tip and spherical rounding), respectively. Note the difference in the extent of tissue affected by the implantation (marked in blue).	53
4.1	Circuit diagram of the basal ganglia pathways in the normal (left) and the parkinsonian (right) states. Line weights reflect the activity levels of the pathways. The parkinsonian state is characterized by a loss of dopaminergic cells in the substantia nigra (SN) that produces an imbalance in the striatum. In turn, it leads to a bursting activity in the basal ganglia output, which can induce rebounding in the ventral anterior nuclei of the thalamus (VA). STN – subthalamic nucleus, GPi and GPe – internal and external regions of the globus pallidus, respectively, MC and PMC are the motor and premotor cortical regions, SMA – supplementary motor area, D1/D2 – dopamine receptors. Note that in the human brain, the pallidosubthalamic pathway consists of two tracts: ansa lenticularis and lenticular fasciculus.	56
4.2	Some passing and local projections potentially affected by STN-DBS. The pathways are taken from [123] and visualized in Lead-DBS. The chosen electrode placement (inside the motor aspect of the STN) is efficient for motor symptom alleviation in Parkinson’s disease. Note that the electrode passes through the subthalamopallidal pathways, potentially leading to a significant neurological damage or neuron migration.	57

4.3	Dataflow for pathway activation modeling in the patient-specific space. Based on patient imaging and brain atlases, Lead-DBS (orange box) reconstructs the electrode position and provides a description of tissue and water diffusion distributions in the brain. These data are used by OSS-DBS (green box) to create an accurate patient-specific volume conductor model. The model is then employed to compute the electric potential distribution in space and time along axon models allocated on the trajectories described by a pathway atlas. Finally, for the given distribution, the cable equation is solved to probe the axonal activation, i.e. the occurrence of an action potential in response to DBS. The image is taken from [144].	59
4.4	Violin plots of pathway activation rates across both cohorts. M1 and PMC refer to the primary and premotor cortical regions, SMA – supplementary motor area; cf and hdp are the corticofugal and the hyperdirect pathways, respectively; Ansa – ansa lenticularis, Lent – lenticular fasciculus, CbTh – cerebellothalamic pathway; l, f, up - lower extremity, face-neck region, and upper extremity in the primary motor cortex. The cohorts' datapoints provide a wide coverage of the pathway activation space. Noteworthy is the nearly zero activation across both cohorts in the corticofugal branch descending from the region of the lower extremity in the primary motor cortex. The image is adapted from [144].	60
4.5	Left: an example of a target profile derivation from two DBS protocols in a 2-D pathway activation space. Values of P_i denote the corresponding UPDRS-III scores for patient i , "+" and "-" subscripts refer to the more and less effective stimulation protocols, respectively. Note that in our problem the pathway activation space had 16 dimensions. Right: the intrapatient in-teprotocol UPDRS-III improvement in the training cohort with and without the normalization by the mean of activation rate differences. The highlighted datapoints were used to derive $\mathcal{A}_{\text{target}}$	61
4.6	Key pathways in the target profile, which activation rates were decisive for UPDRS-III improvement. The box plot on the right shows the optimized weighting factors of the Canberra distance computed with the 'leave-one-out' approach in the training cohort. Note the low number of outliers. The contribution of the cerebellothalamic pathway was not significant in the target profile, but its activation correlated with interprotocol UPDRS-III improvement. The image is adapted from [144].	62

4.7	Correlation of UPDRS-III improvement in the training (left) and the test (right) cohorts with the weighted Canberra distance (defined in the pathway activation space) to the target profile derived based on three patients with the highest normalized interprotocol UPDRS-III improvement. Colored lines between the datapoints highlight the interprotocol binary correlation in the training cohort (green – valid prediction, black – false). The image is adapted from [144].	63
4.8	An example of electrode placement in the STN (MNI space) with a low weighted Canberra distance to the target profile (defined in the pathway activation space). A half of the lenticular fasciculus was considered "damaged" by the implantation (intersected with the electrode or the 0.1 mm encapsulation layer around it), while the rest were recruited by the DBS. Note that no activation was computed for the cerebellothalamic pathway.	64
4.9	Effect of activation in the cerebellothalamic pathway on tremor alleviation in the training cohort. Left: no correlation was observed between activation rates and tremor improvement from baseline. Right: the interprotocol difference in activation rates correlated with the corresponding difference in the tremor scores. The image is taken from [144].	65
4.10	Raster plot of a simulated motor cortical activity in the resting state. Oscillatory patterns were modeled with a broad normal distribution centered at 18 Hz. In the PD affected network, the firing in the β -band is increased (see Fig. 4.12), though it cannot be directly observed in the raster plot.	68
4.11	Simulated single unit activity in the ventral anterior thalamus shown for two representative neurons. Left: a regular single-spike mode in the normal state. Right: in the PD state, rebounding occurs in response to the bursting inhibition via the pallidothalamic pathway.	68
4.12	Normalized power spectra of the simulated mean activity in the normal (left) and PD-affected (right) network. Note that the β -activity was present in the basal ganglia in both states, but became more prominent in PD due to the abnormal synchronization. Low levels of artificial noise in the simulated basal ganglia nuclei eliminated the $1/f$ trend at the low frequencies.	69

4.13	Modeling network effects of DBS for normalization of the ventral anterior thalamic firing. Left: optimized activation rates induced by DBS without a short-term synaptic depression of GABAergic synapses of pallidothalamic neurons. Center: the same with the synaptic depression. Note that in both cases the subthalamopallidal pathways had a large difference in the optimized activation that cannot be achieved with conventional DBS electrodes. Right: normalized power spectra of the simulated mean activity of VA-thalamic neurons in four network states. For both DBS-on cases, normalization of the VA-thalamic firing was achieved by elimination of rebounding bursts, but the mechanism was distinctly different (see Fig. 4.14).	69
4.14	Simulated single unit activity of two representative neurons in the ventral anterior thalamus under STN-DBS. Left: without the short-term synaptic depression in the pallidothalamic projections, the stimulation quenched activity in the receiving neurons. Right: when the synaptic depression was modeled, the neurons were regularly released from the DBS-induced inhibition, leading to a regular single-spike activity in the γ -band.	70
4.15	Coronal and sagittal views of brain structures relevant in STN-DBS, visualized in a rat brain atlas [45]. M1/M2 – somatomotor areas, EC and IC – external and internal capsule, respectively, GPe – external segment of the globus pallidus. A delineation of the ventroanterior/ventrolateral nuclei of the thalamus (VA/VL) and the entopeduncular nucleus (EPN, an analogue of the GPi in rodents) was conducted manually following [79].	73
4.16	Coronal view of the non-diffusion-weighted sequence S_0 in the masked and truncated HARDI data from [45]. The highlighted region in the corpus callosum (CC) is used below to visualize different diffusivity metrics.	74
4.17	Different representations of the voxel-wise defined diffusivity: tensor ellipsoids (left) and orientation distribution functions using the constant solid angle and the constrained spherical deconvolution methods, respectively. Note that all three methods would be suitable for a reconstruction of the corpus callosum fibers.	75

4.18	Workflow of the pathway reconstruction for the hyperdirect and the corticofugal pathways. First, tracts are seeded in the internal capsule and have to propagate to the somatomotor area of the cortex. Second, fibers that pass far from the STN are automatically removed. The rest are grouped depending on whether they terminate in the vicinity of the nucleus. If not, the fibers should merge with the cerebral peduncle or they are discarded otherwise. Finally, a manual evaluation is conducted, which removes outliers and non-physical trajectories; in this case these were the fibers trespassing the external capsule. The fibers remaining in the two groups are considered the hyperdirect (blue) and the corticofugal (orange) pathways.	75
4.19	Reconstruction of the cerebellothalamic (left) and pallidothalamic (right) pathways. For the former, more lateral trajectories could be expected. Note the C-shaped trajectory of the pallidothalamic pathway, which is in accordance to [205]. Cbf – cerebellar fibers, RN – red nucleus.	76
4.20	Alternative approaches to fiber tractography considered in the thesis. Left: an anatomically constrained tractography using the constrained spherical deconvolution. Center: the constant solid angle method with a thresholding by generalized fractional anisotropy. Right: a probabilistic sampling of the orientation distribution function. The tensor-based tractography generated more physiologically plausible trajectories (see Fig. 4.18) possibly due to insensitivity to secondary diffusion directions.	77
4.21	Allocation of axon models on the classified pathway trajectories. The models are comprised of compartments that are depicted as separate points. Note that compartments far from the STN are not affected by the extracellular stimulation and are truncated in order to reduce the computational costs.	80

4.22	Optimizing rat STN-DBS to match the optimal profile that was predictive for clinical motor improvement. Left column: optimized placement of the electrodes for various pulses in the coronal, sagittal and axial planes of the rat brain atlas [45], respectively. The planes are shown at the optimal position of SNEX-100 (rectangular pulse), where the STN is not entirely visible (its center of mass is marked in red, and the 1 <i>mm</i> vicinity is highlighted). For abbreviations see Table 4.2. Right column: the goal function (the Canberra distance to the optimal profile) visualized in the same planes (with ± 0.1 <i>mm</i> aggregation along the transversal axis) for the stimulation with the rectangular pulse using SNEX-100. The results indicate that the anterior lateral electrode placement relative to the STN is the most effective for matching the pathway activation profile suggested in [144].	81
4.23	Optimizing placement of the electrodes for rat STN-DBS to match the optimal profile that led to normalization of the neural activity in the ventral anterior nucleus simulated in the basal ganglia-thalamo-cortical network (without the short-term synaptic depression of pallidothalamic neurons). The goal function on the right is shown for SNEX-100, conventional rectangular pulse. The results indicate that the anterior lateral electrode placement of relative to the STN is the most effective for the normalization. For abbreviations see Table 4.2.	82
4.24	Optimizing placement of the electrodes for rat STN-DBS to match the optimal profile that led to normalization of the neural activity in the ventral anterior nucleus simulated in the basal ganglia-thalamo-cortical network (with the short-term synaptic depression of pallidothalamic neurons). The goal function on the right is shown for SNEX-100, conventional rectangular pulse. The results indicate that the anterior lateral electrode placement relative to the STN is the most effective for the normalization. Note that different positions along the dorsal axis are comparably effective. For abbreviations see Table 4.2. . . .	83
4.25	Goal functions in the coronal, sagittal and axial planes computed for profiles I, II and III (row-wise) when optimizing placement of the custom electrode design with the blunt tip. The planes are shown at the optimal position of SNEX-100 (rectangular pulse), and therefore minimal values might differ for the same profile. Note that for profile II (coronal plane), a suprathreshold activation of the corticofugal pathway can be observed (trivial null-activation solutions were discarded if possible).	84

4.26	Optimized electrode placement (for profiles I, II and III) relative to the classified pathways and relevant brain structures. For visualization purposes, only the trajectory (line with a sphere) is shown for the custom electrode with the blunt tip, which performed comparably to SNEX-100 for normalization of the neural activity in the ventral anterior nucleus (with enabled short-term synaptic depression of pallidothalamic neurons). Note that all trajectories are anterior lateral to the STN and potentially cause a neurological damage in the zona incerta (ZI). RT – reticular nucleus of the thalamus.	87
4.27	Uncertainty in brain tissue conductivity. Left: stochastic scaling factors for the conductivity are chosen from the normal distributions, which standard deviations are derived from [60]. Right: actual conductivity values used in Eq. 2.14 over the DBS power spectrum shown within the two standard deviation margins (95.45%).	88
4.28	Activation rates in the corticofugal pathway computed on the collocation points with Hammersley sampling, further used to derive the surrogate polynomial expansion model. Rows correspond to the optimized protocols for pathway activation profiles I and III suggested in Table 4.1. No corticofugal activation was computed using the optimized protocol for profile II. S_{GM} and S_{WM} are the first order Sobol' indices for the scaling factors of the grey and white matter conductivities, respectively. Note that their effect is comparable for the optimized protocol of profile III, but not for profile I.	89
4.29	Activation rates in the hyperdirect and pallidothalamic pathways computed on the collocation points with Hammersley sampling, further used to derive the surrogate polynomial expansion model. Rows correspond to the optimized protocols for the three pathway activation profiles suggested in Table 4.1. S_{GM} and S_{WM} are the first order Sobol' indices for the scaling factors of the grey and white matter conductivities, respectively. Note that the uncertainty has a larger effect on the hyperdirect pathway activation, and the variation of the white matter conductivity has a higher impact on the activation for all three protocols.	90

List of Tables

4.1	"Optimal" pathway activation profiles of human STN-DBS derived in the retrospective clinical study on motor improvement [144] and in the network analysis of neural activity normalization in the ventral anterior nuclei of the thalamus (VA). The latter was conducted with and without the short-term synaptic depression (STD) in the pallidothalamic neurons. For the corticofugal pathway, which stimulation is associated with motor contractions and dysarthria, the penalization is set for activation rates above a threshold of 2.5%. The cerebellothalamic pathway is added to the analysis due to its involvement in tremor alleviation.	78
4.2	Abbreviations for brain structures in Figs. 4.22, 4.23, 4.24. Note that the number of structures listed here are also targets used in human DBS for various diseases, hence their stimulation might compromise the integrity of experiments.	85
4.3	Mean values \pm standard deviations of approximated pathway activation for the optimized protocols for profiles collected in Table 4.1. The approximation is calculated using the surrogate polynomial expansion model for the considered uncertainties in grey and white matter conductivity. Activation of the cerebellothalamic pathway was not observed in the computational model throughout the optimization and uncertainty quantification. Note that the surrogate model could not accurately evaluate the standard deviation for the corticofugal pathway, which activation dependency violated the smoothness criterion.	88
A.1	Simulation settings.	III

Bibliography

- [1] A. Nambu, Y. Tachibana, and S. Chiken. “Cause of parkinsonian symptoms: Firing rate, firing pattern or dynamic activity changes?” In: *Basal Ganglia* 5.1 (2015), pp. 1–6. ISSN: 2210-5336. DOI: <https://doi.org/10.1016/j.baga.2014.11.001>.
- [2] A. Raz, E. Vaadia, and H. Bergman. “Firing Patterns and Correlations of Spontaneous Discharge of Pallidal Neurons in the Normal and the Tremulous 1-Methyl-4-Phenyl-1,2,3,6-Tetrahydropyridine Vervet Model of Parkinsonism”. In: *Journal of Neuroscience* 20.22 (2000), pp. 8559–8571. ISSN: 0270-6474. DOI: 10.1523/JNEUROSCI.20-22-08559.2000.
- [3] H. Bergman, A. Feingold, A. Nini, and et al. “Physiological aspects of information processing in the basal ganglia of normal and parkinsonian primates”. In: *Trends in Neurosciences* 21.1 (1998), pp. 32–38. ISSN: 0166-2236. DOI: [https://doi.org/10.1016/S0166-2236\(97\)01151-X](https://doi.org/10.1016/S0166-2236(97)01151-X).
- [4] P. Brown, A. Oliviero, P. Mazzone, and et al. “Dopamine Dependency of Oscillations between Subthalamic Nucleus and Pallidum in Parkinson’s Disease”. In: *Journal of Neuroscience* 21.3 (2001), pp. 1033–1038. ISSN: 0270-6474. DOI: 10.1523/JNEUROSCI.21-03-01033.2001.
- [5] R. Levy, W. D. Hutchison, A. M. Lozano, and J. O. Dostrovsky. “High-frequency Synchronization of Neuronal Activity in the Subthalamic Nucleus of Parkinsonian Patients with Limb Tremor”. In: *The Journal of Neuroscience* 20 (2000), pp. 7766 –7775.
- [6] A. Oswal, C. Cao, C. Yeh, and et al. “Neural signatures of hyperdirect pathway activity in Parkinson’s disease”. In: *Nature Communications* 21 (2021). DOI: 10.1038/s41467-021-25366-0.
- [7] Y. Tachibana, H. Iwamuro, H. Kita, and et al. “Subthalamo-pallidal interactions underlying parkinsonian neuronal oscillations in the primate basal ganglia”. In: *European Journal of Neuroscience* 34.9 (2011),

pp. 1470–1484. DOI: <https://doi.org/10.1111/j.1460-9568.2011.07865.x>.

- [8] J. Feingold, D. J. Gibson, B. DePasquale, and A. M. Graybiel. “Bursts of beta oscillation differentiate postperformance activity in the striatum and motor cortex of monkeys performing movement tasks”. In: *Proceedings of the National Academy of Sciences* 112.44 (2015), pp. 13687–13692. ISSN: 0027-8424. DOI: [10.1073/pnas.1517629112](https://doi.org/10.1073/pnas.1517629112).
- [9] J. Kim, Y. Kim, R. Nakajima, and et al. “Inhibitory Basal Ganglia Inputs Induce Excitatory Motor Signals in the Thalamus”. In: *Neuron* 95.5 (2017), pp. 1181–1196. ISSN: 0896-6273. DOI: <https://doi.org/10.1016/j.neuron.2017.08.028>.
- [10] B. Edlow, A. Mareyam, A. Horn, and et al. “7 Tesla MRI of the ex vivo human brain at 100 micron resolution”. In: *Sci Data* 6 (2019). DOI: <https://doi.org/10.1038/s41597-019-0254-8>.
- [11] S. Ewert, P. Plettig, N. Li, and et al. “Toward defining deep brain stimulation targets in MNI space: A subcortical atlas based on multimodal MRI, histology and structural connectivity”. In: *NeuroImage* 170 (2018), pp. 271–282. DOI: [10.1016/j.neuroimage.2017.05.015](https://doi.org/10.1016/j.neuroimage.2017.05.015).
- [12] A. Horn and A. A. Kühn. “Lead-DBS: A toolbox for deep brain stimulation electrode localizations and visualizations”. In: *NeuroImage* 107 (2015), pp. 127–135. ISSN: 1053-8119. DOI: <https://doi.org/10.1016/j.neuroimage.2014.12.002>.
- [13] J. L. Vitek and L. A. Johnson. “Understanding Parkinson’s disease and deep brain stimulation: Role of monkey models”. In: *Proceedings of the National Academy of Sciences* 116.52 (2019), pp. 26259–26265. ISSN: 0027-8424. DOI: [10.1073/pnas.1902300116](https://doi.org/10.1073/pnas.1902300116).
- [14] H. Bergman, T. Wichmann, and M. R. DeLong. “Reversal of Experimental Parkinsonism by Lesions of the Subthalamic Nucleus”. In: *Science* 249.4975 (1990), pp. 1436–1438. DOI: [10.1126/science.2402638](https://doi.org/10.1126/science.2402638).
- [15] F. Machado and C. Reppold. “The effect of deep brain stimulation on motor and cognitive symptoms of Parkinson’s disease: A literature review”. In: *Dementia & Neuropsychologia* 9.1 (2015), pp. 24–31. DOI: [10.1590/S1980-57642015DN91000005](https://doi.org/10.1590/S1980-57642015DN91000005).
- [16] A. Berney, F. Vingerhoets, A. Perrin, and et al. “Effect on mood of subthalamic DBS for Parkinson’s disease A consecutive series of 24 patients”. In: *Neurology* 59.9 (2002), pp. 1427–1429. ISSN: 0028-3878. DOI: [10.1212/01.WNL.0000032756.14298.18](https://doi.org/10.1212/01.WNL.0000032756.14298.18).

- [17] J. Kulisevsky, M. L. Berthier, A. Gironell, and et al. “Mania following deep brain stimulation for Parkinson’s disease”. In: *Neurology* 59.9 (2002), pp. 1421–1424. ISSN: 0028-3878. DOI: 10.1212/WNL.59.9.1421.
- [18] A. Costanza, M. Radomska, G. Bondolfi, and et al. “Suicidality Associated With Deep Brain Stimulation in Extrapyrmidal Diseases: A Critical Review and Hypotheses on Neuroanatomical and Neuroimmune Mechanisms”. In: *Frontiers in Integrative Neuroscience* 15 (2021), p. 5. ISSN: 1662-5145. DOI: 10.3389/fnint.2021.632249.
- [19] A. Kelly, L. Ballerini, M. Lowery, and M. Biggs. “Engineering the Neural Interface”. In: *Comprehensive Biomaterials II*. Elsevier, Jan. 2017. DOI: 10.1016/B978-0-12-803581-8.09322-X.
- [20] S. L. Schmidt, J. J. Peters, D. A. Turner, and W. M. Grill. “Continuous deep brain stimulation of the subthalamic nucleus may not modulate beta bursts in patients with Parkinson”. In: *Brain Stimulation* 13.2 (2020), pp. 433–443. DOI: 10.1016/j.brs.2019.12.008.
- [21] T. Hashimoto, C. M. Elder, M. S. Okun, and et al. “Stimulation of the Subthalamic Nucleus Changes the Firing Pattern of Pallidal Neurons”. In: *Journal of Neuroscience* 23.5 (2003), pp. 1916–1923. ISSN: 0270-6474. DOI: 10.1523/JNEUROSCI.23-05-01916.2003.
- [22] S. Miocinovic, S. Somayajula, S. Chitnis, and J. L. Vitek. “History, Applications, and Mechanisms of Deep Brain Stimulation”. In: *JAMA Neurology* 70.2 (Feb. 2013), pp. 163–171. ISSN: 2168-6149. DOI: 10.1001/2013.jamaneurol.45.
- [23] W. M. Grill, A. Snyder, and S. Miocinovic. “Deep brain stimulation creates an informational lesion of the stimulated nucleus.” In: *Neuroreport* 15 (2004), pp. 1137–1140. DOI: 10.1097/00001756-200405190-00011.
- [24] A. Horn, M. M. Reich, J. Vorwerk, and et al. “Connectivity predicts deep brain stimulation outcome in Parkinson disease”. In: *Annals of Neurology* 82.1 (2017), pp. 67–78. DOI: <https://doi.org/10.1002/ana.24974>.
- [25] V. A. Coenen, B. Sajonz, T. Prokop, and et al. “The dentato-rubro-thalamic tract as the potential common deep brain stimulation target for tremor of various origin: an observational case series”. In: *Acta Neurochirurgica* 162 (2020), pp. 1053–1066.
- [26] I. Adamchic, C. Hauptmann, U. B. Barnikol, and et al. “Coordinated reset neuromodulation for Parkinson’s disease: Proof-of-concept study”. In: *Movement Disorders* 29.13 (2014), pp. 1679–1684. DOI: <https://doi.org/10.1002/mds.25923>.

- [27] J. Wang, S. Nebeck, A. Muralidharan, and et al. “Coordinated Reset Deep Brain Stimulation of Subthalamic Nucleus Produces Long-Lasting, Dose-Dependent Motor Improvements in the 1-Methyl-4-phenyl-1,2,3,6-tetrahydropyridine Non-Human Primate Model of Parkinsonism”. In: *Brain Stimulation* 9.4 (2016), pp. 609–617. DOI: 10.1016/j.brs.2016.03.014.
- [28] N. Yamawaki, P. Magill, G. Woodhall, and et al. “Frequency selectivity and dopamine-dependence of plasticity at glutamatergic synapses in the subthalamic nucleus”. In: *Neuroscience* 203 (2012), pp. 1–11. ISSN: 0306-4522. DOI: <https://doi.org/10.1016/j.neuroscience.2011.12.027>.
- [29] N. Bruet, F. Windels, A. Bertrand, C. Feuerstein, A. Poupard, and M. Savasta. “High Frequency Stimulation of the Subthalamic Nucleus Increases the Extracellular Contents of Striatal Dopamine in Normal and Partially Dopaminergic Denervated Rats”. In: *Journal of Neuropathology & Experimental Neurology* 60.1 (Jan. 2001), pp. 15–24. ISSN: 0022-3069. DOI: 10.1093/jnen/60.1.15.
- [30] W. Meissner, T. Reum, G. Paul, and et al. “Striatal dopaminergic metabolism is increased by deep brain stimulation of the subthalamic nucleus in 6-hydroxydopamine lesioned rats”. In: *Neuroscience Letters* 303.3 (2001), pp. 165–168. ISSN: 0304-3940. DOI: [https://doi.org/10.1016/S0304-3940\(01\)01758-X](https://doi.org/10.1016/S0304-3940(01)01758-X).
- [31] R. H. Walker, C. Moore, G. Davies, and et al. “Effects of Subthalamic Nucleus Lesions and Stimulation upon Corticostriatal Afferents in the 6-Hydroxydopamine-Lesioned Rat”. In: *PLOS ONE* 7.3 (Mar. 2012), pp. 1–10. DOI: 10.1371/journal.pone.0032919.
- [32] H. Bergman, T. Wichmann, B. Karmon, and M. R. DeLong. “The primate subthalamic nucleus. II. Neuronal activity in the MPTP model of parkinsonism”. In: *Journal of Neurophysiology* 72.2 (1994), pp. 507–520. DOI: 10.1152/jn.1994.72.2.507.
- [33] R. Burns, C. Chiueh, S. Markey, and et al. “A primate model of parkinsonism: selective destruction of dopaminergic neurons in the pars compacta of the substantia nigra by N-methyl-4-phenyl-1,2,3,6-tetrahydropyridine”. In: *Proceedings of the National Academy of Sciences* 80.14 (1983), pp. 4546–4550. ISSN: 0027-8424. DOI: 10.1073/pnas.80.14.4546.
- [34] A. Abbott. “Max Planck scientists criticize handling of animal-rights charges against leading neuroscientist”. In: *nature* (May 30, 2018). URL: <https://doi.org/10.1038/d41586-018-05187-w>.

- [35] A. Abbott. “German court dismisses animal-welfare case against leading neuroscientist”. In: *nature* (Dec. 20, 2018). URL: <https://doi.org/10.1038/d41586-018-05187-w>.
- [36] K. Chatfield and D. Morton. “The Use of Non-human Primates in Research”. In: *Ethics Dumping: Case Studies from North-South Research Collaborations*. Ed. by D. Schroeder, J. Cook, F. Hirsch, S. Fenet, and V. Muthuswamy. Springer International Publishing, 2018, pp. 81–90. DOI: 10.1007/978-3-319-64731-9_10.
- [37] S. D. Skaper and P. Giusti. “Transgenic Mouse Models of Parkinsons Disease and Huntingtons Disease”. In: *CNS & Neurological Disorders - Drug Targets* 9.4 (2010), pp. 455–470. ISSN: 0027-8424. DOI: 10.2174/187152710791556186.
- [38] G. E. Meredith and P. Giusti. “MPTP Mouse Models of Parkinson’s Disease: An Update”. In: *Journal of Parkinson’s Disease* 1.1 (2011), pp. 19–33. DOI: 10.3233/JPD-2011-11023.
- [39] M. Fleischer, H. Endres, M. Sendtner, and J. Volkmann. “Development of a Fully Implantable Stimulator for Deep Brain Stimulation in Mice”. In: *Frontiers in Neuroscience* 14 (2020). ISSN: 1662-453X. DOI: 10.3389/fnins.2020.00726.
- [40] F. Plocksties, M. Kober, C. Niemann, and et al. “The software defined implantable modular platform (STELLA) for preclinical deep brain stimulation research in rodents”. In: *Journal of Neural Engineering* 18.5 (2021), p. 056032. DOI: 10.1088/1741-2552/ac23e1.
- [41] S. Duty and P. Jenner. “Animal models of Parkinson’s disease: a source of novel treatments and clues to the cause of the disease”. In: *British Journal of Pharmacology* 164.4 (2011), pp. 1357–1391. DOI: <https://doi.org/10.1111/j.1476-5381.2011.01426.x>.
- [42] M. Lundblad, E. Vaudano, and M. Cenci. “Cellular and behavioural effects of the adenosine A2a receptor antagonist KW-6002 in a rat model of l-DOPA-induced dyskinesia”. In: *Journal of Neurochemistry* 84.6 (2003), pp. 1398–1410. DOI: <https://doi.org/10.1046/j.1471-4159.2003.01632.x>.
- [43] C. Lindemann, M. Alam, J. K. Krauss, and K. Schwabe. “Neuronal activity in the medial associative-limbic and lateral motor part of the rat subthalamic nucleus and the effect of 6-hydroxydopamine-induced lesions of the dorsolateral striatum”. In: *Journal of Comparative Neurology* 521.14 (), pp. 3226–3240.

- [44] C. Severin, P. Young, and L. Massopust. “Pallidothalamic projections in the rat”. In: *Journal of Comparative Neurology* 166.4 (1976), pp. 491–502. DOI: <https://doi.org/10.1002/cne.901660409>.
- [45] G. A. Johnson, R. Laoprasert, R. J. Anderson, and et al. “A multicontrast MR atlas of the Wistar rat brain”. In: *NeuroImage* 242 (2021), p. 118470. ISSN: 1053-8119. DOI: <https://doi.org/10.1016/j.neuroimage.2021.118470>.
- [46] E. Dowd, C. Monville, E. M. Torres, and S. B. Dunnett. “The Corridor Task: A simple test of lateralised response selection sensitive to unilateral dopamine deafferentation and graft-derived dopamine replacement in the striatum”. In: *Brain Research Bulletin* 68.1 (2005). Proceedings of the 14th and 15th Meetings of the European Network for CNS Transplantation and Repair (NECTAR), pp. 24–30. ISSN: 0361-9230. DOI: <https://doi.org/10.1016/j.brainresbull.2005.08.009>.
- [47] K. Badstübner, U. Gimsa, I. Weber, A. Tuchscherer, and J. Gimsa. “Deep Brain Stimulation of Hemiparkinsonian Rats with Unipolar and Bipolar Electrodes for up to 6 Weeks: Behavioral Testing of Freely Moving Animals”. In: *Parkinson’s Disease* 2017 (2017). DOI: 10.1155/2017/5693589.
- [48] A. Huotarinen, S. Leino, R. K. Tuominen, and A. Laakso. “Rat subthalamic stimulation: Evaluating stimulation-induced dyskinesias, choosing stimulation currents and evaluating the anti-akinetic effect in the cylinder test”. In: *MethodsX* 6 (2019), pp. 2384–2395. ISSN: 2215-0161. DOI: <https://doi.org/10.1016/j.mex.2019.10.012>.
- [49] “Nissl Stain”. In: *Encyclopedia of Neuroscience*. Ed. by M. D. Binder, N. Hirokawa, and U. Windhorst. Berlin, Heidelberg: Springer Berlin Heidelberg, 2009, pp. 2871–2871. ISBN: 978-3-540-29678-2. DOI: 10.1007/978-3-540-29678-2_3984.
- [50] J. Rangarajan, G. Vande Velde, F. van Gent, and et al. “Image-based in vivo assessment of targeting accuracy of stereotactic brain surgery in experimental rodent models”. In: *Sci Rep* 6 (2016). DOI: <https://doi.org/10.1038/srep38058>.
- [51] A. Andree, N. Li, K. Butenko, and et al. *Deep Brain Stimulation Electrode Modeling in Rats*. Under review in *Experimental Neurology*. 2021.
- [52] J. Maxwell. *A Treatise on Electricity and Magnetism*. Clarendon Press, 1873.
- [53] J. Peatross and M. Ware. *Physics of Light and Optics*. Brigham Young University, 2015. ISBN: 978-1-312-92927-2.

- [54] U. van Rienen. “Numerical Methods in Computational Electrodynamics”. In: vol. 12. Springer-Verlag Berlin Heidelberg, 2001. Chap. 1, pp. 17–19.
- [55] R. Plonsey and D. Heppner. “Considerations of quasi-stationarity in electrophysiological systems”. In: *The bulletin of mathematical biophysics* 29.4 (1967), pp. 657–664.
- [56] T. J. Foutz and C. C. McIntyre. “Evaluation of novel stimulus waveforms for deep brain stimulation”. In: *Journal of Neural Engineering* 7.6 (2010). DOI: 10.1088/1741-2560/7/6/066008.
- [57] M. Deprez, K. Luyck, L. Luyten, and et al. “An evaluation of the effect of pulse-shape on grey and white matter stimulation in the rat brain”. In: *Sci Rep* 8 (2018). DOI: <https://doi.org/10.1038/s41598-017-19023-0>.
- [58] S. Gabriel, R. Lau, and C. Gabriel. “The dielectric properties of biological tissues: III. Parametric models for the dielectric spectrum of tissues”. In: *Physics in Medicine and Biology* 41.11 (1996), pp. 2271–2293. DOI: 10.1088/0031-9155/41/11/003.
- [59] J. Zimmermann and U. van Rienen. “Ambiguity in the interpretation of the low-frequency dielectric properties of biological tissues”. In: *Bioelectrochemistry* 140 (2021). ISSN: 1567-5394. DOI: <https://doi.org/10.1016/j.bioelechem.2021.107773>.
- [60] L. Koessler, S. Colnat-Coulbois, T. Cecchin, and et al. “In-vivo measurements of human brain tissue conductivity using focal electrical current injection through intracerebral multicontact electrodes”. In: *Human Brain Mapping* 38.2 (2017), pp. 974–986. DOI: <https://doi.org/10.1002/hbm.23431>.
- [61] K. Butenko, C. Bahls, and U. van Rienen. “Evaluation of Epistemic Uncertainties for Bipolar Deep Brain Stimulation in Rodent Models”. In: *2019 41st Annual International Conference of the IEEE Engineering in Medicine and Biology Society (EMBC)*. 2019, pp. 2136–2140. DOI: 10.1109/EMBC.2019.8857910.
- [62] C. Butson and C. C. McIntyre. “Tissue and electrode capacitance reduce neural activation volumes during deep brain stimulation”. In: *Clinical Neurophysiology* 116.10 (2005), pp. 2490–2500. DOI: 10.1016/j.clinph.2005.06.023.

- [63] C. Schmidt, T. Flisgen, and U. van Rienen. “Efficient Computation of the Neural Activation During Deep Brain Stimulation for Dispersive Electrical Properties of Brain Tissue”. In: *IEEE Transactions on Magnetics* 52.3 (2016), pp. 1–4. DOI: 10.1109/TMAG.2015.2498098.
- [64] K. Butenko and U. van Rienen. “Chapter 7 - DBS imaging methods III: Estimating the electric field and volume of tissue activated”. In: *Connectomic Deep Brain Stimulation*. Ed. by A. Horn. Academic Press, 2021, pp. 147–168. ISBN: 978-0-12-821861-7. DOI: <https://doi.org/10.1016/B978-0-12-821861-7.00021-X>.
- [65] H. McCann, G. Pisano, and L. Beltrachini. “Variation in Reported Human Head Tissue Electrical Conductivity Values”. In: *Brain Topography* 32.5 (2019), pp. 825–858.
- [66] P. W. Nicholson. “Specific impedance of cerebral white matter”. In: *Experimental Neurology* 13.4 (1965), pp. 386–401. ISSN: 0014-4886. DOI: [https://doi.org/10.1016/0014-4886\(65\)90126-3](https://doi.org/10.1016/0014-4886(65)90126-3).
- [67] S. Zhang and K. Arfanakis. “Evaluation of standardized and study-specific diffusion tensor imaging templates of the adult human brain: Template characteristics, spatial normalization accuracy, and detection of small inter-group FA differences”. In: *NeuroImage* 172 (2018), pp. 40–50. ISSN: 1053-8119. DOI: <https://doi.org/10.1016/j.neuroimage.2018.01.046>.
- [68] S. Miocinovic, S. F. Lempka, G. S. Russo, and et al. “Experimental and theoretical characterization of the voltage distribution generated by deep brain stimulation”. In: *Experimental Neurology* 216.1 (2009), pp. 166–176. ISSN: 0014-4886. DOI: <https://doi.org/10.1016/j.expneurol.2008.11.024>.
- [69] A. Böhme and U. van Rienen. “A comparative study of approaches to compute the field distribution of deep brain stimulation in the Hemiparkinson rat model”. In: *2016 38th Annual International Conference of the IEEE Engineering in Medicine and Biology Society (EMBC)*. 2016, pp. 5821–5824. DOI: 10.1109/EMBC.2016.7592051.
- [70] D. S. Tuch, V. J. Wedeen, A. M. Dale, and et al. “Conductivity tensor mapping of the human brain using diffusion tensor MRI”. In: *Proceedings of the National Academy of Sciences* 98.20 (2001), pp. 11697–11701. ISSN: 0027-8424. DOI: 10.1073/pnas.171473898.
- [71] E. Garyfallidis, M. Brett, B. Amirbekian, and et al. “Dipy, a library for the analysis of diffusion MRI data”. In: *Frontiers in Neuroinformatics* 8 (2014). ISSN: 1662-5196. DOI: 10.3389/fninf.2014.00008.

- [72] P. Basser, J. Mattiello, and D. LeBihan. “MR diffusion tensor spectroscopy and imaging”. In: *Biophysical Journal* 66.1 (1994), pp. 259–267. ISSN: 0006-3495. DOI: [https://doi.org/10.1016/S0006-3495\(94\)80775-1](https://doi.org/10.1016/S0006-3495(94)80775-1).
- [73] B. Howell and C. C. McIntyre. “Analyzing the tradeoff between electrical complexity and accuracy in patient-specific computational models of deep brain stimulation”. In: *Journal of Neural Engineering* 13.3 (2016), p. 036023. DOI: [10.1088/1741-2560/13/3/036023](https://doi.org/10.1088/1741-2560/13/3/036023).
- [74] T. Nordin, P. Zsigmond, S. Pujol, and et al. “White matter tracing combined with electric field simulation – A patient-specific approach for deep brain stimulation”. In: *NeuroImage: Clinical* 24 (2019), pp. 1–11.
- [75] D. Güllmar, J. Haueisen, and J. Reichenbach. “Influence of anisotropic electrical conductivity in white matter tissue on the EEG/MEG forward and inverse solution. A high-resolution whole head simulation study”. In: *NeuroImage* 51.1 (2010), pp. 145–163.
- [76] V. Fonov, A. Evans, R. McKinstry, and et al. “Unbiased nonlinear average age-appropriate brain templates from birth to adulthood”. In: *NeuroImage* 47 (2009). Organization for Human Brain Mapping 2009 Annual Meeting. ISSN: 1053-8119. DOI: [https://doi.org/10.1016/S1053-8119\(09\)70884-5](https://doi.org/10.1016/S1053-8119(09)70884-5).
- [77] T. Rohlfing, N. M. Zahr, E. V. Sullivan, and A. Pfefferbaum. “The SRI24 multichannel atlas of normal adult human brain structure”. In: *Human Brain Mapping* 31.5 (2010), pp. 798–819. DOI: <https://doi.org/10.1002/hbm.20906>.
- [78] D. Goerzen, C. Fowler, G. Devenyi, and et al. “An MRI-Derived Neuroanatomical Atlas of the Fischer 344 Rat Brain”. In: *Sci Rep* 10 (2020). DOI: <https://doi.org/10.1038/s41598-020-63965-x>.
- [79] G. Paxinos and C. Watson. *The Rat Brain in Stereotaxic Coordinates*. Academic Press, 2006. ISBN: 9780080475158.
- [80] G. A. Johnson, E. Calabrese, A. Badea, and et al. “A multidimensional magnetic resonance histology atlas of the Wistar rat brain”. In: *NeuroImage* 62.3 (2012), pp. 1848–1856. ISSN: 1053-8119. DOI: <https://doi.org/10.1016/j.neuroimage.2012.05.041>.
- [81] J. Evers and M. Lowery. “The Active Electrode in the Living Brain: The Response of the Brain Parenchyma to Chronically Implanted Deep Brain Stimulation Electrodes”. In: *Operative Neurosurgery* 20.2 (Oct. 2020), pp. 131–140. ISSN: 2332-4252. DOI: [10.1093/ons/opaa326](https://doi.org/10.1093/ons/opaa326).

- [82] D. Orlowski, A. Michalis, A. N. Glud, and et al. “Brain Tissue Reaction to Deep Brain Stimulation—A Longitudinal Study of DBS in the Goettingen Minipig”. In: *Neuromodulation: Technology at the Neural Interface* 20.5 (2017), pp. 417–423. DOI: <https://doi.org/10.1111/ner.12576>.
- [83] V. Vedam-Mai, C. Rodgers, A. Gureck, and et al. “Deep Brain Stimulation associated gliosis: A post-mortem study”. In: *Parkinsonism Related Disorders* 54 (2018), pp. 51–55. ISSN: 1353-8020. DOI: <https://doi.org/10.1016/j.parkreldis.2018.04.009>.
- [84] T. Cheung, M. Nuño, M. Hoffman, and et al. “Longitudinal Impedance Variability in Patients with Chronically Implanted DBS Devices”. In: *Brain Stimulation* 6.5 (2013), pp. 746–751. ISSN: 1935-861X. DOI: <https://doi.org/10.1016/j.brs.2013.03.010>.
- [85] K. Torab, T. Davis, D. Warren, and et al. “Multiple factors may influence the performance of a visual prosthesis based on intracortical microstimulation: nonhuman primate behavioural experimentation”. In: *Journal of Neural Engineering* 8.3 (2011). DOI: 10.1088/1741-2560/8/3/035001.
- [86] S. Hemm, N. Vayssiere, G. Mennessier, and et al. “Evolution of Brain Impedance in Dystonic Patients Treated by GPi Electrical Stimulation”. In: *Neuromodulation: Technology at the Neural Interface* 7.2 (2004), pp. 67–75. DOI: <https://doi.org/10.1111/j.1094-7159.2004.04009.x>.
- [87] P. M. Biesheuvel, Y. Fu, and M. Z. Bazant. “Diffuse charge and Faradaic reactions in porous electrodes”. In: *Phys. Rev. E* 83 (6 2011). DOI: 10.1103/PhysRevE.83.061507.
- [88] E. McAdams and J. Jossinet. “Physical interpretation of Schwan’s limit voltage of linearity”. In: *Med. Biol. Eng. Comput.* 32 (1994). DOI: <https://doi.org/10.1007/BF02518908>.
- [89] E. McAdams and J. Jossinet. “DC nonlinearity of the solid electrode-electrolyte interface-impedance”. In: *Innov. Tech. Biol. Med.* 12 (1991), pp. 329–343.
- [90] S. F. Lempka, S. Miocinovic, M. D. Johnson, and et al. “In vivo impedance spectroscopy of deep brain stimulation electrodes”. In: *Journal of Neural Engineering* 6.4 (2009). DOI: 10.1088/1741-2560/6/4/046001.

- [91] E. McAdams and J. Jossinet. “PA physical interpretation of Schwan’s limit current of linearity”. In: *Ann Biomed Eng* 20 (1994). DOI: <https://doi.org/10.1007/BF02368533>.
- [92] A. Chaturvedi, C. R. Butson, S. F. Lempka, and et al. “Patient-specific models of deep brain stimulation: Influence of field model complexity on neural activation predictions”. In: *Brain Stimulation* 3.2 (2010), pp. 65–77. ISSN: 1935-861X. DOI: <https://doi.org/10.1016/j.brs.2010.01.003>.
- [93] X. F. Wei and W. M. Grill. “Impedance characteristics of deep brain stimulation electrodes in vitro and in vivo”. In: *Journal of Neural Engineering* 6.4 (2009). DOI: 10.1088/1741-2560/6/4/046008.
- [94] D. Satzer, D. Lanctin, L. Eberly, and A. Abosch. “Variation in Deep Brain Stimulation Electrode Impedance over Years Following Electrode Implantation”. In: *Stereotact Funct Neurosurg* 92 (2014), pp. 94–102. DOI: <https://doi.org/10.1159/000358014>.
- [95] *N’Vision® Clinician Programmer with Software Activa® PC, Activa® RC, and Activa® SC neurostimulation systems for deep brain stimulation*. Document 8840/88702010-10. Medtronic.
- [96] J. Gimsa, B. Habel, U. Schreiber, and et al. “Choosing electrodes for deep brain stimulation experiments—electrochemical considerations”. In: *Journal of Neuroscience Methods* 142.2 (2005), pp. 251–265. ISSN: 0165-0270. DOI: <https://doi.org/10.1016/j.jneumeth.2004.09.001>.
- [97] A. L. Hodgkin and A. F. Huxley. “A quantitative description of membrane current and its application to conduction and excitation in nerve”. In: *The Journal of Physiology* 117.4 (1952), pp. 500–544. DOI: <https://doi.org/10.1113/jphysiol.1952.sp004764>.
- [98] W. M. Grill, M. Cantrell, and M. Robertson. “Antidromic propagation of action potentials in branched axons: implications for the mechanisms of action of deep brain stimulation”. In: *J Comput Neurosci* 24 (2008), pp. 81–93. DOI: <https://doi.org/10.1007/s10827-007-0043-9>.
- [99] A. Mathai, T. Wichmann, and Y. Smith. “More than meets the Eye—Myelinated axons crowd the subthalamic nucleus”. In: *Movement Disorders* 28.13 (2013), pp. 1811–1815. DOI: <https://doi.org/10.1002/mds.25603>.

- [100] J. B. Ranck. “Which elements are excited in electrical stimulation of mammalian central nervous system: A review”. In: *Brain Research* 98.3 (1975), pp. 417–440. ISSN: 0006-8993. DOI: [https://doi.org/10.1016/0006-8993\(75\)90364-9](https://doi.org/10.1016/0006-8993(75)90364-9).
- [101] L. Nowak and J. Bullier. “Axons, but not cell bodies, are activated by electrical stimulation in cortical gray matter II. Evidence from selective inactivation of cell bodies and axon initial segments”. In: *Exp Brain Res* 118 (1998), pp. 489–500. DOI: <https://doi.org/10.1007/s002210050305>.
- [102] Yale. http://medcell.med.yale.edu/systems_cell_biology/nervous_system_lab.php. [Online; accessed 18-September-2021].
- [103] B. Frankenhaeuser and A. F. Huxley. “The action potential in the myelinated nerve fibre of *Xenopus laevis* as computed on the basis of voltage clamp data”. In: *The Journal of Physiology* 171.2 (1964), pp. 302–315. DOI: <https://doi.org/10.1113/jphysiol.1964.sp007378>.
- [104] D. R. McNeal. “Analysis of a Model for Excitation of Myelinated Nerve”. In: *IEEE Transactions on Biomedical Engineering* BME-23.4 (1976), pp. 329–337. DOI: 10.1109/TBME.1976.324593.
- [105] F. Rattay. “Analysis of Models for External Stimulation of Axons”. In: *IEEE Transactions on Biomedical Engineering* 33.10 (1986), pp. 974–977.
- [106] B. Tahayori, H. Meffin, S. Dokos, and et al. “Modeling extracellular electrical stimulation: II. Computational validation and numerical results”. In: *Journal of Neural Engineering* 9.6 (2012), p. 065006. DOI: 10.1088/1741-2560/9/6/065006.
- [107] R. Bestel, U. van Rienen, C. Thielemann, and R. Appali. “Influence of Neuronal Morphology on the Shape of Extracellular Recordings With Microelectrode Arrays: A Finite Element Analysis”. In: *IEEE Transactions on Biomedical Engineering* 68.4 (2021), pp. 1317–1329. DOI: 10.1109/TBME.2020.3026635.
- [108] J. Crank and P. Nicolson. “A practical method for numerical evaluation of solutions of partial differential equations of the heat-conduction type”. In: *Mathematical Proceedings of the Cambridge Philosophical Society* 43.1 (1947), pp. 50–67.
- [109] N. Carnevale and H. M.L. *The NEURON Book*. UK Cambridge University Press, 2006.

- [110] J. P. Reilly. “Survey of numerical electrostimulation models”. In: *Physics in Medicine and Biology* 61.12 (2016), pp. 4346–4363. DOI: 10.1088/0031-9155/61/12/4346.
- [111] C. C. McIntyre, A. G. Richardson, and W. M. Grill. “Modeling the excitability of mammalian nerve fibers: Influence of afterpotentials on the recovery cycle”. In: *Journal of Neurophysiology* 87.2 (2002), pp. 995–1006.
- [112] C. C. McIntyre, S. Mori, D. L. Sherman, and et al. “Electric field and stimulating influence generated by deep brain stimulation of the subthalamic nucleus”. In: *Clinical Neurophysiology* 115.3 (2004), pp. 589–595. ISSN: 1388-2457. DOI: <https://doi.org/10.1016/j.clinph.2003.10.033>.
- [113] A. Gillies and D. Willshaw. “Membrane Channel Interactions Underlying Rat Subthalamic Projection Neuron Rhythmic and Bursting Activity”. In: *Journal of Neurophysiology* 95.4 (2006), pp. 2352–2365. DOI: 10.1152/jn.00525.2005.
- [114] B. V. Safronov. “Spatial distribution of Na⁺ and K⁺ channels in spinal dorsal horn neurones: role of the soma, axon and dendrites in spike generation”. In: *Progress in Neurobiology* 59.3 (1999), pp. 217–241. ISSN: 0301-0082. DOI: [https://doi.org/10.1016/S0301-0082\(98\)00051-3](https://doi.org/10.1016/S0301-0082(98)00051-3).
- [115] E. Shink and Y. Smith. “Differential synaptic innervation of neurons in the internal and external segments of the globus pallidus by the GABA- and glutamate-containing terminals in the squirrel monkey”. In: *Journal of Comparative Neurology* 358.1 (1995), pp. 119–141. DOI: <https://doi.org/10.1002/cne.903580108>.
- [116] J. O. Dostrovsky, R. Levy, J. P. Wu, and et al. “Microstimulation-Induced Inhibition of Neuronal Firing in Human Globus Pallidus”. In: *Journal of Neurophysiology* 84.1 (2000), pp. 570–574. DOI: 10.1152/jn.2000.84.1.570.
- [117] C. C. McIntyre, W. M. Grill, D. L. Sherman, and N. V. Thakor. “Cellular Effects of Deep Brain Stimulation: Model-Based Analysis of Activation and Inhibition”. In: *Journal of Neurophysiology* 91.4 (2004), pp. 1457–1469. DOI: 10.1152/jn.00989.2003.
- [118] C. Butson and C. C. McIntyre. “Tissue and electrode capacitance reduce neural activation volumes during deep brain stimulation”. In: *Clinical Neurophysiology* 116.10 (2005), pp. 2490–2500.

- [119] M. Åström, E. Diczfalusy, H. Martens, and K. Wårdell. “Relationship between neural activation and electric field distribution during deep brain stimulation”. In: *IEEE Transactions on Biomedical Engineering* 62.2 (2015), pp. 664–672.
- [120] D. N. Anderson, B. Osting, J. Vorwerk, and et al. “Optimized programming algorithm for cylindrical and directional deep brain stimulation electrodes”. In: *Journal of Neural Engineering* 15.2 (2018), p. 026005. DOI: [10.1088/1741-2552/aaa14b](https://doi.org/10.1088/1741-2552/aaa14b).
- [121] E. Peterson, O. Izad, and D. Tyler. “Predicting myelinated axon activation using spatial characteristics of the extracellular field”. In: *Journal of Neural Engineering* 8.4 (2011), pp. 1–12.
- [122] B. Howell, K. Gunalan, and C. C. McIntyre. “A Driving-Force Predictor for Estimating Pathway Activation in Patient-Specific Models of Deep Brain Stimulation”. In: *Neuromodulation: Technology at the Neural Interface* 22.4 (2019), pp. 403–415. DOI: <https://doi.org/10.1111/ner.12929>.
- [123] M. V. Petersen, J. Mlakar, S. Haber, and et al. “Holographic Reconstruction of Axonal Pathways in the Human Brain”. In: *Neuron* 104.6 (2019), pp. 1056–1064. ISSN: 0896-6273. DOI: <https://doi.org/10.1016/j.neuron.2019.09.030>.
- [124] K. Gunalan, A. Chaturvedi, B. Howell, and et al. “Creating and parameterizing patient-specific deep brain stimulation pathway-activation models using the hyperdirect pathway as an example”. In: *PLoS ONE* 12.4 (2017), pp. 1–19.
- [125] P. M. Lauro, N. Vanegas-Aroyave, L. Huang, and et al. “DBSproc: An open source process for DBS electrode localization and tractographic analysis”. In: *Human Brain Mapping* 37.1 (2016), pp. 422–433. DOI: <https://doi.org/10.1002/hbm.23039>.
- [126] C. R. Butson, S. E. Cooper, J. M. Henderson, and et al. “Probabilistic analysis of activation volumes generated during deep brain stimulation”. In: *NeuroImage* 54.3 (2011), pp. 2096–2104. ISSN: 1053-8119. DOI: <https://doi.org/10.1016/j.neuroimage.2010.10.059>.
- [127] T. A. Dembek, J. Roediger, A. Horn, and et al. “Probabilistic sweet spots predict motor outcome for deep brain stimulation in Parkinson disease”. In: *Annals of Neurology* 86.4 (2019), pp. 527–538. DOI: <https://doi.org/10.1002/ana.25567>.

- [128] M. M. Reich, A. Horn, F. Lange, and et al. “Probabilistic mapping of the antidystonic effect of pallidal neurostimulation: a multicentre imaging study”. In: *Brain* 142.5 (Mar. 2019), pp. 1386–1398. ISSN: 0006-8950. DOI: [10.1093/brain/awz046](https://doi.org/10.1093/brain/awz046).
- [129] T. Cheung, A. M. Noecker, R. L. Alterman, and et al. “Defining a therapeutic target for pallidal deep brain stimulation for dystonia”. In: *Annals of Neurology* 76.1 (2014), pp. 22–30. DOI: <https://doi.org/10.1002/ana.24187>.
- [130] H. Akram, S. N. Sotiropoulos, S. Jbabdi, and et al. “Subthalamic deep brain stimulation sweet spots and hyperdirect cortical connectivity in Parkinson’s disease”. In: *NeuroImage* 158 (2017), pp. 332–345. ISSN: 1053-8119. DOI: <https://doi.org/10.1016/j.neuroimage.2017.07.012>.
- [131] A. M. Noecker, K. S. Choi, P. Riva-Posse, and et al. “StimVision Software: Examples and Applications in Subcallosal Cingulate Deep Brain Stimulation for Depression”. In: *Neuromodulation: Technology at the Neural Interface* 21.2 (2018), pp. 191–196. DOI: <https://doi.org/10.1111/ner.12625>.
- [132] C. Hamani, J. A. Saint-Cyr, J. Fraser, and et al. “The subthalamic nucleus in the context of movement disorders”. In: *Brain* 127.1 (Jan. 2004), pp. 4–20. ISSN: 0006-8950. DOI: [10.1093/brain/awh029](https://doi.org/10.1093/brain/awh029).
- [133] G. B. Dunkerley and D. Duncan. “A light and electron microscopic study of the normal and the degenerating corticospinal tract in the rat”. In: *Journal of Comparative Neurology* 137.2 (1969), pp. 155–183. DOI: <https://doi.org/10.1002/cne.901370204>.
- [134] M. Alnæs, J. Bletcha, J. Hake, and et al. “The FEniCS Project Version 1.5”. In: *Archive of Numerical Software* 3.100 (2015), pp. 9–23.
- [135] A. Bondeson, T. Rylander, and P. Ingelström. *Computational Electromagnetics*. Texts in Applied Mathematics. Springer New York, 2005. ISBN: 9780387261584.
- [136] D. Rincon, E. Aguilera, and J. Chacón. “Tumerical treatment of floating conductors based on the traditional finite element formulation”. In: *Advanced Electromagnetics* 7.3 (2018), pp. 46–55.
- [137] P. Amestoy, I. Duff, J. Koster, and J.-Y. L’Excellent. “A Fully Asynchronous Multifrontal Solver Using Distributed Dynamic Scheduling”. In: *SIAM Journal on Matrix Analysis and Applications* 23.1 (2001), pp. 15–41.

- [138] H. A. van der Vorst. “Bi-CGSTAB: A Fast and Smoothly Converging Variant of Bi-CG for the Solution of Nonsymmetric Linear Systems”. In: *SIAM Journal on Scientific and Statistical Computing* 13.2 (1992), pp. 631–644. DOI: [10.1137/0913035](https://doi.org/10.1137/0913035).
- [139] Y. Saad and M. H. Schultz. “GMRES: A Generalized Minimal Residual Algorithm for Solving Nonsymmetric Linear Systems”. In: *SIAM J. Sci. Stat. Comput.* 7.3 (1986), pp. 856–869. ISSN: 0196-5204.
- [140] K. Butenko, C. Bahls, M. Schröder, and et al. “OSS-DBS: Open-source simulation platform for deep brain stimulation with a comprehensive automated modeling”. In: *PLoS Computational Biology* 16.7 (2020), pp. 1–18. DOI: <https://doi.org/10.1371/journal.pcbi.1008023>.
- [141] R. C. Kirby, A. Logg, M. E. Rognes, and A. R. Terrel. “Common and unusual finite elements”. In: *Automated Solution of Differential Equations by the Finite Element Method: The FEniCS Book*. Ed. by A. Logg, K.-A. Mardal, and G. Wells. Berlin, Heidelberg: Springer Berlin Heidelberg, 2012, pp. 95–119. ISBN: 978-3-642-23099-8. DOI: [10.1007/978-3-642-23099-8_3](https://doi.org/10.1007/978-3-642-23099-8_3).
- [142] L. Demkowicz, J. Kurtz, D. Pardo, and et al. *Computing with Hp-Adaptive Finite Elements, Vol. 2: Frontiers Three Dimensional Elliptic and Maxwell Problems with Applications*. 1st. Chapman & Hall/CRC, 2007.
- [143] D. Merkel. “Docker: lightweight linux containers for consistent development and deployment”. In: *Linux journal* 2014.239 (2014), p. 2.
- [144] K. Butenko, N. Li, C. Neudorfer, and et al. *Linking Profiles of Pathway Activation with Clinical Motor Improvements – a Retrospective Computational Study*. Preprint medRxiv. 2021. DOI: <https://doi.org/10.1101/2021.10.08.21264743>.
- [145] K. Butenko, R. Köhling, and U. van Rienen. “Numerical Study on Electrode Design for Rodent Deep Brain Stimulation With Implantations Cranial to Targeted Nuclei”. In: *Frontiers in Computational Neuroscience* 15 (2021), p. 6. DOI: [10.3389/fncom.2021.631188](https://doi.org/10.3389/fncom.2021.631188).
- [146] R. G. Ghanem and P. D. Spanos. *Stochastic Finite Elements: A Spectral Approach*. Berlin, Heidelberg: Springer-Verlag, 1991. ISBN: 0387974563.
- [147] S. Hosder, R. Walters, and M. Balch. “Efficient Sampling for Non-Intrusive Polynomial Chaos Applications with Multiple Uncertain Input Variables”. In: DOI: [10.2514/6.2007-1939](https://doi.org/10.2514/6.2007-1939).

- [148] J. M. Hammersley. “MONTE CARLO METHODS FOR SOLVING MULTIVARIABLE PROBLEMS”. In: *Annals of the New York Academy of Sciences* 86 (1960).
- [149] S. Tennøe, G. Haldnes, and G. T. Einevoll. “Uncertainpy: A Python Toolbox for Uncertainty Quantification and Sensitivity Analysis in Computational Neuroscience”. In: *Frontiers in Neuroinformatics* 12 (2018), p. 49. ISSN: 1662-5196. DOI: [10.3389/fninf.2018.00049](https://doi.org/10.3389/fninf.2018.00049).
- [150] C. Schmidt. “Uncertainty quantification in a computationally optimised volume conductor model for deep brain stimulation”. PhD thesis. University of Rostock, 2014. DOI: https://doi.org/10.18453/rosdok_id00001251.
- [151] D. Xiu and G. E. Karniadakis. “The Wiener–Askey Polynomial Chaos for Stochastic Differential Equations”. In: *SIAM Journal on Scientific Computing* 24.2 (2002), pp. 619–644. DOI: [10.1137/S1064827501387826](https://doi.org/10.1137/S1064827501387826).
- [152] J. Feinberg and H. P. Langtangen. “Chaospy: An open source tool for designing methods of uncertainty quantification”. In: *Journal of Computational Science* 11 (2015), pp. 46–57. ISSN: 1877-7503. DOI: <https://doi.org/10.1016/j.jocs.2015.08.008>.
- [153] S. Miocinovic, M. Parent, C. R. Butson, and et al. “Computational Analysis of Subthalamic Nucleus and Lenticular Fasciculus Activation During Therapeutic Deep Brain Stimulation”. In: *Journal of Neurophysiology* 96.3 (2006), pp. 1569–1580. DOI: [10.1152/jn.00305.2006](https://doi.org/10.1152/jn.00305.2006).
- [154] G. Tinkhauser, A. Pogosyan, S. Little, and et al. “The modulatory effect of adaptive deep brain stimulation on beta bursts in Parkinson’s disease”. In: *Brain* 140.4 (Feb. 2017), pp. 1053–1067. ISSN: 0006-8950. DOI: [10.1093/brain/awx010](https://doi.org/10.1093/brain/awx010).
- [155] W. Meissner, A. Leblois, D. Hansel, and et al. “Subthalamic high frequency stimulation resets subthalamic firing and reduces abnormal oscillations”. In: *Brain* 128.10 (Aug. 2005), pp. 2372–2382. ISSN: 0006-8950. DOI: [10.1093/brain/awh616](https://doi.org/10.1093/brain/awh616).
- [156] K. Ossowska. “Zona incerta as a therapeutic target in Parkinson’s disease”. In: *Journal of Neurology* 267 (2020), pp. 591–606. DOI: <https://doi.org/10.1007/s00415-019-09486-8>.
- [157] D. McCreery, W. Agnew, T. Yuen, and L. Bullara. “Charge density and charge per phase as cofactors in neural injury induced by electrical stimulation”. In: *IEEE Transactions on Biomedical Engineering* 37.10 (1990), pp. 996–1001. DOI: [10.1109/10.102812](https://doi.org/10.1109/10.102812).

- [158] J. L. Lanciego, N. Luquin, and J. A. Obeso. “Functional Neuroanatomy of the Basal Ganglia”. In: *Cold Spring Harbor Perspectives in Medicine* 2.12 (2012). DOI: [10.1101/cshperspect.a009621](https://doi.org/10.1101/cshperspect.a009621).
- [159] A. A. Kühn, A. Kupsch, G.-H. Schneider, and P. Brown. “Reduction in subthalamic 8–35Hz oscillatory activity correlates with clinical improvement in Parkinson’s disease”. In: *European Journal of Neuroscience* 23.7 (2006), pp. 1956–1960. DOI: <https://doi.org/10.1111/j.1460-9568.2006.04717.x>.
- [160] A. A. Kühn, A. Tsui, T. Aziz, and et al. “Pathological synchronisation in the subthalamic nucleus of patients with Parkinson’s disease relates to both bradykinesia and rigidity”. In: *Experimental Neurology* 215.2 (2009), pp. 380–387. ISSN: 0014-4886. DOI: <https://doi.org/10.1016/j.expneurol.2008.11.008>.
- [161] A. Eusebio, W. Thevathasan, L. Doyle Gaynor, and et al. “Deep brain stimulation can suppress pathological synchronisation in parkinsonian patients”. In: *Journal of Neurology, Neurosurgery & Psychiatry* 82.5 (2011), pp. 569–573. DOI: [10.1136/jnnp.2010.217489](https://doi.org/10.1136/jnnp.2010.217489).
- [162] A. Leblois, W. Meissner, B. Bioulac, and et al. “Late emergence of synchronized oscillatory activity in the pallidum during progressive parkinsonism”. In: *European Journal of Neuroscience* 26.6 (2007), pp. 1701–1713. DOI: <https://doi.org/10.1111/j.1460-9568.2007.05777.x>.
- [163] G. Tommasi, P. Krack, V. Fraix, and et al. “Pyramidal tract side effects induced by deep brain stimulation of the subthalamic nucleus”. In: *Journal of Neurology, Neurosurgery & Psychiatry* 79.7 (2008), pp. 813–819.
- [164] D. Mücke, J. Becker, M. T. Barbe, and et al. “The Effect of Deep Brain Stimulation on the Speech Motor System”. In: *Journal of Speech, Language, and Hearing Research* 57.4 (2014), pp. 1206–1218. DOI: [10.1044/2014_JSLHR-S-13-0155](https://doi.org/10.1044/2014_JSLHR-S-13-0155).
- [165] W. Xu, S. Miocinovic, J. Zhang, and et al. “Dissociation of motor symptoms during deep brain stimulation of the subthalamic nucleus in the region of the internal capsule”. In: *Experimental Neurology* 228.2 (2011), pp. 294–297. ISSN: 0014-4886. DOI: <https://doi.org/10.1016/j.expneurol.2010.08.007>.
- [166] H. Akram, V. Dayal, P. Mahlknecht, and et al. “Connectivity derived thalamic segmentation in deep brain stimulation for tremor”. In: *NeuroImage: Clinical* 18 (2018), pp. 130–142. ISSN: 2213-1582. DOI: <https://doi.org/10.1016/j.nicl.2018.01.008>.

- [167] B. Al-Fatly, S. Ewert, D. Kübler, and et al. “Connectivity profile of thalamic deep brain stimulation to effectively treat essential tremor”. In: *Brain* 142.10 (Aug. 2019), pp. 3086–3098. ISSN: 0006-8950. DOI: 10.1093/brain/awz236.
- [168] K. J. Friston, A. P. Holmes, K. J. Worsley, and et al. “Statistical parametric maps in functional imaging: A general linear approach”. In: *Human Brain Mapping* 2.4 (1994), pp. 189–210. DOI: <https://doi.org/10.1002/hbm.460020402>.
- [169] Q. Li, Z.-M. Qian, G. W. Arbutnott, and et al. “Cortical Effects of Deep Brain Stimulation: Implications for Pathogenesis and Treatment of Parkinson Disease”. In: *JAMA Neurology* 71.1 (Jan. 2014), pp. 100–103.
- [170] T. H. Sanders and D. Jaeger. “Optogenetic stimulation of cortico-subthalamic projections is sufficient to ameliorate bradykinesia in 6-OHDA lesioned mice”. In: *Neurobiology of Disease* 95 (2016), pp. 225–237. ISSN: 0969-9961. DOI: <https://doi.org/10.1016/j.nbd.2016.07.021>.
- [171] G. Lance and W. Williams. “Mixed-Data Classificatory Programs I - Agglomerative Systems”. In: *Aust. Comput. J.* 1 (1967), pp. 15–20.
- [172] D. Whitmer, C. de Solages, B. Hill, and et al. “High frequency deep brain stimulation attenuates subthalamic and cortical rhythms in Parkinson’s disease”. In: *Frontiers in Human Neuroscience* 6 (2012). DOI: 10.3389/fnhum.2012.00155.
- [173] H. C. Walker, H. Huang, C. L. Gonzalez, and et al. “Short latency activation of cortex during clinically effective subthalamic deep brain stimulation for Parkinson’s disease”. In: *Movement Disorders* 27.7 (2012), pp. 864–873. DOI: <https://doi.org/10.1002/mds.25025>.
- [174] C. Hammond, H. Bergman, and P. Brown. “Pathological synchronization in Parkinson’s disease: networks, models and treatments”. In: *Trends in Neurosciences* 30.7 (2007), pp. 357–364. DOI: 10.1016/j.tins.2007.05.004.
- [175] H. Wycis and E. Spiegel. “Ansotomy in paralysis agitans”. In: *Confinia neurologica* 12.4 (1952), pp. 245–246. ISSN: 0010-5678. DOI: 10.1159/000105783.
- [176] W. Xu, G. S. Russo, T. Hashimoto, and et al. “Subthalamic Nucleus Stimulation Modulates Thalamic Neuronal Activity”. In: *Journal of Neuroscience* 28.46 (2008), pp. 11916–11924. ISSN: 0270-6474. DOI: 10.1523/JNEUROSCI.2027-08.2008.

- [177] T. Tsuboi, J. K. Wong, R. S. Eisinger, and et al. “Comparative connectivity correlates of dystonic and essential tremor deep brain stimulation”. In: *Brain* 144.6 (Apr. 2021), pp. 1774–1786. ISSN: 0006-8950. DOI: 10.1093/brain/awab074.
- [178] M. Johnson, S. Miocinovic, C. C. McIntyre, and et al. “Mechanisms and targets of deep brain stimulation in movement disorders”. In: *Neurotherapeutics* 5 (2008), pp. 294–308. DOI: <https://doi.org/10.1016/j.nurt.2008.01.010>.
- [179] M. Rosa, M. Arlotti, G. Ardolino, and et al. “Adaptive deep brain stimulation in a freely moving parkinsonian patient”. In: *Movement Disorders* 30.7 (2015), pp. 1003–1005. DOI: <https://doi.org/10.1002/mds.26241>.
- [180] M. Arlotti, S. Marceglia, G. Foffani, and et al. “Eight-hours adaptive deep brain stimulation in patients with Parkinson disease”. In: *Neurology* 90.11 (2018), pp. 971–976. DOI: 10.1212/WNL.0000000000005121.
- [181] G. Kang and M. Lowery. “Effects of antidromic and orthodromic activation of STN afferent axons during DBS in Parkinson’s disease: a simulation study”. In: *Frontiers in Computational Neuroscience* 8 (2014). DOI: 10.3389/fncom.2014.00032.
- [182] A. Farokhniaee and M. Lowery. “Cortical network effects of subthalamic deep brain stimulation in a thalamo-cortical microcircuit model”. In: *Journal of Neural Engineering* 18.5 (2021). DOI: 10.1088/1741-2552/abee50.
- [183] R. Lofredi, W.-J. Neumann, A. Bock, and et al. “Dopamine-dependent scaling of subthalamic gamma bursts with movement velocity in patients with Parkinson’s disease”. In: *eLife* 7 (2018). DOI: 10.7554/eLife.31895.
- [184] W. Singer. “Neuronal Synchrony: A Versatile Code for the Definition of Relations?” In: *Neuron* 24.1 (1999), pp. 49–65. ISSN: 0896-6273. DOI: [https://doi.org/10.1016/S0896-6273\(00\)80821-1](https://doi.org/10.1016/S0896-6273(00)80821-1).
- [185] M. Uno, N. Ozawa, and M. Yoshida. “The mode of pallido-thalamic transmission investigated with intracellular recording from cat thalamus”. In: *Exp. Brain Res.* 33 (1978), pp. 493–507. DOI: <https://doi.org/10.1007/BF00235570>.
- [186] K. Spiliotis, J. Starke, D. Franz, and et al. *Deep brain stimulation for movement disorder treatment: Exploring frequency-dependent efficacy in a computational network model*. Preprint arXiv. 2021.

- [187] K. Marek, D. Jennings, S. Lasch, and et al. “The Parkinson Progression Marker Initiative (PPMI)”. In: *Progress in Neurobiology* 95.4 (2011), pp. 629–635. ISSN: 0301-0082. DOI: <https://doi.org/10.1016/j.pneurobio.2011.09.005>.
- [188] D. Watts and S. Strogatz. “Collective dynamics of ‘small-world’ networks”. In: *Nature* 393 (1998), pp. 440–442. DOI: <https://doi.org/10.1038/30918>.
- [189] R. Ammari, C. Lopez, B. Bioulac, and et al. “Subthalamic nucleus evokes similar long lasting glutamatergic excitations in pallidal, entopeduncular and nigral neurons in the basal ganglia slice”. In: *Neuroscience* 166.3 (2010), pp. 808–818. ISSN: 0306-4522. DOI: <https://doi.org/10.1016/j.neuroscience.2010.01.011>.
- [190] L.-A. Gouty-Colomer, F. J. Michel, A. Baude, and et al. “Mouse subthalamic nucleus neurons with local axon collaterals”. In: *Journal of Comparative Neurology* 526.2 (2018), pp. 275–284. DOI: <https://doi.org/10.1002/cne.24334>.
- [191] P. A. Dąbrowska, N. Voges, M. von Papen, and et al. “On the Complexity of Resting State Spiking Activity in Monkey Motor Cortex”. In: *Cerebral Cortex Communications* 2.3 (May 2021). ISSN: 2632-7376. DOI: [10.1093/texcom/tgab033](https://doi.org/10.1093/texcom/tgab033).
- [192] A. L. Crowell, E. S. Ryapolova-Webb, J. L. Ostrem, and et al. “Oscillations in sensorimotor cortex in movement disorders: an electrocorticography study”. In: *Brain* 135.2 (2012), pp. 615–630. DOI: [10.1093/brain/awr332](https://doi.org/10.1093/brain/awr332).
- [193] W.-J. Neumann, F. Staub-Bartelt, A. Horn, and et al. “Long term correlation of subthalamic beta band activity with motor impairment in patients with Parkinson’s disease”. In: *Clinical Neurophysiology* 128.11 (2017), pp. 2286–2291. ISSN: 1388-2457. DOI: <https://doi.org/10.1016/j.clinph.2017.08.028>.
- [194] G. C. McConnell, R. Q. So, J. D. Hilliard, and et al. “Effective Deep Brain Stimulation Suppresses Low-Frequency Network Oscillations in the Basal Ganglia by Regularizing Neural Firing Patterns”. In: *Journal of Neuroscience* 32.45 (2012), pp. 15657–15668. ISSN: 0270-6474. DOI: [10.1523/JNEUROSCI.2824-12.2012](https://doi.org/10.1523/JNEUROSCI.2824-12.2012).
- [195] D. Leventhal, G. Gage, R. Schmidt, and et al. “Basal Ganglia Beta Oscillations Accompany Cue Utilization”. In: *Neuron* 73.3 (2012), pp. 523–536. DOI: <https://doi.org/10.1016/j.neuron.2011.11.032>.

- [196] G. Yi and W. M. Grill. “Frequency-dependent antidromic activation in thalamocortical relay neurons: effects of synaptic inputs”. In: *Journal of Neural Engineering* 15.5 (2018). DOI: 10.1088/1741-2552/aacbff.
- [197] C. Bosch-Bouju, B. Hyland, and L. Parr-Brownlie. “Motor thalamus integration of cortical, cerebellar and basal ganglia information: implications for normal and parkinsonian conditions”. In: *Frontiers in Computational Neuroscience* 7 (2013), p. 163. ISSN: 1662-5188. DOI: 10.3389/fncom.2013.00163.
- [198] P. Callaghan, C. Eccles, and Y. Xia. “NMR microscopy of dynamic displacements: k-space and q-space imaging”. In: *Journal of Physics E: Scientific Instruments* 21.8 (1988), pp. 820–822. DOI: 10.1088/0022-3735/21/8/017.
- [199] V. J. Wedeen, P. Hagmann, W.-Y. I. Tseng, and et al. “Mapping complex tissue architecture with diffusion spectrum magnetic resonance imaging”. In: *Magnetic Resonance in Medicine* 54.6 (2005), pp. 1377–1386. DOI: <https://doi.org/10.1002/mrm.20642>.
- [200] J. Hrabe, G. Kaur, and D. Guilfoyle. “Principles and limitations of NMR diffusion measurements”. In: *Journal of Medical Physics* 32.1 (2007), pp. 34–42. DOI: 10.4103/0971-6203.31148.
- [201] M. Niethammer, R. S. J. Estepar, S. Bouix, and et al. “On Diffusion Tensor Estimation”. In: *2006 International Conference of the IEEE Engineering in Medicine and Biology Society*. 2006, pp. 2622–2625. DOI: 10.1109/IEMBS.2006.259826.
- [202] S.-K. Song, S.-W. Sun, M. J. Ramsbottom, and et al. “Dysmyelination Revealed through MRI as Increased Radial (but Unchanged Axial) Diffusion of Water”. In: *NeuroImage* 17.3 (2002), pp. 1429–1436. ISSN: 1053-8119. DOI: <https://doi.org/10.1006/nimg.2002.1267>.
- [203] S. W. Chung, Y. Lu, and R. G. Henry. “Comparison of bootstrap approaches for estimation of uncertainties of DTI parameters”. In: *NeuroImage* 33.2 (2006), pp. 531–541. ISSN: 1053-8119. DOI: <https://doi.org/10.1016/j.neuroimage.2006.07.001>.
- [204] T. Kita and H. Kita. “The Subthalamic Nucleus Is One of Multiple Innervation Sites for Long-Range Corticofugal Axons: A Single-Axon Tracing Study in the Rat”. In: *Journal of Neuroscience* 32.17 (2012), pp. 5990–5999. DOI: 10.1523/JNEUROSCI.5717-11.2012.

- [205] H. T. Kha, D. I. Finkelstein, D. V. Pow, and et al. “Study of projections from the entopeduncular nucleus to the thalamus of the rat”. In: *Journal of Comparative Neurology* 426.3 (2000), pp. 366–377. DOI: [https://doi.org/10.1002/1096-9861\(20001023\)426:3<366::AID-CNE2>3.0.CO;2-B](https://doi.org/10.1002/1096-9861(20001023)426:3<366::AID-CNE2>3.0.CO;2-B).
- [206] O. Schmitt. Personal correspondence. Institute for Anatomy, University Medicine Rostock. 2021.
- [207] J.-D. Tournier, F. Calamante, and A. Connelly. “Robust determination of the fibre orientation distribution in diffusion MRI: Non-negativity constrained super-resolved spherical deconvolution”. In: *NeuroImage* 35.4 (2007), pp. 1459–1472. ISSN: 1053-8119. DOI: <https://doi.org/10.1016/j.neuroimage.2007.02.016>.
- [208] R. E. Smith, J.-D. Tournier, F. Calamante, and A. Connelly. “Anatomically-constrained tractography: Improved diffusion MRI streamlines tractography through effective use of anatomical information”. In: *NeuroImage* 62.3 (2012), pp. 1924–1938. ISSN: 1053-8119. DOI: <https://doi.org/10.1016/j.neuroimage.2012.06.005>.
- [209] I. Aganj, C. Lenglet, G. Sapiro, and et al. “Reconstruction of the orientation distribution function in single- and multiple-shell q-ball imaging within constant solid angle”. In: *Magnetic Resonance in Medicine* 64.2 (2010), pp. 554–566. DOI: <https://doi.org/10.1002/mrm.22365>.
- [210] D. S. Tuch. “Q-ball imaging”. In: *Magnetic Resonance in Medicine* 52.6 (2004), pp. 1358–1372. DOI: <https://doi.org/10.1002/mrm.20279>.
- [211] N. Wang, R. J. Anderson, D. G. Ashbrook, and et al. “Variability and heritability of mouse brain structure: Microscopic MRI atlases and connectomes for diverse strains”. In: *NeuroImage* 222 (2020). ISSN: 1053-8119. DOI: <https://doi.org/10.1016/j.neuroimage.2020.117274>.
- [212] K. Maier-Hein, P. Neher, J Houde, and et al. “The challenge of mapping the human connectome based on diffusion tractography”. In: *Nature Communications* 8 (2017). DOI: <https://doi.org/10.1038/s41467-017-01285-x>.
- [213] C. Thomas, F. Q. Ye, M. O. Irfanoglu, and et al. “Anatomical accuracy of brain connections derived from diffusion MRI tractography is inherently limited”. In: *Proceedings of the National Academy of Sciences* 111.46 (2014), pp. 16574–16579. DOI: [10.1073/pnas.1405672111](https://doi.org/10.1073/pnas.1405672111).
- [214] S. Kirkpatrick, C. Gelatt, and M. Vecchi. “Optimization by Simulated Annealing”. In: *Science* 220.4598 (1983), pp. 671–680. DOI: [10.1126/science.220.4598.671](https://doi.org/10.1126/science.220.4598.671).

- [215] W. Hastings. “Monte Carlo Sampling Methods Using Markov Chains and Their Applications”. In: *Biometrika* 57.1 (1970), pp. 97–109.
- [216] Y. Xiang, D. Sun, W Fan, and X. Gong. “Generalized simulated annealing algorithm and its application to the Thomson model”. In: *Physics Letters A* 233.3 (1997), pp. 216–220. ISSN: 0375-9601. DOI: [https://doi.org/10.1016/S0375-9601\(97\)00474-X](https://doi.org/10.1016/S0375-9601(97)00474-X).
- [217] D. L. Fischer, T. J. Collier, A. Cole-Strauss, and et al. “High-Frequency Stimulation of the Rat Entopeduncular Nucleus Does Not Provide Functional or Morphological Neuroprotection from 6-Hydroxydopamine”. In: *PLOS ONE* 10.7 (July 2015), pp. 1–19. DOI: [10.1371/journal.pone.0133957](https://doi.org/10.1371/journal.pone.0133957).
- [218] A. D. Kirsch, S. Hassin-Baer, M. Cordula, and et al. “Anodic versus cathodic neurostimulation of the subthalamic nucleus: A randomized-controlled study of acute clinical effects”. In: *Parkinsonism & Related Disorders* 55 (2018), pp. 61–67. DOI: <https://doi.org/10.1016/j.parkreldis.2018.05.015>.
- [219] T. D. Aumann, J. A. Rawson, D. I. Finkelstein, and M. K. Horne. “Projections from the lateral and interposed cerebellar nuclei to the thalamus of the rat: A light and electron microscopic study using single and double anterograde labelling”. In: *Journal of Comparative Neurology* 349.2 (1994), pp. 165–181. DOI: <https://doi.org/10.1002/cne.903490202>.
- [220] A. L. Spieles-Engemann, T. J. Collier, and C. E. Sortwell. “A functionally relevant and long-term model of deep brain stimulation of the rat subthalamic nucleus: advantages and considerations”. In: *European Journal of Neuroscience* 32.7 (2010), pp. 1092–1099. DOI: <https://doi.org/10.1111/j.1460-9568.2010.07416.x>.
- [221] A. L. Spieles-Engemann, K. Steece-Collier, M. M. Behbehani, and et al. “Subthalamic nucleus stimulation increases brain derived neurotrophic factor in the nigrostriatal system and primary motor cortex.” In: *Journal of Parkinson’s disease* 11 (2011), pp. 123–136.
- [222] S. Mottaghi, O. Buchholz, and U. G. Hofmann. “Systematic Evaluation of DBS Parameters in the Hemi-Parkinsonian Rat Model”. In: *Frontiers in Neuroscience* 14 (2020). DOI: [10.3389/fnins.2020.561008](https://doi.org/10.3389/fnins.2020.561008).
- [223] T. M. Herrington, J. J. Cheng, and E. N. Eskandar. “Mechanisms of deep brain stimulation”. In: *Journal of Neurophysiology* 115.1 (2016), pp. 19–38. DOI: [10.1152/jn.00281.2015](https://doi.org/10.1152/jn.00281.2015).

Declaration of authorship

I, Konstantin Butenko, hereby declare that the dissertation titled "Modeling Perspective on Translatability of Deep Brain Stimulation Mechanism for Treating Parkinsonian Motor Symptoms in Rodent and Human" has been written by me under the guidance of my supervisor. All the sources of information and aid have been acknowledged to the best of my knowledge. This dissertation has not been submitted previously for any other qualification at any other universities or institutions.

Rostock, 29th of November, 2021

Signature

A handwritten signature in black ink, consisting of stylized initials 'KB' followed by a long horizontal stroke.

Name	Konstantin Butenko
Date of birth	25. February 1994
Address	Warnowufer St. 30 Rostock
E-Mail	konstantinmgtu@gmail.com
Contact number	+49 1625326633



Related Work Experience

- | | |
|---|--|
| October 2021 – | Charité – Universitätsmedizin Berlin
Research Fellow in CRC TRR 295 <ul style="list-style-type: none">• Patient-specific modeling of deep brain stimulation• Software development |
| October 2017 - October 2021 | University of Rostock
Doctoral Researcher in CRC 1270 ELAINE <ul style="list-style-type: none">• Numerical simulation of electromagnetic fields• Computational modeling of stimulated neural tissue• Optimization of deep brain stimulation treatment for Parkinson's disease |
| September 2016 - December 2016 & May 2017 - August 2017 | University of Rostock
Scientific assistant <ul style="list-style-type: none">• Further development of the eigenmode solver Roswell 2.5 for the calculation of eigenwaves with arbitrary azimuthal symmetry• Performance optimization of the software package WizaRD (Wakefield Calculation In Rectangular Waveguides Lined with Dielectrics) |
| July 2014 | Public Limited company "KB Mashinostroenie"
Intern/Engineer's Assistant <ul style="list-style-type: none">• Engineering simulations• Process flow documentation |

Education

- | | |
|-----------------------------|--|
| October 2017 - October 2021 | University of Rostock, Institute of General Electrical Engineering
Ph.D., Engineering. Dissertation: "Modeling Perspective on Translatability of Deep Brain Stimulation Mechanism for Treating Parkinsonian Motor Symptoms in Rodent and Human" |
| October 2015 - October 2017 | University of Rostock
Master of Science, Computational science and engineering |

Personal Achievements

Language skills	Native fluency in Russian Proficiency in English and German Basic skills in Italian
Computer skills	Python/MATLAB/C++ FEniCS/COMSOL Multiphysics/ANSYS/Autodesk Inventor/CST Studio NEURON/Mimics/Lead-DBS/3D Slicer LaTeX/AnyLogic Misc. CAD/CAM/CAE tools
Driver's license	Category B (EU & RU)

Publications

K. Butenko, C. Bahls, and U. van Rienen. "Evaluation of Epistemic Uncertainties for Bipolar Deep Brain Stimulation in Rodent Models". In: 2019 41st Annual International Conference of the IEEE Engineering in Medicine and Biology Society (EMBC). 2019, pp. 2136–2140.

K. Butenko, C. Bahls, M. Schröder, and et al. "OSS-DBS: Open-source simulation platform for deep brain stimulation with a comprehensive automated modeling". In: PLoS Computational Biology 16.7 (2020), pp. 1–18. doi: <https://doi.org/10.1371/journal.pcbi.1008023>

K. Butenko, R. Köhling, and U. van Rienen. "Numerical Study on Electrode Design for Rodent Deep Brain Stimulation With Implantations Cranial to Targeted Nuclei". In: Frontiers in Computational Neuroscience 15 (2021), p.6. doi: <https://doi.org/10.3389/fncom.2021.631188>

K. Butenko and U. van Rienen. "Chapter 7 - DBS imaging methods III: Estimating the electric field and volume of tissue activated". In: Connectomic Deep Brain Stimulation. Ed. by A. Horn. Academic Press, 2021, pp. 147–168. isbn: 978-0-12-821861-7

K. Butenko, N. Li, C. Neudorfer, and et al. Linking Profiles of Pathway Activation with Clinical Motor Improvements – a Retrospective Computational Study. Preprint medRxiv (under revision in Brain Stimulation). 2021. doi: <https://doi.org/10.1101/2021.10.08.21264743>